

UNIVERSITY OF BELGRADE

FACULTY OF MECHANICAL ENGINEERING

**PROCEDURE FOR CALIBRATION OF
MATERIAL CONSTITUTIVE MODELS
FOR POWDER COMPACTION THROUGH
INVERSE ANALYSIS**

DOCTORAL DISSERTATION

SHWETANK PANDEY

BELGRADE, 2018

This page is intentionally left blank.

UNIVERSITY OF BELGRADE



DEPARTMENT OF STRENGTH OF MATERIALS
FACULTY OF MECHANICAL ENGINEERING

PROCEDURE FOR CALIBRATION OF MATERIAL CONSTITUTIVE MODELS FOR POWDER COMPACTION THROUGH INVERSE ANALYSIS



DOCTORAL DISSERTATION

Supervisor

Prof. Dr. Vladimir Buljak

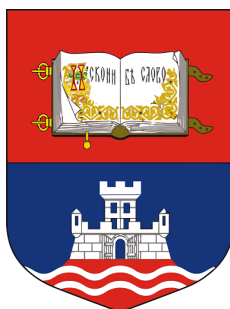
Ph.D. Candidate

Shwetank Pandey

Belgrade, 2018

This page is intentionally left blank.

УНИВЕРЗИТЕТ У БЕОГРАДУ



**КАТЕДРА ЗА ОТПОРНОСТ МАТЕРИЈАЛА
МАШИНСКИ ФАКУЛТЕТ**

**МЕТОДА ЗА КАЛИБРИСАЊЕ КОНСТИТУТИВНИХ
МОДЕЛА ЗА СИМУЛИРАЊЕ ПРОЦЕСА
ПРЕСОВАЊА КЕРАМИЧКОГ ПРАХА
КОРИШЋЕЊЕМ ИНВЕРЗНИХ АНАЛИЗА**



ДОКТОРСКА ДИСЕРТАЦИЈА

МЕНТОР

Проф. др Владимир Буљак

ДОКТОРАНТ

Shwetank Pandey

БЕОГРАД, 2018

This page is intentionally left blank.

PROCEDURE FOR CALIBRATION OF MATERIAL CONSTITUTIVE MODELS FOR POWDER COMPACTION THROUGH INVERSE ANALYSIS

A Thesis Submitted to the Academic Faculty

by

Shwetank Pandey

As a Partial Fulfillment

of the Requirements for the Degree of

Doctor of Philosophy

in

Department of Strength of Materials

Faculty of Mechanical Engineering

Belgrade, February 2018

This page is intentionally left blank.

THESIS REVIEW COMMITTEE

Prof. Dr. Vladimir Buljak (Mentor)

Associate Professor

Department of Strength of Materials

Faculty of Mechanical Engineering

University of Belgrade

Prof. Dr. Igor Balać

Professor

Department of Strength of Materials

Faculty of Mechanical Engineering

University of Belgrade

Prof. Dr. Milorad Milovančević

Professor

Department of Strength of Materials

Faculty of Mechanical Engineering

University of Belgrade

Dr. Nina Obradović

Principal Research Fellow

Institute of Technical Sciences

Serbian Academy of Sciences and Arts

Prof. Dr. Giuseppe Cocchetti

Associate Professor

Department of Civil and Environmental Engineering

Politecnico di Milano

This page is intentionally left blank.

ACKNOWLEDGMENTS

This research is related to the CERMAT-2 project within European Union's Seventh Framework Program FP7/2007-2013/ under REA grad agreement number PITN-GA-2013-606878. I would like to take this opportunity to thank the project organizers and coordinators for their support throughout this work and greatly appreciate the financial help.

I would like to express my sincere gratitude to my advisor Prof. Vladimir Buljak for his patience, motivation, enthusiasm, immense knowledge, and above all his friendship. If not for his continuous support, it would have been impossible to submit this Ph.D thesis in a good shape. His constant guidance helped me not only academically but I also learned a lot in my personal endeavors. I could not have imagined a better mentor for my Ph.D work.

I also deeply thank all the people in Vesuvius Inc., Belgium, for providing the research facilities to conduct all the experiments for this work. In particular, Severine Romero-Baivier and Dr. Achraf Kallel provided me the practical suggestions and a deep insight into industrial practices followed in powder compaction. Their practical knowledge gave me a better perspective to conduct this study. Following my work from the very beginning, their revisions, remarks and ideas contributed a lot to this thesis.

I owe my gratitude to all other professors, colleagues and friends whom I had the opportunity to meet during this project. In particular, I would like to mention Prof. Piccolroaz, Prof. Davide Bigoni, Dr. Scot Swan and Dr. Massimo Penasa for their constructive discussions on theoretical constitutive modeling.

I also thank the professors, colleagues and staff members at my faculty: Prof. Balać, Prof. Grbović, Prof. Petrović, Snezana Obradović and all others for their continued support and availability despite their busy schedule.

I dedicate this thesis to my family, and in particular to my parents for always being there.

This page is intentionally left blank.

ABSTRACT

Ceramic parts are increasingly produced by compacting loose powders to form, what is called a "green body", which is further subjected to sintering, to give the final product. During the sintering stage, the green body undergoes shrinkage inversely proportional to its density, so defects and even large cracks can appear in the presence of density gradients. Such circumstance affects the quality of production of ceramic parts, with still elevated number of rejected pieces.

Numerical simulations of green body formation are increasingly used as a support for the stable production. Modeling the compaction process usually involves complex constitutive models with an elevated number of parameters. The current praxis of evaluating the governing constants relies on a large number of experiments on the green body, like, Brazilian, crush, triaxial tests etc. Therefore, the model calibration is time consuming and rather difficult, presenting an obstacle for routine industrial purposes.

To tackle this problem, an alternative procedure based on Inverse Analysis (IA) is developed, which relies on the data collected from the compaction experiment only. Such approach fully eliminates the need for further testing on the green body, making it practicable for routine industrial purposes. Within this methodology, a discrepancy function is formed that quantifies the difference between experimental and simulated quantities collected from the compaction test, which is further minimized to give the constitutive parameters. To ascertain the strong influence of sought parameters on measurable data, certain new green body geometries are designed.

Proposed approach is tested and validated on the calibration of "modified" Drucker-Prager Cap (DPC) model, which is frequently adopted for powder pressing simulations. To this purpose, rigorous experimentation involving both compaction tests for calibration and destructive tests for verification are performed. The parameters obtained through IA are used to simulate complex geometries, followed by a comparative study between the currently adopted praxis vs. inverse analysis methodology.

Further on, calibration of a more sophisticated material model relying on the Bigoni-Piccolroaz yield surface is considered. Certain instabilities in the numerical

implementation of this fairly complex model, lead to discontinuous discrepancy function, and therefore, parameters are assessed by performing the minimization through genetic algorithms. Computational burden coming from recursive simulations required by the genetic algorithm is made consistent by employing controllably "enriched" reduced basis model based on proper orthogonal decomposition. Finally, a comparison between the novel model and the "modified" DPC model is presented.

Keywords: Inverse Analysis, Powder Compaction, Material Calibration, Drucker-Prager Cap, Bigoni-Piccolroaz, Reduced Basis Model

Scientific Discipline: Mechanical Engineering

Scientific Sub-discipline: Strength of Materials

This page is intentionally left blank.

САЖЕТАК

Производња керамичких компоненти најчешће се састоји из процеса механичког компактирања керамичког праха у циљу добијања испреска, који се потом подвргава синтеровању на повишеној температури. У току синтеровања, евентуално присуство шупљина у отпреску изазива интензивније локално скупљање материјала у тој зони, што за последицу има нехомогеност финалног производа или стварање унутрашњих прскотина. Сходно томе перформансе финалног производа у великој мери су условљене квалитетом произведеног отпреска.

Значајан фактор за стабилну и ефикасну производњу керамичких отпресака представља могућност извођења реалистичних нумеричких симулација самог процеса. Моделирање овог процеса најчешће укључује комплексне конститутивне моделе са великим бројем параметара. Процедуре калибрисања ових параметара, које су тренутно у примени, захтевају извођење низа деструктивних тестова на отпреску. Овакав приступ је захтеван и неприлагођен за рутинску индустријску примену.

У оквиру ове дисертације развијена је алтернативна метода, са низом предности при решавању описаног проблема калибрације параметара, заснована на примени инверзних анализа. Развијена метода користи као експерименталне податке искључиво оне вредности које се могу измерити у току процеса сабијања, чиме је искључена потреба за спровођењем деструктивних испитивања на отпреску. У оквиру развијене методе формирана је циљна функција која квантификује дискрепанцу између експериментално измерених, и одговарајућих нумерички добијених вредности. Тако је процес калибрације конститутивних параметара сведен на проблем нумеричке минимизације формиране циљне функције. Како би се обезбедила одговарајућа осетљивост експериментално измерених вредности на тражене параметере, дефинисане су посебне геометрије отпресака као резултат детаљне геометријске анализе. Тиме је формиран експериментални протокол који тачно дефинише геометрију отпресака, избор

експерименталних вредности, и примену одговарајућих алгоритама и циљу аутоматског добијања тражених конститутивних параметара.

Развијена метода је тестирана на решавању проблема калибрације "Drucker-Prager Cap" конститутивног модела, који се често примењује у симулацијама процеса сабијања праха. Тестирање је укључило и обимну експерименталну кампању коришћењем деструктивних тестова на отпресцима, чиме су добијене референтне вредности, употребљене као база за поређење. Допунска верификација састојала се у симулирању комплексних геометрија, коришћењем конститутивних параметара добијених применом развијене методе.

Предложена метода је примењена и на калибрацију сложенијег конститутивног модела који користи "Bishop-Piccolroaz" модел пластичности. Ово представља нов и изразито комплексан конститутивни модел, па је његова нумеричка имплементација резултирала нестабилним нумеричким симулацијама, чинећи циљну функцију дисконтинуалном. При решавању овог проблема калибрације, минимизација је извршена употребом „генетичких алгоритама“, уз развијени редуковани модел за нумеричке симулације теста, чиме је постигнуто значајно смањење компјутерског времена при извођењу нелинеарних симулација. На самом крају, упоређени су резултати добијени применом једног и другог конститутивног модела уз назначене смернице о групи проблема на којима их је могуће применити са задовољавајућом тачношћу.

Кључне Речи: Инверзне Анализе, Пресовање Праха, Калибрација Конститутивних Модела, Редуковани Модели, "Drucker-Prager Cap", Модел Пластичности, "Bigoni-Riccolroaz", Модел Пластичности

Научна дисциплина: Машинство

Ужа научна област: Отпорност Конструкција

This page is intentionally left blank.

Contents

List of Figures	v
List of Tables	xiii
1 INTRODUCTION	1
1.1 General Motivations	4
1.2 Primary Objectives	6
1.3 Outline of the Method	7
1.4 Organization of the Thesis	8
2 CURRENT CALIBRATION PROCEDURES FOR POWDER COMPACTION MODELS	10
2.1 The Drucker Prager Cap Model	11
2.2 Current Practice for Calibration of DPC Model	13
2.2.1 Shear Failure Surface Characterization	15
2.2.2 Cap Surface Characterization	18
2.2.3 Evaluation of Elastic Properties	20
3 ON INVERSE ANALYSIS, POWDER COMPACTION SIMULATION AND RELATED NOVELTIES	23
3.1 Compaction: Experiment and its Simulation	27
3.1.1 Experiment	27
3.1.2 General Aspects of Experiment Simulation	29
3.2 Mathematical Programming	32
3.2.1 Forming the Discrepancy Function	32

3.2.2	Minimization Algorithms	33
4	PROPOSED CALIBRATION PROTOCOLS	39
4.1	Sensitivity Analysis	46
4.2	Effects of Friction	54
5	RESULTS	59
5.1	Materials and Experiments	59
5.1.1	Compaction Tests	60
5.1.2	Crush and Brazilian Tests	69
5.2	Determination of Parameters Based on Currently Adopted Praxis	76
5.2.1	Shear Failure Surface Parameters	77
5.2.2	Cap Surface Parameters	78
5.2.3	Elastic Parameters	81
5.3	Determination of Parameters based on Inverse Analysis	82
5.3.1	Results of IA by Employing Two Configurations	85
5.3.2	Results of IA by Employing Three Configurations	88
5.4	Simulation of Complex Geometries Using Parameters Obtained from IA	98
5.5	Inverse Analysis Approach vs. Currently Adopted Praxis	101
5.6	Summary of the Inverse Analysis Protocol	106
6	CALIBRATION OF NOVEL MATERIAL MODEL THROUGH INVERSE ANALYSIS	107
6.1	Novel Constitutive Model for Powder Compaction	109
6.1.1	Bigoni-Piccolroaz Yield Function	110
6.1.2	Description of Hardening Rules	113
6.1.3	Elastic Response and Elasto-Plastic Coupling	114
6.2	Genetic Algorithms	116
6.3	Reduced Basis Model	120
6.4	POD-RBF Model for Direct Analysis	124
6.5	POD-RBF Model with Controllable Enrichment for Inverse Analysis	128
6.6	Results and Discussions	133

6.6.1 Comparison between Drucker-Prager Cap and Bigoni Piccolroaz Yield Surface	138
7 CONCLUSIONS AND FUTURE WORK	142
7.1 Conclusions	142
7.2 Future Research	145
BIBLIOGRAPHY	148
APPENDIX A EVALUATION OF THE RADIAL STRESS FROM STRAIN GAUGE	A-1

This page is intentionally left blank.

List of Figures

1.1	Schematic representation of cold compaction	2
1.2	Unloading phase of powder compaction at different relative densities evidencing change in elastic properties as compaction progresses	5
1.3	Representation of changes in plastic property with changing relative density evidenced by shift in DPC yield surface	5
2.1	The DPC yield surface in p - q plane	11
2.2	Brazilian test setup	15
2.3	Crush test setup	16
2.4	Schematic representation of different tests needed for calibration of shear failure line DPC yield criterion	17
2.5	Visualization of loading path in compaction test	18
3.1	Schematic representation of IA procedure	24
3.2	Experimental setup of compaction test	28
3.3	Force vs. displacement (of the punch) curve from compaction experiment	29
3.4	FE model of compaction simulation and the digitally extracted curve	31
3.5	Visualization of the residual vector formation as the difference between experimental and simulated curve for compaction.	32
4.1	Cylindrical green body	40
4.2	Compaction curve corresponding to the cylindrical green body	40
4.3	Experimental vs. computed curves (initialization 1)	42
4.4	Experimental vs. computed curves (initialization 2)	42
4.5	Cohesion corresponding to initialization 1 and 2	44

LIST OF FIGURES

4.6	Hydrostatic yield compression stress corresponding to initialization 1 and 2	44
4.7	Cap eccentricity corresponding to initialization 1 and 2	45
4.8	Stress distribution in configuration-1	45
4.9	Proposed punch design along with the conventional cylindrical one	47
4.10	Schematic representation of proposed green body configurations	47
4.11	Stress distribution in configuration-2	48
4.12	Stress distribution in configuration-3	48
4.13	Stress distribution in configuration-4	49
4.14	2-D Schematic representation of specimen to show material point locations	50
4.15	Stress path of selected material points in configuration-1	51
4.16	Stress path of selected material points in configuration-2	51
4.17	Stress path of selected material points in configuration-3	52
4.18	Stress path of selected material points in configuration-4	52
4.19	Stress path of material point-3 in all configurations	53
4.20	Stress distribution highlighting effect of friction in configuration-1	55
4.21	Comparison of simulated compaction curves with and without friction . .	55
4.22	Fitted strain gages on the mold	57
4.23	Schematic representation of strain gage locations on the sample	57
4.24	Force vs. radial stress from compaction experiment	58
5.1	SEM micro-graph of alumina graphite powder	60
5.2	Elastic deformation of the testing system	61
5.3	Prepared samples for crush tests	63
5.4	Compaction curves of the crush test samples of 93% relative density . . .	63
5.5	Prepared samples for Brazilian tests	65
5.6	Compaction curves of the Brazilian test samples of 93% relative density .	65
5.7	Prepared samples for calibration through IA	67
5.8	Compaction curve corresponding to configuration-1 to configuration-4 . .	67
5.9	Radial stress curves corresponding to configuration-1 to configuration-4 for middle strain gage	68

5.10 Radial stress curves corresponding to configuration-1 to configuration-4 for bottom strain gage	68
5.11 Tinius Olsen H50KT press for performing destructive tests	69
5.12 Experimental setup of crush test	70
5.13 Experimental setup of Brazilian test	70
5.14 Samples corresponding to 69% to 93% relative density (left to right) subjected to crush test	71
5.15 Samples corresponding to 69% to 93% relative density (left to right) subjected to Brazilian test	71
5.16 Resulting curves of crush test performed on samples of 93% relative density	71
5.17 Resulting curves of crush test performed on samples of 78% relative density	72
5.18 Resulting curves of Brazilian test performed on samples of 93% relative density	72
5.19 Resulting curves of Brazilian test performed on samples of 73% relative density	73
5.20 Averaged failure stress of all samples for crush tests	75
5.21 Averaged failure stress of all samples for Brazilian tests	76
5.22 Experimentally determined cohesion as a function of relative density . . .	78
5.23 Experimentally determined friction angle as a function of relative density	78
5.24 Experimentally determined cap eccentricity as a function of relative density	80
5.25 Experimentally determined evolution pressure as a function of relative density	80
5.26 Experimentally determined hydrostatic yield compression stress as a function of relative density	81
5.27 Experimentally determined Young's modulus as a function of relative density	82
5.28 Effect of transition surface radius on the simulated compaction curve . . .	84
5.29 Experimental vs. computed compaction curves for configuration-1 corresponding to parameters identified through IA employing configuration-1 and -2 as inputs	86

LIST OF FIGURES

5.30	Experimental vs. computed compaction curves for configuration-1 corresponding to parameters identified through IA employing configuration-1 and -2 as inputs	87
5.31	Experimental vs. final compaction computed curve for configuration-3 corresponding to parameters identified through IA employing configuration-1 and -2 as inputs	87
5.32	Experimental vs. final computed compaction curve for configuration-4 corresponding to parameters identified through IA employing configuration-1 and -2 as inputs	88
5.33	Experimental vs. computed compaction curves for configuration-1 corresponding to parameters identified through IA employing configuration-1, -2 and -3 as inputs	90
5.34	Experimental vs. computed radial stress curves (middle gage) for configuration-1 corresponding to parameters identified through IA employing configuration-1, -2 and -3 as inputs	90
5.35	Experimental vs. computed radial stress curves (bottom gage) for configuration-1 corresponding to parameters identified through IA employing configuration-1, -2 and -3 as inputs	91
5.36	Experimental vs. computed compaction curves for configuration-2 corresponding to parameters identified through IA employing configuration-1, -2 and -3 as inputs	91
5.37	Experimental vs. computed radial stress curves (middle gage) for configuration-2 corresponding to parameters identified through IA employing configuration-1, -2 and -3 as inputs	92
5.38	Experimental vs. computed radial stress curves (bottom gage) for configuration-2 corresponding to parameters identified through IA employing configuration-1, -2 and -3 as inputs	92
5.39	Experimental vs. computed compaction curves for configuration-3 corresponding to parameters identified through IA employing configuration-1, -2 and -3 as inputs	93

5.40	Experimental vs. computed radial stress curves (middle gage) for configuration-3 corresponding to parameters identified through IA employing configuration-1, -2 and -3 as inputs	93
5.41	Experimental vs. computed radial stress curves (bottom gage) for configuration-3 corresponding to parameters identified through IA employing configuration-1, -2 and -3 as inputs	94
5.42	Experimental vs. final computed compaction curve for configuration-4 corresponding to parameters identified through IA employing configuration-1, -2 and -3 as inputs	94
5.43	Experimental vs. computed compaction curves for configuration-1 corresponding to parameters identified through IA starting from a different initialization	95
5.44	Experimental vs. computed compaction curves for configuration-2 corresponding to parameters identified through IA starting from a different initialization	95
5.45	Experimental vs. computed compaction curves for configuration-3 corresponding to parameters identified through IA starting from a different initialization	96
5.46	Convergence plot of cohesion for IA starting from 2 different initializations	96
5.47	Convergence plot of hydrostatic yield compression stress for IA starting from 2 different initializations	97
5.48	Convergence plot of Young's modulus for IA starting from 2 different initializations	97
5.49	Schematic representation of configurations -5 to -7	98
5.50	Samples made from alumina-graphite powder along with the required punches to produce configurations -5 to -7 (Left to Right)	99
5.51	Experimental vs. final computed compaction curve for configuration-5 corresponding to parameters identified through IA employing configuration-1, -2 and -3 as inputs	100

LIST OF FIGURES

5.52	Experimental vs. final computed compaction curve for configuration-6 corresponding to parameters identified through IA employing configuration-1, -2 and -3 as inputs	100
5.53	Experimental vs. final computed compaction curve for configuration-7 corresponding to parameters identified through IA employing configuration-1, -2 and -3 as inputs	101
5.54	Comparison of material cohesion assessed from IA vs. experimentally determined values	102
5.55	Comparison of friction angle assessed from IA vs. experimentally determined values	102
5.56	Comparison of cap eccentricity assessed from IA vs. experimentally determined values	103
5.57	Comparison of hydrostatic yield compression stress assessed from IA vs. experimentally determined values	103
5.58	Comparison of evolution pressure assessed from IA vs. experimentally determined values	104
5.59	Comparison of Young's modulus assessed from IA vs. experimentally determined values	104
6.1	Bigoni-Piccolroaz yield surface at three different instances during compaction	110
6.2	Semi logarithmic plot of compact density vs. applied pressure	111
6.3	The influence of amount of mutation to demonstrate capability of algorithm to avoid trapping in local minima	119
6.4	Experimental vs. final computed compaction curve from FE simulation for configuration-1, corresponding to parameters of the novel model identified through IA employing configuration-1, and -5 as inputs	134
6.5	Experimental vs. final computed compaction curve from FE simulation for configuration-5, corresponding to parameters of the novel model identified through IA employing configuration-1, and -5 as inputs	134

6.6	Comparison of compaction curves generated through POD-RBF model and FE simulation for configuration-1, corresponding to parameters of the novel model identified through IA employing configuration-1, and -5 as inputs	136
6.7	Comparison of compaction curves generated through POD-RBF model and FE simulation for configuration-5, corresponding to parameters of the novel model identified through IA employing configuration-1, and -5 as inputs	136
6.8	Experimental vs. final computed compaction curve from FE simulation for configuration-6, corresponding to parameters of the novel model identified through IA employing configuration-1, and -5 as inputs	137
6.9	Experimental vs. final computed compaction curve from FE simulation for configuration-7, corresponding to parameters of the novel model identified through IA employing configuration-1, and -5 as inputs	137
6.10	Evolution of Bigoni-Piccolroaz yield surface during compaction for powder from granular to dense state	139
6.11	Comparison between Drucker-Prager Cap and Bigoni-Piccolroaz yield surface in initial stages of compaction after cohesion starts developing in the powder.	140
A.1	Schematic representation of strain gages pasted on the die-wall	A-2
A.2	Axial stress (= radial stress) vs. circumferential strain for rubber sample .	A-3

This page is intentionally left blank.

List of Tables

4.1	Final parameters corresponding to two different initializations	43
5.1	Experimental details of the compaction tests performed to prepare crush test samples	62
5.2	Experimental details of the compaction tests performed to prepare Brazilian test samples	64
5.3	Experimental details of the compaction tests performed to prepare samples for calibration through IA	66
5.4	Results of the performed crush tests	74
5.5	Results of the performed Brazilian tests	75
5.6	Assessed parameters defining the shear failure surface of DPC yield function	77
5.7	Assessed parameters defining the cap surface of DPC yield function	79
5.8	Assessed Young's modulus corresponding to Poisson's ratio of 0.05 and 0.3	82
5.9	Final parameters corresponding to IA identification employing configuration-1 and -2 as inputs	86
5.10	Final parameters corresponding to IA identification employing configuration-1, -2 and -3 as inputs	89
5.11	Experimental details of the compaction tests performed to prepare samples for configurations -5 to -7	99
6.1	Parameters defining the novel constitutive model	116
6.2	Parameters of the novel constitutive model corresponding assessed through IA employing configuration-1 and -5 as inputs	133

LIST OF TABLES

6.3	Parameters of the novel constitutive model corresponding assessed through IA employing configuration-1 and -5 as inputs	135
6.4	Comparison between the final values of similar parameters for novel constitutive model and DPC model	141

This page is intentionally left blank.

Chapter 1

INTRODUCTION

Production of parts by using powders as starting material, is a vital part of the manufacturing industry. This route finds its applications in many sectors, such as powder metallurgy, production of ceramic components, hard metals, pharmaceutical tablets, detergents, magnets, and others [58]. The popularity of this method of production is derived from several benefits offered by the process such as: possibility to manufacture complex shapes, producing parts of high melting point materials as casting is not a viable option and also, where the two constituents of the system cannot be mixed (e.g. tungsten/copper system) [67].

Production usually comprises of two steps. The first step is the formation of "green body" (compact) by cold compaction which refers to the use of mechanical force to densify the powder so as to give a green body (figure 1.1). The second step is the sintering step, which is consolidation of weakly bonded compact at elevated temperatures, with or without additional pressure [55]. Following the cold compaction, green body should have enough cohesion to remain intact after mold ejection, free of macro defects and handleable for subsequent stages without failure. The presence of defects within the green body can cause local shrinking during the sintering phase, resulting in non-homogeneity of final product, appearance of residual stresses or even formation of macro cracks (see [50, 51]). Such circumstances pose the need for detailed study of cold compaction phase and is a topic of extensive research.

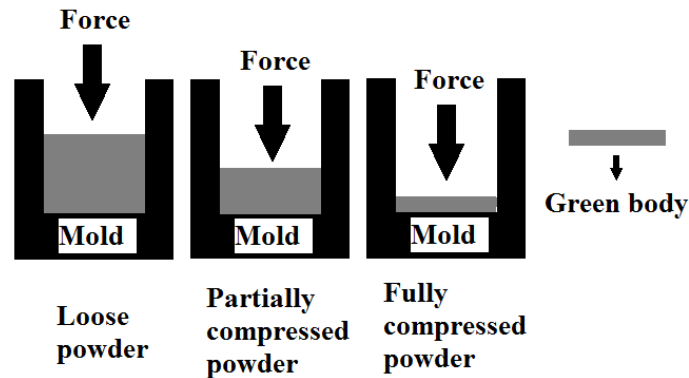


Figure 1.1. Schematic representation of cold compaction

Numerical simulations are increasingly used to better understand the powder compaction process. A successful simulation requires detailed constitutive description of the involved material. In general, one can use either a discrete approach, where it is attempted to separately model particles and their interaction, or continuum approaches where overall macroscopic effects of the powder are studied.

Within discrete approach, each powder particle is treated individually and the contact and friction between the particles are studied [29, 54, 68]. Rojek et al. [54] in their work involving cold compaction of NiAl powder at low pressures (up to 50 MPa), modeled the contact between powder particles following approaches based on elastic Hertz model and plastic Storakers model. The plastic Storakers contact model was deemed more suitable to represent a local interaction associated with yielding at the contact point for particles, however, both models produced very similar macroscopic behavior. In another work by Huang et al. [29], multi-particle finite element simulation was performed on Al/SiC composite powders. The aim of the study was to understand the effects of particle size ratio, initial packing structure and composition on compaction process. This method involved generation of initial packing structure, imported into finite element model, with each particle discretized by finite element meshes. Yan et al. [68] investigated $\text{La}_{0.6}\text{Sr}_{0.4}\text{Co}_{0.2}\text{Fe}_{0.8}\text{O}_3$ (LSCF) cathode which is used in solid oxide fuel cells. The research involved a combination of Discrete Element Method (DEM) with Kinetic Monte Carlo (KMC) simulations. DEM was used to create a number of numerical samples containing spheres or clumped spheres to take into consideration particle size, particle size distribution, aspect ratio, sphericity and orientation generating

distinct powder packings. Further on, a cubic representative volume is sampled from each powder packing and voxelized, serving as starting micro-structure for KMC simulations used to model sintering mechanism.

Clearly, discrete modeling approach can be fairly useful to simulate the physical processes in compaction. However, the difficulty lies in the fact that these models are intrinsically "multi-scale". Such modeling effectively implies that the true experiment is scaled down to a representative volume to enact the original behavior. This leads to several assumptions such as uniform distribution of density over the representative volume, preserving the size ratio and particle distributions etc. Even after such adjustments, the computational burden associated with the modeling is fairly high [53].

Alternatively, continuum based approach can be used to model powder compaction, since from computational point of view, it is better suited for engineering applications [28]. This is related to the fact that even though the powder is clearly discontinuous at particle level, such discontinuity becomes irrelevant when compacting it to a relatively dense state. The use of continuum based approach employs phenomenological models like Cam-Clay, Drucker-Prager, cap plasticity models etc. These models were originally developed for soil mechanics [35], but are extensively used also to model powder compaction [2, 58, 59]. In particular, researchers have established Drucker-Prager Cap (DPC) model as a good constitutive model [28] and most accepted one [26, 31]. This is due to the fact that in DPC model the elliptical cap surface is added to shear failure surface, existing in typical Drucker-Prager model. The shearing phenomenon becomes important during decompression and ejection of powder whereas the cap surface takes into account the densification of the powder [21, 59]. Furthermore, the DPC model is readily available in commercial finite element modeling softwares. Clearly, such modeling necessitates the complete knowledge of constitutive parameters entering the governing equations. The assessment of these parameters is within the main focus of the present research.

1.1 General Motivations

Quantification of material parameters used within constitutive models employed for powder compaction simulation is a challenging task. Current practice relies on performing destructive tests like Brazilian tests, uniaxial compression tests (crush tests), triaxial tests and/or acquisition of stresses from mold used for compaction. Transition from experimentally measured quantities to parameters of interest is done through simplified relations, occasionally representing source of an error. This is evidenced by works of Han et al. [28] and Lamarche et al. [35] on pharmaceutical tablets, Sinha et al. [59] on sensitivity study of DPC model, Almanstötter [2] on doped tungsten powder, Diarra et al. [23] on cosmetic products, Zhou et al. [70] on mixed metal powders and many others [3, 26, 31, 58]. Such experimentations and the related calculations, provide a reasonable estimate of the parameters but they involve large number of experiments, particularly when the number of constitutive parameters is elevated. Another complication comes from the fact that during compaction a loose powder transforms into a dense solid and these two states have fairly different mechanical behaviour. Such transition must be accounted for in the modeling.

From mechanical point of view, the above mentioned transition implies that the governing parameters should change with progressing of compaction. When continuum based approach is used, which is the strategy adopted in this research, it is common to relate relative density to volumetric plastic strain, as the internal state variable of the model. It is therefore required to define parameters which are changing with accumulated plastic strain. This is not a straightforward task since, for example, in the classic form of DPC model hardening affects only "cap" parameters, while it assumes fixed shear failure surface. Similar holds also for other plasticity models.

During the powder compaction, the values of most of the parameters change as the relative density of the compact increases. This has been evidenced in [21, 28] for example and can be visualized in the figure 1.2 (note the changing slope of the unloading branch at different density levels) and figure 1.3 (shear surface also shifts along with the growing cap surface). It is therefore needed to introduce a so called "elasto-plastic" coupling, where also the elastic properties will depend on accumulated plastic strain.

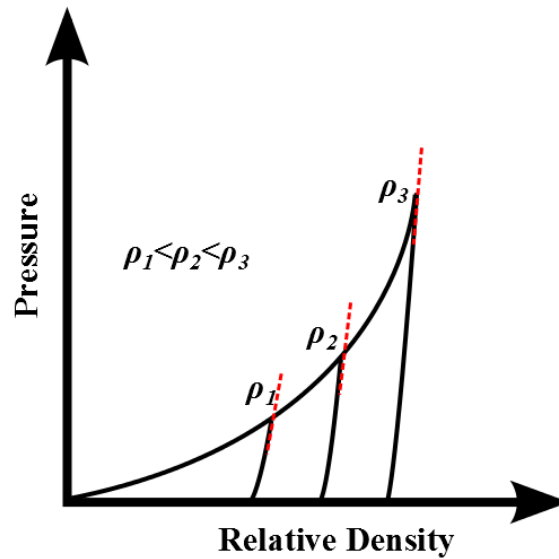


Figure 1.2. Unloading phase of powder compaction at different relative densities evidencing change in elastic properties as compaction progresses

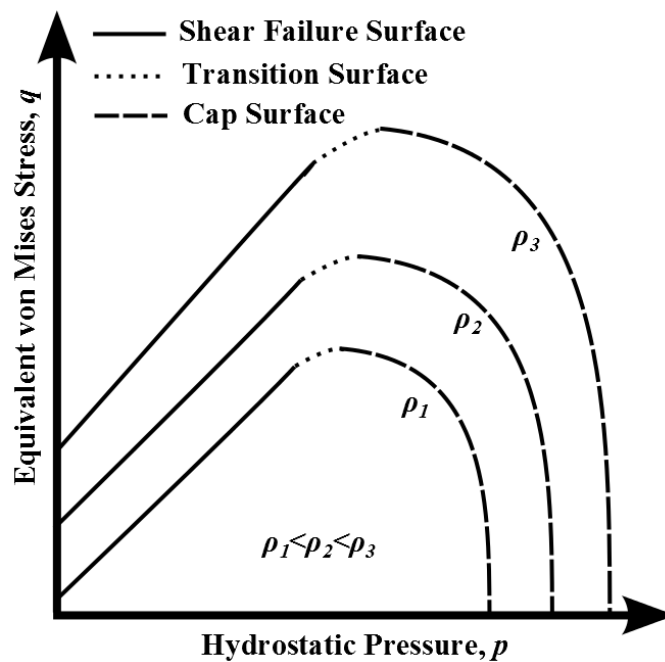


Figure 1.3. Representation of changes in plastic property with changing relative density evidenced by shift in DPC yield surface

As a possible remedy to the above mentioned limitations, some authors have introduced and numerically implemented the field dependency of constitutive parameters within continuum models (refer to [2, 3, 23, 26, 28, 31, 35, 58, 59, 70]). It assumes constitutive parameters as a function of volumetric plastic strain, thereby enabling to

incorporate also the elasto-plastic coupling. For compaction, relative density is derived from the plastic strain and is treated as the solution dependent variable making it possible to have parameter definition as a function of relative density. Clearly, such modifications significantly affect the calibration procedure, since constitutive parameters change as the density increases. Thus, the required number of experiments on green bodies significantly increases. This circumstance creates the need for heavy experimental protocol, making the industrial routine application rather difficult and fairly expensive. Furthermore, some of the parameters cannot be determined by the conventional experimental route of calibration at relatively low and high densities [26]. In a view of the listed difficulties, the research is motivated on finding an alternative procedure for the calibration of constitutive models for powder compaction without involving such heavy experimental regime.

1.2 Primary Objectives

The primary objective of the thesis is to develop a full characterization procedure to determine the evolution of properties of the green body as a function of relative density, throughout the cold compaction based on the Inverse Analysis (IA) methodology. The IA approach synergically combines the experiments with numerical simulations and mathematical programming for minimization of discrepancy between experimentally measured quantities and their computed counterpart [13]. The novelty pursued relies on the development of calibration protocol depending only on experimental quantities collected from compaction test, and therefore excluding all the heavy experimentation needed for evaluating the properties of green body. Such characterization is obviously more appropriate for industrial applications and could lead to, hopefully important, reduction of rejected pieces, as more information is available on the green body before it subsequently undergoes sintering, leading to obvious economical and environmental advantages.

To achieve this goal, numerical implementation of the DPC model, capable of taking into account the elasto-plastic coupling together with other sources of non-linearities observed from the experiments is done. The implemented model is optimized

specifically for ceramic powders. After the successful development of the model with the required features, a calibration procedure based on IA is setup. The evaluated parameters from the IA are verified against the values obtained from traditional route of performing experiments within an extensive testing campaign. As the final step, the assessed parameters are fed to the developed constitutive model and the results are tested on compaction of industrial powder, for a few different geometries.

1.3 Outline of the Method

Central methodological ingredient of developed calibration procedure represents the Inverse Analysis (IA). The IA approach has already been successfully implemented in different fields, like, material characterization based on instrumented indentation [14, 16], identification of stress states and elastic properties of concrete dams using flat jack tests [25], determination of boundary temperatures and heat flux for a steady state heat conduction problem [69], shape optimization of transonic airfoil [37], quantification of unknown impact forces on a beam [65] and many others [8, 10, 11, 22, 48, 61].

The focus of this research is to implement IA in the present context of calibrating models for simulation powder compaction based only on the data collected during compaction experiment (e.g. using force vs. displacement curve). The developed procedure is tested with reference to DPC model, however, the methodology can be extended to the calibration of other models as well. In fact, with some modification the developed methodology is also applied to the calibration of more sophisticated model based on Bigoni-Piccolroaz yield criterion [49, 51].

One of the key ingredients required for IA includes the simulation of experiment. To this purpose, the DPC model in its classic form is modified to include dependency of constitutive parameters on the relative density. The selection of the experiment plays an important role within the IA protocol, as it is of primary importance that all the sought parameters are sensitive to the selected measurable quantities. To ascertain this, systematic sensitivity analyses are performed through numerical simulations of experiment. Different mold geometries are considered to optimize the overall experimental protocol. Once the experiment is selected and the measurable quantities are

available from both the experiment and its numerical model, a discrepancy function is formed to quantify the difference between the experimentally measured quantities and their computed counterparts. This discrepancy function is further minimized using mathematical programming techniques within an iterative procedure to give the required parameters.

1.4 Organization of the Thesis

Chapter 2 presents an overview of the currently adopted praxis to calibrate the models used in powder compaction. In particular the reference is made to Drucker-Prager Cap (DPC) model, which is described with the relevant equations. This is followed by the detailed description on the evaluation of model parameters through crush tests, Brazilian tests and acquisition of radial stress.

In Chapter 3, the methodology based on Inverse Analysis (IA) is introduced. A brief description of the compaction experiment with the testing machine used for it is given. Following this, the general aspects of the compaction simulation are presented with the specific details on the implementation of the "modified" DPC model. Finally at the end of the chapter, a survey of most frequently employed algorithms for constrained minimization of the discrepancy function is outlined.

Chapter 4 describes the proposed calibration protocols. A sensitivity study is presented, which is used to establish different mold geometries for compaction to optimize the overall experimental protocol.

In Chapter 5, comparative results of the developed calibration procedure based on IA and current praxis are presented with reference to the DPC model. At the beginning of the chapter, the relevant experimental details of the compaction test for the production of green bodies, for both flat cylindrical and modified mold geometries is mentioned. The destructive tests on the former is used to establish reference values of parameters through the procedure employed as current praxis, while the data from the compaction tests of the latter is selected for IA identification. Following this, the comparison between the assessed values on the basis of these two approaches is given. Finally at the end of the chapter, the designed calibration protocol based on IA is summarized.

Chapter 6 deals with the application of the developed IA procedure to calibrate a more sophisticated material model relying on Bigoni-Piccolroaz yield criterion. This novel constitutive model is outlined with the relevant equations. The main features of the Genetic Algorithm (GA) which is used for the minimization of the discrepancy function is further presented. Following this, reduced basis model based on proper orthogonal decomposition is introduced to significantly reduce the associated computational burden from recursive simulations required by GA. Finally, the developed calibration procedure combining the reduced basis models with genetic algorithm is explained and the obtained results are discussed and comparisons between novel model and DPC model are shown.

Chapter 7 concludes the thesis with final remarks and suggestions for potential future research.

Chapter 2

CURRENT CALIBRATION PROCEDURES FOR POWDER COMPACTION MODELS

The current method of quantifying constitutive parameters entering the models used in powder compaction relies on performing experiments on the green body. Recently, Diarra et al. [24] performed a comparative study between "modified" Cam-Clay (CC) model and "modified" Drucker-Prager Cap (DPC) model (modification so to include the elasto-plastic coupling). For the modified CC model, the radial stresses measured from the die-wall were used for evaluating the slope of critical state line (M), the size of the yield surface (a) and the hydrostatic yield stress (p_c). However, the modified CC model can only be used to study densification and cannot take into account the failure behavior (for example, the failure during ejection). Thus, DPC model must be selected to model such behavior along with the densification and in fact, is the most accepted model for powder compaction for different categories of materials, such as pharmaceutical tablets [21, 28], ceramic powders [58], metal powders [2, 70], cosmetic products [23] etc. In what follows, a brief description of the DPC model is outlined, proceeded by presenting the procedure employed for the identification of its governing parameters.

2.1 The Drucker Prager Cap Model

Graphical representation of DPC yield surface in p - q plane is visualized in figure 2.1. As indicated in the figure, p represents a hydrostatic pressure and q , the equivalent von Mises stress, namely:

$$p = \frac{\sigma_{xx} + \sigma_{yy} + \sigma_{zz}}{3} \quad (2.1)$$

$$q = \sqrt{\frac{(\sigma_{xx} - \sigma_{yy})^2 + (\sigma_{yy} - \sigma_{zz})^2 + (\sigma_{zz} - \sigma_{xx})^2 + 6(\sigma_{xy}^2 + \sigma_{yz}^2 + \sigma_{zx}^2)}{2}} \quad (2.2)$$

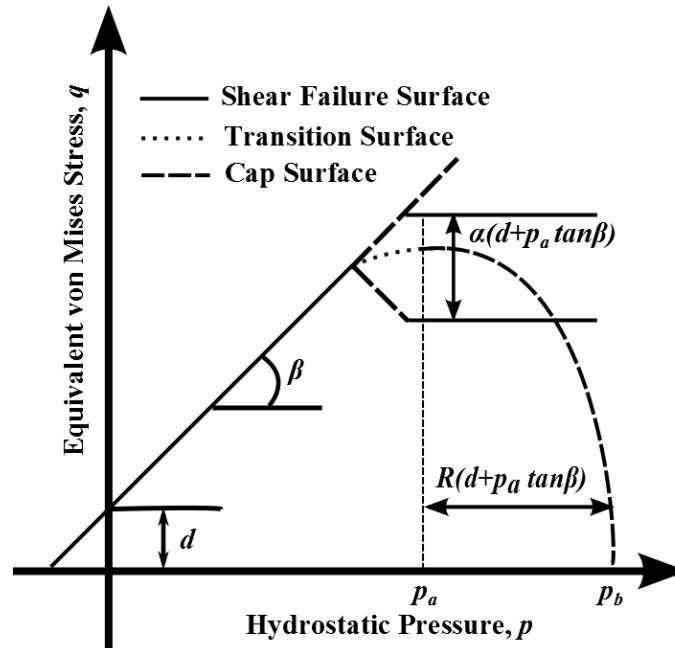


Figure 2.1. The DPC yield surface in p - q plane

In addition to the shear failure surface in the DP model in its classic form, here, a cap surface is added to take into account yielding due to hydrostatic stress only. In the DPC yield function, the elastic domain is enclosed by three surfaces, namely shear failure surface, cap surface and transition surface (from shear to cap surface). The shear failure surface is the boundary between the stress state that causes dilation and shape changes and usually determines the failure of the compact. The densification and hardening is

controlled by the expanding cap surface, governed by volumetric plastic deformation. The third surface ensures a smooth transition between the shear and the cap surface to avoid numerical instabilities. The parameters that define these surfaces are as follows:

- Shear failure surface (F_s) is defined through material cohesion (d) which is an indicator of the shear strength, and friction angle (β) through the following expression:

$$F_s = q - p \tan \beta - d = 0 \quad (2.3)$$

- Cap surface (F_c) is governed by evolution pressure (p_a) and parameter R , which controls the shape of the cap surface (usually known as cap eccentricity). Therefore, cap surface is defined by:

$$F_c = \sqrt{(p - p_a)^2 + \left(\frac{Rq}{1 + \alpha - \frac{\alpha}{\cos \beta}} \right)^2} - R(d + p_a \tan \beta) = 0 \quad (2.4)$$

- Transition surface (F_t) is defined by transition radius (α):

$$F_t = \sqrt{(p - p_a)^2 + \left[q - \left(1 - \frac{\alpha}{\cos \beta} \right) (d + p_a \tan \beta) \right]^2} - \alpha(d + p_a \tan \beta) = 0 \quad (2.5)$$

Hardening is described by hydrostatic yield compression stress (p_b) as a function of volumetric plastic strain (ε_p^v). Here, p_b is the magnitude of stress needed to compact the material using hydrostatic stress alone. It can be calculated using the values of d , β , p_a and R such that:

$$p_b = p_a (1 + R \tan \beta) + Rd \quad (2.6)$$

In compaction modeling, the volumetric plastic strain plays the role of relative density of the compact and the correlation between the two can be given by:

$$\varepsilon_p^v = \ln \left(\frac{\rho}{\rho_0} \right) \quad (2.7)$$

where, ρ and ρ_0 are the current and initial relative density respectively.

In addition to the yield function, the plastic flow rule is defined. The plastic potential is defined by an associative component (G_c) on the cap surface whereas, a non-associative component (G_s) is used for shear failure surface and transition regions, shown in equations below:

$$G_c = \sqrt{(p - p_a)^2 + \left(\frac{Rq}{1 + \alpha - \frac{\alpha}{\cos \beta}} \right)^2} \quad (2.8)$$

$$G_s = \sqrt{[(p - p_a) \tan \beta]^2 + \left(\frac{q}{1 + \alpha - \frac{\alpha}{\cos \beta}} \right)^2} \quad (2.9)$$

To uniquely define the DPC yield function, a total of five parameters are required, namely: cohesion (d), friction angle (β), transition surface radius (α), evolution pressure (p_a), cap eccentricity (R). The transition surface radius (α) is typically a small number between 0.01 and 0.05 and is assumed as a constant value throughout the compaction (for example, $\alpha = 0.02$ in [3, 28], 0.03 [23]). In what follows, the current procedure employed for identification of the rest of parameters is laid out.

2.2 Current Practice for Calibration of DPC Model

In the works carried out so far, the governing parameters of the DPC yield criterion are evaluated using experiments on green body. Han et al. [28] in their study of die-compaction simulation of pharmaceutical powders, assessed the material cohesion (d) and friction angle (β) by using Brazilian disc test (diametrical compression) along with uniaxial compression test (crush test). The samples of different densities were formed and tested, so as to give the evolution of these parameters over the range of relative density. The cap surface parameters, namely: evolution pressure (p_a) and cap eccentricity (R), were found out by forming green bodies at different densities and

analyzing the loading path of the involved compaction tests. These values were then used to calculate hydrostatic yield compression stress (p_b). Shang et al. [58] in their study tried to quantify the effect of deformation of the punches on the evaluated parameters of the DPC model. For the assessment of shear failure surface, Brazilian disc test along with uniaxial compression test were employed. The parameters of the cap surface were estimated using measurements from axial and die-wall stresses. In another research conducted by Cunningham et al. [21] analyzing tablet compaction, similar approach was used to find the shear failure surface. The work carried out by Sinha et al. [59] on the sensitivity of DPC parameters during decompression phase, also relied on the methodology mentioned above for quantifying constitutive parameters.

In the more recent works, LaMarche et al. [35] performed studies for a range of excipients and formulated products. The material cohesion and friction angle were evaluated using Brazilian disc test and uniaxial compression test. The values of material cohesion and friction angle were used along with die wall stress and axial stress to quantify evolution pressure, cap eccentricity and hydrostatic yield stress. Garner et al. [26] proposed a scheme to extrapolate parameters for the relative densities that are not accessible experimentally so as to cover a full range from initial relative density to a relative density of unity. To carry out the extrapolation, the parameters were identified at some particular densities using the tests mentioned above. Almanstötter [2] in his study of doped tungsten powder, Diarra et al. [23] in their work on compaction of cosmetic products, Kadiri and Michrafy [31] in their research on effect of punch shape in powder compaction process, employed the above mentioned techniques to characterize the plastic parameters of the DPC model.

In the previous studies, shear failure surface parameters are assessed on the basis of Brazilian disk tests and uniaxial compression tests, while cap surface parameters are quantified through measuring radial stress on the die wall and analyzing the loading path during compaction, whereas the elastic parameters were evaluated from the unloading curves of radial stress vs. axial stress and axial stress vs. axial strain. In what follows, the description of the above mentioned methodologies and their application to identify the constitutive parameters is given.

2.2.1 Shear Failure Surface Characterization

The most common method to characterize the shear failure surface involves carrying out Brazilian test and crush test [2, 21, 23, 26, 28, 31, 35, 58, 59, 70]. These tests exhibit shear in two different loading patterns and thus offer a good combination to determine the shear failure surface, which is represented by a line in 2-dimensional p - q space. In the Brazilian disk test, a disc shape specimen is loaded by two opposing normal strip loads at the disc periphery. The schematic representation is shown in figure 2.2. The load is continuously increased at a constant rate until the failure occurs. The load at which the specimen fails (maximum load L) is then in turn used to calculate the failure limit (σ_d) of the sample using following formula:

$$\sigma_d = \left(\frac{2L}{\pi DH} \right) \quad (2.10)$$

where D is the diameter and H is the height of the sample respectively.

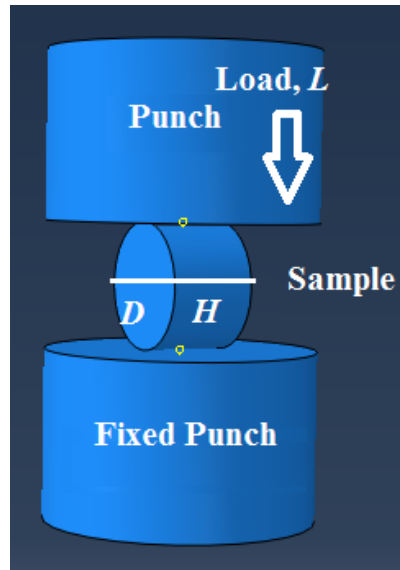


Figure 2.2. Brazilian test setup

The crush test gives the stress vs. strain evolution of the green body using uniaxial compression. The experimental setup is shown in figure 2.3. In the crush test, a cylindrical sample is compressed until failure. As can be seen in the figure, one of the punches is kept fixed, whereas the other punch applies load. The force and the displacement are recorded

and failure load (F_m) is picked from this curve. This is then used to compute failure stress (σ_c) using diameter of the sample (D) by the following equation:

$$\sigma_c = \left(\frac{4F_m}{\pi D^2} \right) \quad (2.11)$$

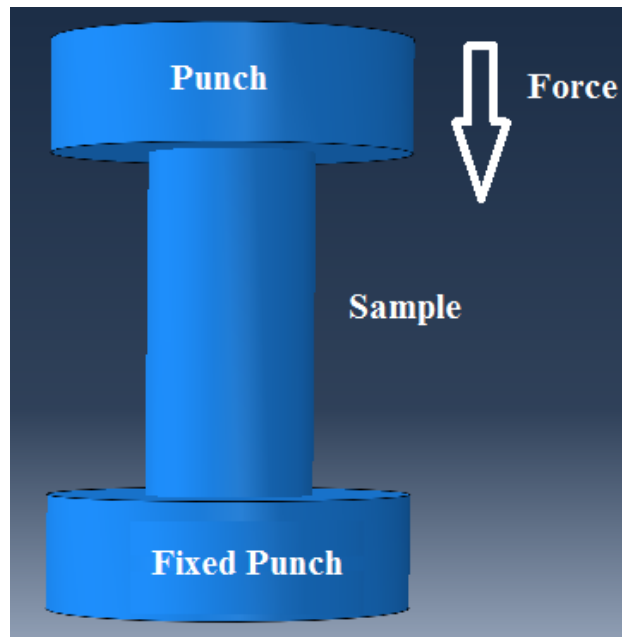


Figure 2.3. Crush test setup

The combination of Brazilian test and crush test is used to determine the shear failure line as can be visualized in the figure 2.4. These two tests give two points on the shear failure line, which in turn gives the cohesion as the intersection with y -axis, and friction angle as the slope of this line. The equations used to calculate the points of shear failure starting from stress values (σ_d) and (σ_c) are given below.

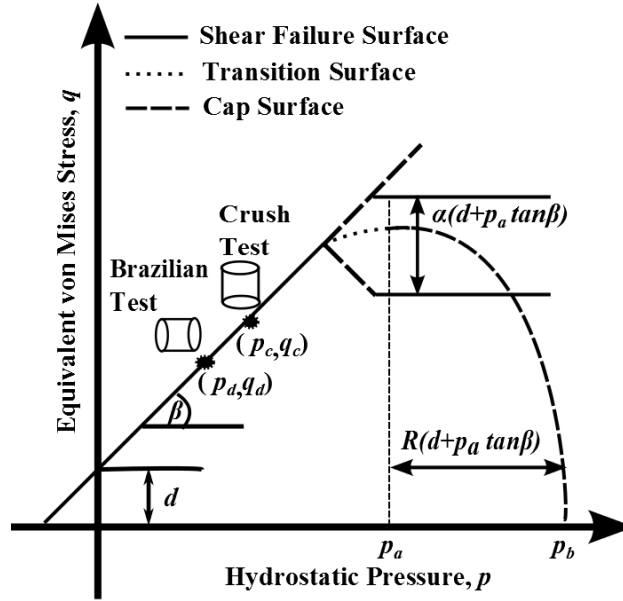


Figure 2.4. Schematic representation of different tests needed for calibration of shear failure line DPC yield criterion

In the Brazilian test, the stress state can be represented as:

$$p_d = \left(\frac{2\sigma_d}{3} \right) \quad (2.12)$$

$$q_d = \left(\sqrt{13}\sigma_d \right) \quad (2.13)$$

whereas, in the crush test it is given by:

$$p_c = \left(\frac{-\sigma_c}{3} \right) \quad (2.14)$$

$$q_c = (-\sigma_c) \quad (2.15)$$

Using these equations, the material cohesion (d) and friction angle (β) can be deduced through the formulae given below:

$$d = \left(\frac{\sigma_d \sigma_c \sqrt{13 - 2}}{\sigma_c + 2\sigma_d} \right) \quad (2.16)$$

$$\beta = \tan^{-1} \left(\frac{3\sigma_c + d}{\sigma_c} \right) \quad (2.17)$$

From what precedes, it can be realized that the evaluation of cohesion and friction angle at a particular level of density requires two compaction tests and two destructive tests (Brazilian and crush). It is reasonable to perform these tests at least twice at a particular density level to check and establish reciprocity of results. This effectively means that characterizing cohesion and friction angle at a single density point, involves in total minimally eight experiments. Such characterization needs to be done at an elevated number of densities (say, five or more) to have a reasonable estimate of parameters over the range of relative density.

2.2.2 Cap Surface Characterization

The cap surface parameters are obtained by analyzing the stress state of the loading point (A). The intersection of loading path OA (see figure 2.4) with the cap surface gives the maximum value of axial stress and radial stress. The radial stress is measured from the die-wall during compaction, usually, by employing strain gages and calibrating them details on which can be found in appendix A. Axial stress can be recorded from the testing machine used to perform compaction.

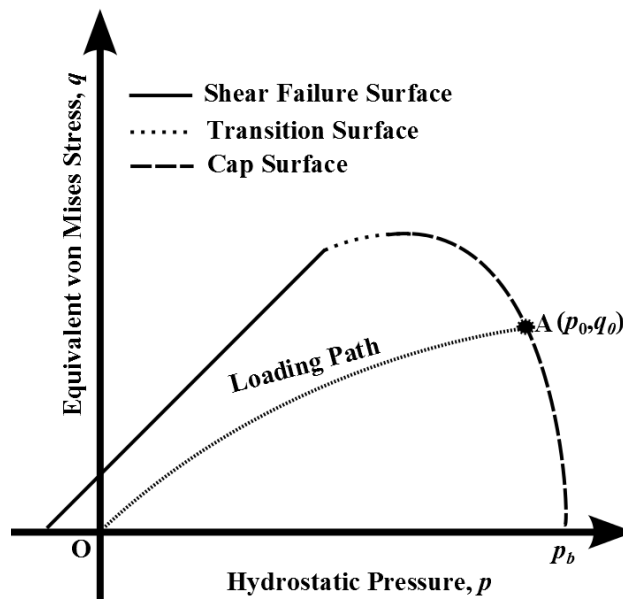


Figure 2.5. Visualization of loading path in compaction test

The available values of axial stress (σ_z) and radial stress (σ_r) are then converted to hydrostatic pressure (p_0) and equivalent mises stress (q_0) by the following relations:

$$p_0 = \left(\frac{\sigma_z + 2\sigma_r}{3} \right) \quad (2.18)$$

$$q_0 = |\sigma_z - \sigma_r| \quad (2.19)$$

With an assumption that the die-wall is rigid, the radial strain rate at point A is null and can be denoted as:

$$\dot{\epsilon}_r^p = \dot{\lambda} \left. \frac{\partial G_c}{\partial \sigma_r} \right|_{(p_0, q_0)} = 0 \quad (2.20)$$

Given that $\dot{\lambda}$ is a positive quantity in equation (2.20), it implies:

$$\left. \frac{\partial G_c}{\partial \sigma_r} \right|_{(p_0, q_0)} = 0 \quad (2.21)$$

By using (2.8) and (2.21), the cap eccentricity (R) can be determined and is given as:

$$R = \sqrt{(p_0 - p_a) \frac{2 \left(1 + \alpha - \frac{\alpha}{\cos \beta} \right)^2}{3q_0}} \quad (2.22)$$

Substituting value of R from equation (2.22) into (2.4), evolution pressure (p_a) can be computed as:

$$p_a = \frac{\sqrt{9q_0^2 + 24dq_0 \left(1 + \alpha - \frac{\alpha}{\cos \beta}\right)^2 \tan \beta + 8(3p_0q_0 + 2q_0^2) \left[\left(1 + \alpha - \frac{\alpha}{\cos \beta}\right) \tan \beta\right]^2}}{\left[\left(1 + \alpha - \frac{\alpha}{\cos \beta}\right) \tan \beta\right]^2} - \frac{\left[3q_0 + 4d \tan \beta \left(1 + \alpha - \frac{\alpha}{\cos \beta}\right)\right]^2}{\left[\left(1 + \alpha - \frac{\alpha}{\cos \beta}\right) \tan \beta\right]^2} \quad (2.23)$$

Once the compaction is finished, compact's relative density can be measured using the volume of the sample and the absolute density of the material. This in turn can be used to compute the volumetric plastic strain using equation (2.7). The hydrostatic yield compression stress (p_b) can be calculated using formula (2.6) and hardening law can be defined.

From the above given relations, the cap surface can be fully determined at a particular relative density. This needs to be done for multiple compacts, formed at different density levels, to evaluate the cap surface and the hardening of DPC yield criterion.

2.2.3 Evaluation of Elastic Properties

The elastic behavior of compacting powder is assumed to be isotropic [2, 23, 31, 70]. Thus, only two elastic parameters, namely Young's modulus (E) and Poisson's ratio (ν) need to be evaluated. The elastic constants E and ν are related to the bulk modulus (K) and shear modulus (G), describing the elastic behavior under hydrostatic stress and shear stress, respectively. This can be expressed as:

$$K = \frac{E}{3(1 - 2\nu)} \quad (2.24)$$

$$G = \frac{E}{2(1 + \nu)} \quad (2.25)$$

In the elastic range, the behavior of isotropic materials is governed by the Hooke's law, which in incremental form reads:

$$d\mathbf{e}_{ij}^e = \frac{dI_1}{9K}\delta_{ij} + \frac{d\mathbf{s}_{ij}}{2G} \quad (2.26)$$

where, $d\mathbf{e}_{ij}^e$ is the elastic strain increment, I_1 is the first stress invariant, δ_{ij} is the Kronecker delta and \mathbf{s}_{ij} ($\sigma_{ij} - I_1/3$) is the deviatoric stress tensor. In the compaction test, the die-wall is assumed to be rigid, implying:

$$\varepsilon_r = \varepsilon_\theta = 0 \quad (2.27)$$

$$\sigma_r = \sigma_\theta \quad (2.28)$$

here, ε_r , ε_θ , σ_r and σ_θ is radial strain, hoop strain, radial stress and hoop stress, respectively. Using (2.27) and (2.28), axial strain increment can be computed from equation (2.26) as:

$$d\varepsilon_z = \frac{d\sigma_z + 2d\sigma_r}{3K} = \frac{dp}{K} \quad (2.29a)$$

$$d\varepsilon_z = \frac{d\sigma_z - d\sigma_r}{2G} = \frac{dq}{2G} \quad (2.29b)$$

The relationship between stress and strain can be expressed using the Young's modulus such that:

$$d\sigma_z = \frac{E}{(\nu + 1)(2\nu - 1)} [(\nu - 1) d\varepsilon_z] \quad (2.30a)$$

$$d\varepsilon_z = \frac{d\sigma_z - \nu(2d\sigma_r)}{E} \quad (2.30b)$$

since, $\varepsilon_r = \varepsilon_\theta = 0$ and $\sigma_r = \sigma_\theta$. Substituting, values of $d\varepsilon_z$ (2.29) and K (2.24) into the above formula (2.30a), the following relation can be obtained:

$$d\sigma_z = \frac{(1 - \nu)}{\nu} d\sigma_r \quad (2.31)$$

Using the value of $d\sigma_r$ from (2.31) and G from (2.25), and putting it into equation (2.30b), following can be expressed:

$$d\sigma_z = \frac{E(1 - \nu)}{(1 + \nu)(1 - 2\nu)} d\varepsilon_z \quad (2.32)$$

The value of Poisson's ratio can be calculated from (2.31) by using the slope of unloading curve of axial stress vs. radial stress. For the Young's modulus, slope of the axial stress vs. axial strain needs to be plugged into equation (2.32). This needs to be repeated at multiple level of densities.

From the above characterization procedure, it is obvious that multiple tests need to be performed. To put more light on this, the full characterization of DPC model at a particular level of density requires ten experiments (eight for shear failure line, two for cap and elastic parameters) in the minimum case scenario. Thus, to calibrate a density dependent DPC model which will require parameters to be defined as a function of relative density, one should perform about fifty experiments for evaluating constitutive parameters at five different levels of relative density. It is abundantly evident that such procedure for calibration is very heavy experimentally and not so feasible for routine industrial purposes. Similar heavy experimental regime can be expected with other models for powder compaction simulations. Therefore, such circumstances invoke the need for an alternative route to calibrate the models used for powder compaction and can be tackled using the methodology based on IA presented in Chapter 3.

Chapter 3

ON INVERSE ANALYSIS, POWDER COMPACTION SIMULATION AND RELATED NOVELTIES

In present research, the material constants entering the models employed in powder compaction are evaluated through Inverse Analysis (IA). These are analyses performed backwards, meaning that the solution is known but not the causes leading to it. As opposed to commonly used direct analysis, here, the full result of the forward problem is at the disposal, while the complete knowledge of all the inputs, namely, initial/boundary conditions, geometry details, constants (constitutive parameters entering governing equations) etc. is not available. Such problems are referred to as the "inverse problems" and they are tackled within the growing branch in applied mechanics under the name of inverse analysis [13, 63, 64].

The IA methodology synergically combines the experiment, its simulation and mathematical programming. The idea is to perform the experiment along with its simulation, and record the measurable quantities from both. The difference between these measured values is estimated within, what is called a discrepancy function. As the final step, this function is minimized with respect to the sought quantity of interest. The flow of the IA procedure is visualized in figure 3.1. For more details on the subject, refer to [13, 63, 64].

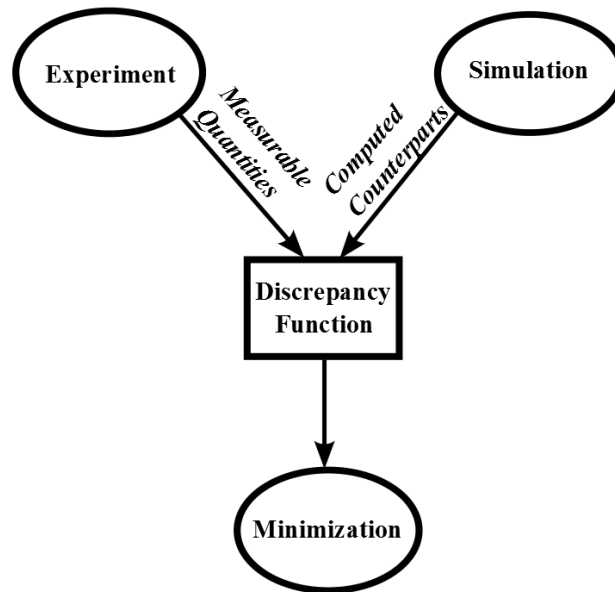


Figure 3.1. Schematic representation of IA procedure

Over the last two decades, IA methodology has seen diverse applications in multiple areas. These range from determination of initial/boundary conditions [65, 69] to shape optimization [37, 61] and parameter identifications [10, 14, 25]. For example, Wang and Chiu [65], employed IA to quantify the impact force on a beam, using experimentally measured accelerations. In the work carried out by Sobieczky and Center [61], the shape of the airfoil was optimized, respecting the geometry constraints, based on target pressure distribution, used as the input data. Damasceno and Fratta [22], monitored the chemical diffusion in a porous media using electrical resistivity tomography. Sodium chloride solution was seeped in the porous media and electrical currents and voltages were measured at the boundaries, helping to make electrical resistivity tomographic images. Similar kind of study was done on sandy soils by Borsic et. al. [11] using water as the conductor. Ostrowski et. al. [48] evaluated the heat conductivity and the heat transfer coefficient utilizing the temperature field measurements. In another research, Bolzon et. al. [10] used the indentation curve and the imprint of the indenter on the specimen under test, to assess the sample's mechanical properties, such as Young's modulus, yield limit and exponent of hardening. In more recent works, Xie et. al. [66] estimated the endothermic reaction parameters like thermal conductivities, reaction temperature and heat, making use of the temperature history curves. In a research by Nakamura et. al. [44], a prediction of transient heat flux during aerodynamic heating

was done relying on finite temperature data points. Liang et. al. [38] estimated the inherent deformation in thin plate aluminum alloy joints during welding. Shrinkage and bending in longitudinal and transverse directions were determined using the measurements of deformations at limited locations.

From what precedes, it can be realized that the IA procedure is increasingly employed in diverse fields of engineering. The common point in all these applications is that the quantity of interest is evaluated on the basis of some experimentally measured data. Clearly, such strategy offers an important advantage for assessing quantities difficult, or even impossible to measure otherwise. This feature of the methodology is particularly important for determination of parameters entering complex constitutive models. The current research focuses on these kinds of problems.

By observing literature one can find many recent applications of IA methodology employed for the assessment of material parameters. Fedele and Maier [25], identified the stress states and the elastic properties of concrete used in dam structures. Flat jack was inserted into the concrete and reference points were marked. The device was then pressurized, and consequent variations in distances of these marked reference points was measured and fed as an input for IA procedure. Applying similar principles, Chisari et. al. [20] evaluated the material parameters of mortar joints in unreinforced masonry. Buljak and Maier [15] in their research, showed the possibility to quantify residual stresses in the material based on indentation tests alone. Elliptical indenters of novel shape were proposed and the obtained indentation curve was used as an input to the IA procedure. In a study performed by Magalhaes et. al. [40], the Young's modulus of a cantilever beam made of ASTM A36 steel was estimated from the displacement of the structure. Jiang et. al. [30] quantified linear and nonlinear elastic properties of porcine brain tissue. The ultrasonic probe was pushed into the soft tissue, which generated an acoustic radiation force inducing plane shear waves. The velocity of these waves was employed as input to the IA procedure. Chen et. al. [19] evaluated the cohesive model parameters for crack growth simulations by analyzing the key points on the load-crack extension experimental curve. Based on a similar approach, Buljak and Maier [12], designed novel shape of sharp indenters to be specifically used for calibration of fracture properties of brittle materials. Li et. al. [36] employed the IA procedure to determine the

material models for work hardening and dynamic recovery. Bainite steel was subjected to hot compression tests at high temperatures (1100°C-1400°C) at varying strain rates. The obtained stress-strain curve was then used to evaluate the material constants of the established constitutive equations to predict work hardening and recovery. Bolzon et. al. [9] characterized aluminum-based metal matrix composites relying on the data of indentation test. The material behavior was modeled through Drucker-Prager constitutive model and parameters were determined by IA.

In a view of recent developments of inverse analysis methodology, and the complications involved in evaluating parameters of constitutive models for compaction, the research is motivated in employing IA within the present context considered in this thesis. The difficulty with characterizing constitutive parameters for compaction modeling is derived from their elevated number and the way they change throughout pressing. These circumstances make the application of IA procedure more challenging, however, offering important benefits by eliminating the need for heavy experimental regime described in the previous chapter. In the light of these potential novelties, IA procedure is adopted as the central methodology in this research work.

For applying such concept to determine parameters entering the governing equations, die compaction tests are performed. A compaction curve, which is a typical output of this experiment, is considered as experimental data \mathbf{U}^{exp} . The same experiment is further simulated using the commercial Finite Element (FE) code ABAQUS [1] to give the computed data \mathbf{U}^{com} . These measurements are used to form the residual vector \mathbf{R} :

$$\mathbf{R}(\mathbf{p}) = \mathbf{U}^{exp} - \mathbf{U}^{com}(\mathbf{p}) \quad (3.1)$$

Further on, a discrepancy function ω is formulated:

$$\omega(\mathbf{p}) = \mathbf{R}^T \cdot \mathbf{R} = [\mathbf{U}^{exp} - \mathbf{U}^{com}(\mathbf{p})]^T [\mathbf{U}^{exp} - \mathbf{U}^{com}(\mathbf{p})] \quad (3.2)$$

Parameter set that minimizes discrepancy function (3.2) represents the solution of the inverse problem. To reach a numerical solution of this minimization problem, a suitable mathematical programming algorithm is usually employed.

From the above outline, it is clear that there are three crucial ingredients in constructing the IA procedure: (1) the selection of the experiment, with proper measurable quantities collected from it; (2) numerical simulation of the formulated experiment and (3) the employment of appropriate iterative algorithm. In what follows, all these ingredients are briefly discussed in the present context.

3.1 Compaction: Experiment and its Simulation

3.1.1 Experiment

The experiment to be considered within the inverse analysis is the compaction (pressing) test itself. An attempt is made to define punch/mold (or die) geometry as simple as possible, considering first the simplest cylindrical specimen formed through pressing test performed in uniaxial strain regime. During the compaction, loose powder particles are compressed in a die cavity by the application of pressure, to form a solid green body of relatively high density, that conforms to the shape of the mold used. The pressure is applied along one axis, whereas, the cavity into which the powder is pressed gives it a lateral constraint. To perform compaction, the powder is filled in a corrosion resistant steel mold. A combination of a movable punch along with a fixed one is subjected to a force, which is then transferred to the powder.

For the purpose of applying force, an "Instron" testing machine (servo-hydraulic) is used in this research. This machine has a maximum load capacity of 600 kN and an uncertainty of less than 0.5% in measuring the applied force. The experimental setup is visualized in the figure 3.2, with reference to cylindrical green body, shown in the bottom part of the figure.

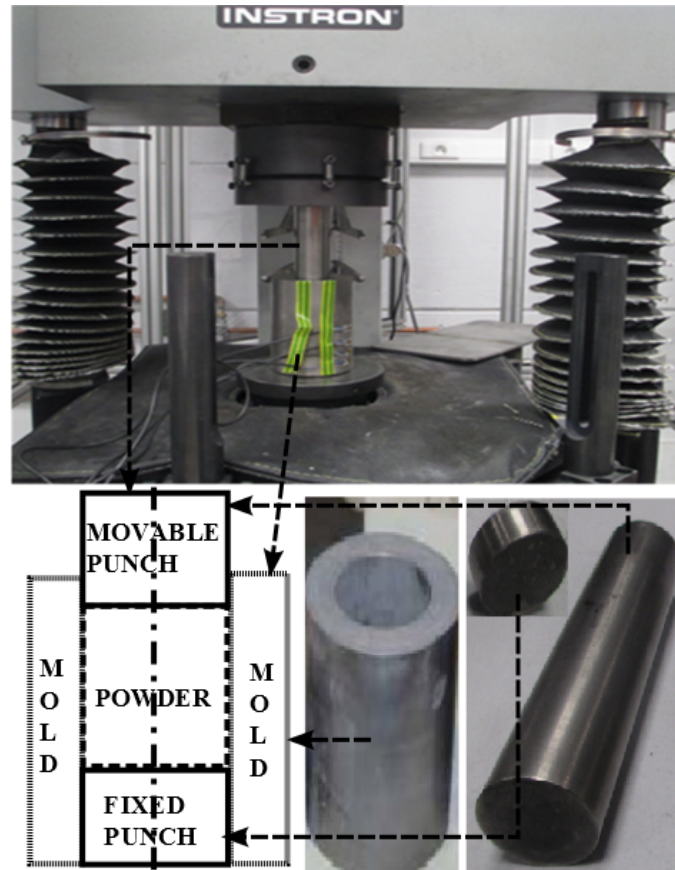


Figure 3.2. Experimental setup of compaction test

The force applied during the compaction vs. the displacement of the punch, can be recorded from the machine and typically, has the form given in figure 3.3. This curve is selected as the main measurable quantity from the experiment, to be used as an input within the IA procedure. The solution of the subsequently formed inverse problem will serve as a platform for definition of die/punch geometry (or geometries) required for the calibration of the considered model. Systematic sensitivity analysis, by employing numerical simulation of the experiment will be performed to motivate proper selection of measurable quantities.

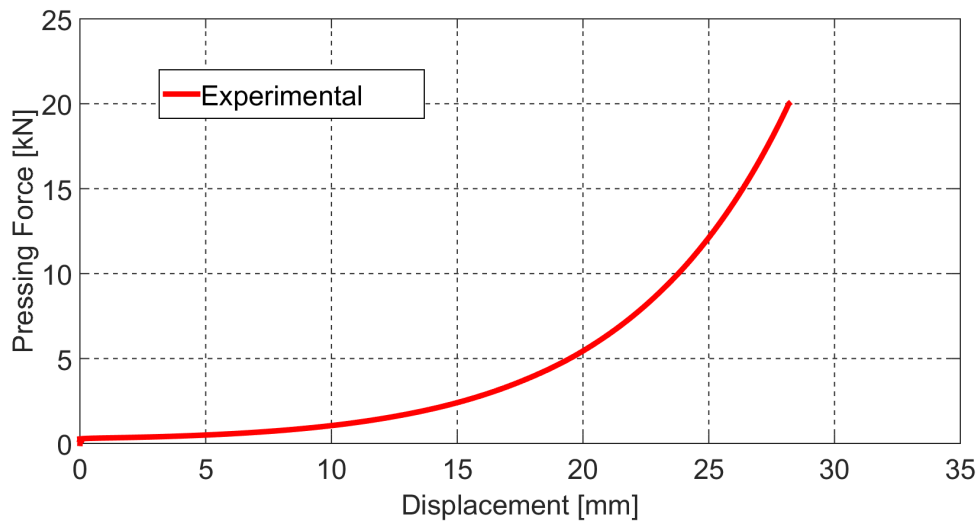


Figure 3.3. Force vs. displacement (of the punch) curve from compaction experiment

3.1.2 General Aspects of Experiment Simulation

The FE models are designed by exploiting axial or planar symmetries wherever possible. The powder is modeled as 2-D deformable body with fully integrated four node axisymmetric element (CAX4) for 2-D cases, or fully integrated tri-linear iso-parametric element (C3D8) in 3-D models. The punches and the mold are considered as analytical rigid surfaces owing to their high stiffness as compared to the powder. The contact is assumed to be hard in the normal direction (i.e. no penetration is allowed) while a coefficient of friction is defined for the lateral direction. All contacts are assumed to operate in finite sliding conditions, according to the implementation in ABAQUS [1].

For the constitutive description, DPC model is chosen as the reference material model. In the numerical implementation of DPC yield function within ABAQUS, seven plastic parameters are required: cohesion (d), friction angle (β), cap eccentricity (R), hydrostatic compression yield stress (p_b), transition surface radius (α), cap position (a) and the flow stress ratio (k). Further on, the elastic parameters, namely: Young's modulus (E) and Poisson's ratio (ν) are also required.

In order to fulfill the need for transformation of the typical DPC model, so as to include elasto-plastic coupling, field dependency of the parameters needs to be incorporated. For such modifications, ABAQUS proves to be a very suitable choice as it offers the possibility to amend the existing model using the user-subroutine "USDFLD". Within the USDFLD

subroutine, the parameters can be defined as a function of some solution dependent field. Here it is selected to be plastic strain, which in turn can be converted to relative density using equation (2.7). To formulate the dependency of governing parameters on relative density, following relationship is proposed:

$$P(\rho) = (P_f - P_0) \left[\frac{\rho - \rho_0}{\rho_f - \rho_0} \right]^n + P_0 \quad (3.3)$$

where, P_f and P_0 are the values of the parameter at final and initial relative density respectively, ρ_f and ρ_0 are final and initial value of density selected *a priori*, hence, not subjected to the identification, while, n is the exponent governing this transition.

With this approach the trend of parameter change over a wide range of relative density is assessed by its initial value, final value and the exponent. Apart from introducing the elasto-plastic coupling (i.e. the dependency of elastic parameters on accumulated plastic strain), such description offers a framework for introducing more complex hardening rule with respect to what is available within typical DPC model implementation.

Within present research it is proposed that four plastic parameters (d, β, R, p_b) along with the elastic ones (E, ν) are going to be identified by using the above formula, while the others (α, a, k) will be kept fixed at a constant value throughout the simulation. This assumption is reasonable since the transition radius which enables smoothening, cap position that is related to the history of the material and the flow stress ratio controlling the shape of yield surface, usually change marginally with progressing compaction. Therefore, a total of 21 inputs are required for the numerical simulation. Coefficient of friction is an additional quantity needed for the simulation. In the current work, it is assumed as an unknown, and therefore subjected to identification along with other parameters, offering a more realistic alternative as compared to previous studies [23, 26] where its value was *a priori* assumed.

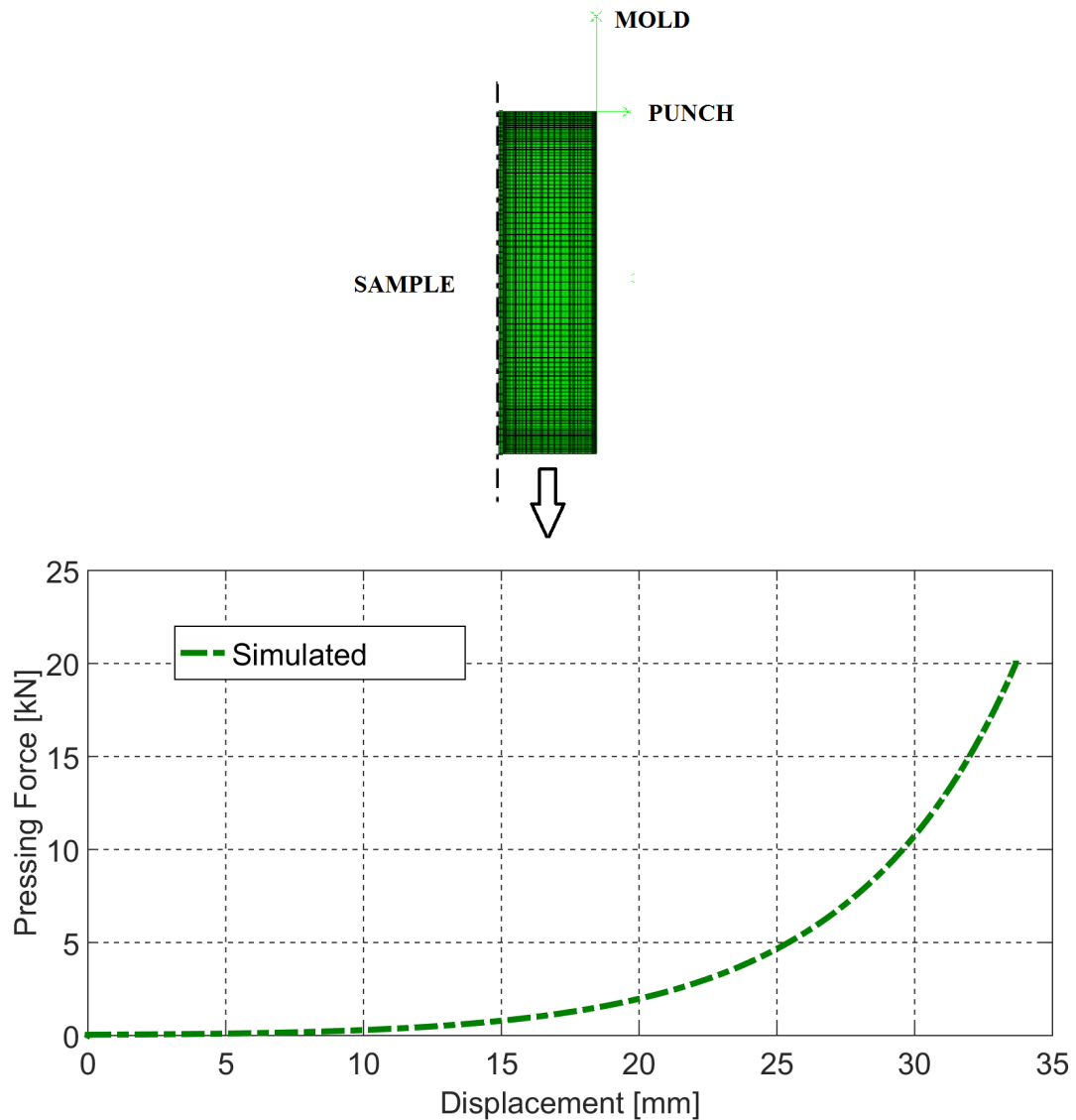


Figure 3.4. FE model of compaction simulation and the digitally extracted curve

Upon performing the test simulation, the force vs. displacement curve is extracted from the simulation and transferred to the digital form visualized in figure 3.4. Simulated curve together with the experimental one serve to form discrepancy function in the form given by equation (3.2), which is subsequently minimized. Main features of the minimization algorithms employed to this purpose are outlined in what follows.

3.2 Mathematical Programming

3.2.1 Forming the Discrepancy Function

The results from the experiment and the simulations are collected to form the residual vector using equation (3.1). In the present context, the entries to the vector \mathbf{R} are the differences between displacements corresponding to a certain level of force (see figure 3.5). The discrepancy function (ω) given in relation (3.2) represents the sum of squares of the residual vector members.

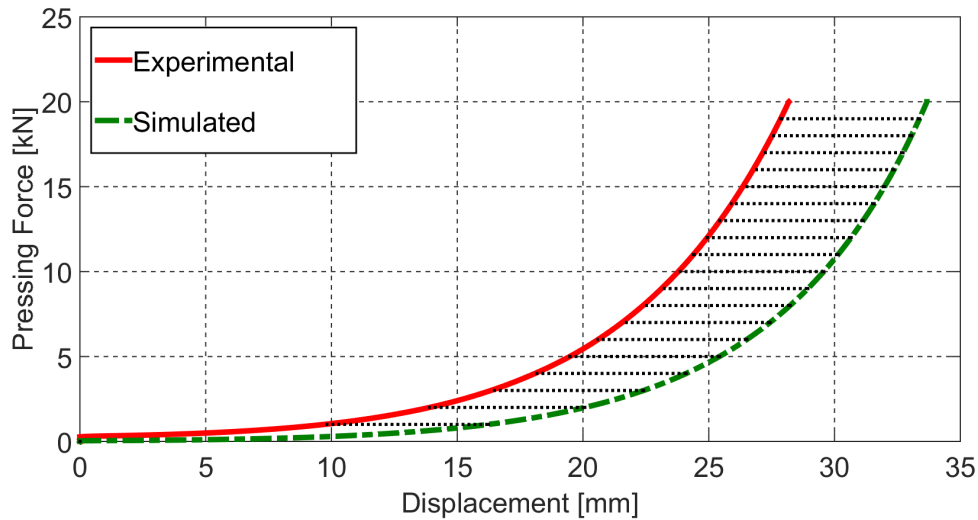


Figure 3.5. Visualization of the residual vector formation as the difference between experimental and simulated curve for compaction.

Such an expression of the discrepancy function (usually referred to as the objective function in the minimization jargon) in the least square sense is the most frequently used formulation in engineering for fitting actual data employing parameterized models [13]. This kind of definition offers certain advantages, particularly when calculating derivatives. Differentiating the objective function with respect to the parameters \mathbf{p} , gives:

$$\frac{\partial \omega}{\partial \mathbf{p}} = 2 \left[\frac{\partial \mathbf{R}}{\partial \mathbf{p}} \right]^T \mathbf{R} \quad (3.4)$$

where, $\left[\frac{\partial \mathbf{R}}{\partial \mathbf{p}}\right] = \mathbf{J}$ is the Jacobian, which is a $m \times n$ matrix. Here, m is the size of residual vector \mathbf{R} and n is the total number of sought parameters. Hessian matrix of second order derivatives of the objective function can be written as:

$$\frac{\partial^2 \omega}{\partial \mathbf{p} \partial \mathbf{p}^T} = \mathbf{J}^T \cdot \mathbf{J} + \sum_{i=1}^m r_i \frac{\partial^2 r_i}{\partial \mathbf{p}^2} \quad (3.5)$$

where, r_i is the component of vector \mathbf{R} . The contribution of the second part in above equation (3.5) vanishes in the vicinity of the solution, since r_i members are close to zero there. Hence, approximating Hessian matrix just by the first term in (3.5) represents a reasonable simplification. This approximation is a very peculiar feature of the least square type of problem formulation adopted in many engineering problems and is going to be used throughout this work. The minimization of this function with respect to the sought parameters is the solution to the inverse problem. Some of the minimization techniques employed to this purpose are outlined in what follows.

3.2.2 Minimization Algorithms

Minimization algorithms usually solve the problem iteratively. After the initial guess is supplied, the procedures iteratively propagates by generating new parameter sets with the improved value of the objective function, even though some algorithms are not providing continuous reduction of it. The scheme employed to proceed from one iteration to another, distinguishes the type of algorithm. There are two fundamental strategies for moving from current solution point to the next one: (1) line search methods and (2) trust region methods.

Line Search Methods

Within the line search minimization technique, it is required to find the direction $\boldsymbol{\alpha}_k$ and to determine how far to go along that direction (d_k). If the current iterate is \mathbf{p}_k , the new one is given by:

$$\mathbf{p}_{k+1} = \mathbf{p}_k + d_k \boldsymbol{\alpha}_k \quad (3.6)$$

The effectiveness of this method relies on the choice of the direction as well as the step length determined by the scalar d_k . The selection of these two quantities distinguishes different types of line search methods, where the two most common ones, are: line search with steepest descent and Newton line search technique. These two are briefly described here.

Steepest Descent Method:

In this method, the direction of steepest descent is found by calculating the gradient and dividing it by its magnitude, as it is the most logical approach, namely:

$$\boldsymbol{\alpha}_k = -\frac{\frac{\partial \omega}{\partial \mathbf{p}_k}}{\left\| \frac{\partial \omega}{\partial \mathbf{p}_k} \right\|} \quad (3.7)$$

Once the direction is determined, the algorithm needs to find the appropriate step length that minimizes the following equation:

$$\min_{d_k} \omega(\mathbf{p}_k + d_k \boldsymbol{\alpha}_k) \quad (3.8)$$

Ideally, the best step length would be the one that globally minimizes the relation (3.8). However, it may be computationally too expensive to find this value. Usually, a few different combinations of the step lengths are tried and then the best of them is selected. Choosing different step lengths means solving the forward problem each time, for that particular length. This needs to be repeated for each iteration. Note that the steepest descent is the direction at the current iterate and may not match the direction of global minimizer. Such a circumstance, which is almost always there in non-convex problems, causes this method to take small steps. Since, the difficulty is related to the direction itself, there are no effective ways to improve the overall performance. Therefore, a high number of iterations would be required to solve the problem, usually with a linear convergence rate. This is a major drawback when using this method, since each iteration is computationally expensive, as the forward solver is a FEM simulation. An alternative line search strategy, that potentially provides quadratic convergence relies on the objective function expressed as a quadratic form. Such approach is adopted within Newton line search method.

Newton Line Search Method:

In this technique, the direction α_k is derived by minimizing (with respect to α_k) the Taylor series approximation of the objective function truncated at the second order. The numerical relation is given by:

$$\omega(\mathbf{p}_k + \alpha_k) \cong M_k(\alpha_k) = \omega(\mathbf{p}_k) + (\alpha_k)^T \left[\frac{\partial \omega}{\partial \mathbf{p}} \right] (\mathbf{p}_k) + \frac{1}{2} (\alpha_k)^T \left[\frac{\partial^2 \omega}{\partial \mathbf{p}^2} \right] (\mathbf{p}_k) \cdot (\alpha_k) \quad (3.9)$$

where, \mathbf{p}_k is the current iterate, α_k is the direction and M_k represents the model function. Assuming Hessian matrix to be positive definite, Newton direction can be evaluated by taking first derivative of the model function with respect to the direction and setting it to zero, which gives:

$$\alpha_k = - \left[\frac{\partial^2 \omega}{\partial \mathbf{p}^2} \right]^{-1} \left[\frac{\partial \omega}{\partial \mathbf{p}} \right] \quad (3.10)$$

It can be observed that the Newton direction has a step length of one (i.e. no additional scaling is required), as it is derived by setting the first derivative of model function to zero. This implies that Newton direction is the exact minimizer of the model function and therefore, it can give the solution in just one iteration if the model function closely represents the real objective one. However, that is not usually true in the cases of non-convex problems, since the model approximation of the objective function starts to worsen far from the current iterate, which could potentially lead to an increase in objective function's value. Another issue is that the Hessian matrix can be non-positive definite. Clearly, in this case the Newton direction cannot be defined. There are methods which modify Hessian matrix to make it positive definite, but it is arguable if such a modification would yield a descending step. This hampers the performance of Newton method in complicated problems, such as the one considered in this research, where the objective function depends on elevated number of parameters. As a possible remedy, the second strategy based on the trust region method can be used.

Trust Region Methods

Trust Region Algorithm (TRA) also relies on the quadratic approximation of the objective function (3.9), but used in a different way. In TRA, a region around the current iterate is defined, within which the model function can be "trusted" to be a good approximation of the real objective function. The minimization is further performed but restricted to only this region around the current iterate. This is implemented by simultaneously seeking both the direction and the step length that makes, hopefully, the best possible improvement of the function, within the radius δ_k of the trust region. This minimization sub-problem is formulated by:

$$\min_{\alpha_k} M_k(\alpha_k) \quad \text{such that} \quad \|\alpha_k\| \leq \delta_k \quad (3.11)$$

The evaluation of this minimizer α_k distinguishes the different trust region methods. In the Cauchy point trust region, α_k is found out by using the steepest descent method within this trusted area. The presence of the model function makes the steepest descent method much more effective as trying different step lengths can be done without any computational cost. However, Cauchy point does not involve Hessian matrix and uses it only to compute the model function in the steepest descent direction. Therefore, the Hessian matrix is not contributing in determining the direction and quadratic convergence cannot be expected.

Another strategy known as the Lavenberg Marquardt technique, employs the Newton method to evaluate the direction α_k and restricts it to the trust region. The positive definite nature of the Hessian matrix is ascertained by adding a small scalar quantity to it, when needed. However, in the cases when the scalar is too large, the approximation of the Hessian matrix itself could be erroneous, thus, limiting the algorithm to linear convergence only, or even step rejection due to bad step evaluation. In the cases when the scalar is too small, the Hessian matrix could be very close to being non-positive definite leading to ill conditioned problem, making this technique difficult to use.

Both these methods have their advantages. Steepest descent on one side always ensures that the direction is that of descent while, Newton method offers quadratic convergence. The combination of the two would help derive maximum benefits, and is most commonly used trust region method. In this technique, minimizer α_k can be

expressed as the linear combination of steepest descent and Newton direction, such that:

$$\boldsymbol{\alpha}_k = \|a_1 \boldsymbol{\alpha}_k^{SD} + a_2 \boldsymbol{\alpha}_k^N\| \leq \delta_k \quad (3.12)$$

Expressing the direction $\boldsymbol{\alpha}_k$ in the above form makes the problem two-dimensional, irrespective of its initial dimension: once that $\boldsymbol{\alpha}_k^{SD}$ and $\boldsymbol{\alpha}_k^N$ are formulated, the goal is to find the values of the coefficients a_1 and a_2 that define the direction $\boldsymbol{\alpha}_k$. These coefficients can be evaluated using the Langrange multipliers technique, details on which can be found in [13].

The effectiveness of TRA highly depends on the trust region size. The usually adopted criterion to select its radius (δ_k) is given by the ratio written below:

$$\frac{\omega(\mathbf{p}_k) - \omega(\mathbf{p}_k + \boldsymbol{\alpha}_k)}{M(0) - M(\boldsymbol{\alpha}_k)} \quad (3.13)$$

Numerator of the above ratio is the actual decrease in the value of the objective function while the denominator is the predicted reduction, which is clearly always a positive number. This ratio, which is calculated *a posteriori* once that next parameter set is evaluated, gives information for potential modification of the trust region radius for the subsequent iteration depending on its value. If the ratio is close to one, it means that the model and the objective function are in good agreement, and one could possibly enlarge the trust region, helping to progress with larger steps and potentially, move much closer to the minimizer of the objective function. If the ratio is negative, it means that the value of the objective function has increased and thus, the step is rejected and trust region is shrank. If the ratio is very close to zero, it implies that the model function is not a good approximation of the real objective function and the trust region radius should still be reduced, to avoid possible step rejection in the subsequent iteration. The presence of this radius constrains the search of the direction in the region where model function is in close approximation of real objective one, thereby, avoiding possible step rejections. This makes TRA more robust for complicated problems, as the one dealt within this research.

Another advantage offered by TRA is the possibility to deal with constraints of the type $\mathbf{l}_b \leq \mathbf{p} \leq \mathbf{u}_b$, where, \mathbf{l}_b and \mathbf{u}_b are the lower and upper bounds respectively, imposed

on the sought parameters. This is particularly important from the point of view of the current problem, since the variables in question are material parameters, which need to have physically acceptable values. In the light of these mentioned benefits, TRA will be used throughout this research as the minimization algorithm.

Within the TRA, the first derivatives are calculated using finite differences, meaning that the number of simulations required is one more than the total count of the sought parameters. The minimization generally involves about ten iterations, with mostly continuous reduction of the objective function (i.e. limited number of step rejections), provided that the problem is well-posed. When the minimum change of the objective function or the parameters between two consecutive iterations reaches a predefined threshold (specified by the tolerances), iterative procedure is stopped. The final converged solution at the end of the iterative procedure is the best estimate of the sought parameters.

The IA methodology outlined in this chapter is applied in the context of powder compaction, offering several advantages. IA procedure gives the possibility to assess the material parameters by using data from the compaction test only, without any further experimentation. The constitutive parameters are defined such that it provides the capability to simulate compaction behavior for a range of materials, by the virtue of the exponent. It can take into account the transitions of parameters ranging from linear ($n = 1$) to exponentially increasing or decreasing. Another big advantage that can be derived is the ability to determine the material properties from a low density up to a high density in a continuous manner, something which is not possible through conventional experiments [26]. Such benefits drive the research towards the use of IA methodology as an alternative to the current methods for calibration of constitutive models. Detailed description of designed testing protocol centered on the discussed techniques, followed by the assessed results is shown in the following chapters.

Chapter 4

PROPOSED CALIBRATION PROTOCOLS

To calibrate Drucker-Prager Cap (DPC) constitutive model, the Inverse Analysis (IA) procedure described in the previous chapter is applied. Material under consideration is a mix of alumina powder with graphite as the binder. Such composition is a commonly used mixture to make refractory materials especially in steel making process [43, 52, 71]. As the first attempt, only a flat cylindrical configuration is going to be used for the calibration purposes and considered measurable quantities are the data collected from digitalized force-displacement curve.

A cylindrical green body of 60 g weight with 36 mm final height and 30 mm diameter (see figure 4.1b) is formed, applying a compaction force of 17675 N corresponding to about 25 MPa pressure. Resulting compaction curve measured from the experiment is shown in figure 4.2.

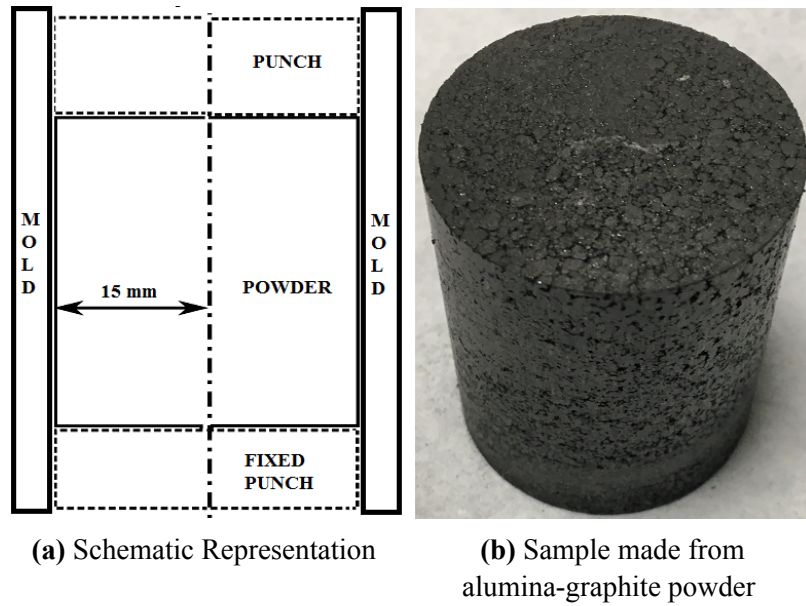


Figure 4.1. Cylindrical green body

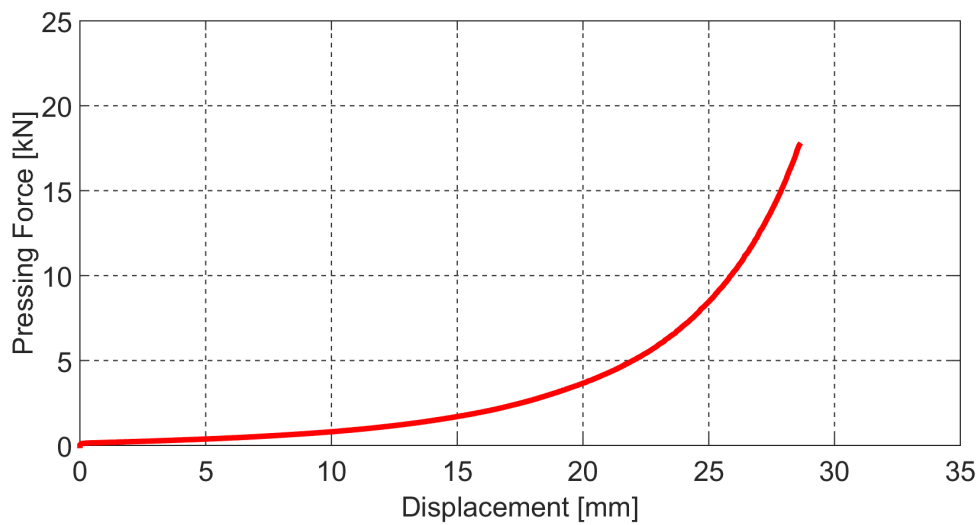


Figure 4.2. Compaction curve corresponding to the cylindrical green body

The simulation is performed within force control regime, corresponding to the experimental conditions listed above. The height up to which the mold was filled is taken as the initial height of the modeled specimen, which is calculated by adding the final green body height (36 mm) to the maximum displacement from the compaction curve (28.6 mm). The powder specimen is discretized in 672 four node fully integrated axisymmetric (CAX4) elements. The other simulation conditions are those described in the previous chapter (see section 3.1.2).

Using the experimental and simulated results IA procedure is developed in order to assess the unknown parameters. The parameters subjected to identification are four plastic parameters namely: material cohesion (d), friction angle (β), cap eccentricity (R) and hydrostatic compression yield stress (p_b); two elastic parameters: Young's modulus (E) and Poisson's ratio (ν); and the coefficient of friction defining the lateral contact between the powder and the mold. Only the friction coefficient is assumed as a constant throughout the compaction and it is evaluated as independent of the relative density, while the other six parameters are estimated as a function of the relative density using equation (3.3) by quantifying the initial and the final value of the parameter (corresponding to initial and final density) along with an exponent governing the transition for this density range. Therefore, a total of 19 parameters are assessed. The parameters are initialized with some "expert" values to start the IA procedure, and the bounds within which these parameters are searched is decided by using the expected range of properties for this type of material. The mathematical programming is done in MATLAB [41], employing the already implemented Trust Region Algorithm (TRA) for minimization. The parameters are normalized between zero and one, where zero corresponds to the parameter's lower bound and one to the upper bound. Gradients are calculated through forward difference with the perturbation of 10^{-4} . The iterative procedure is stopped when the change in the objective function value is less than 10^{-6} or difference between the norm of the parameter vector within two consecutive iterations is lower than 10^{-2} . The comparison of compaction curve corresponding to the final parameters evaluated through IA against the experimental one is given in the following figure.

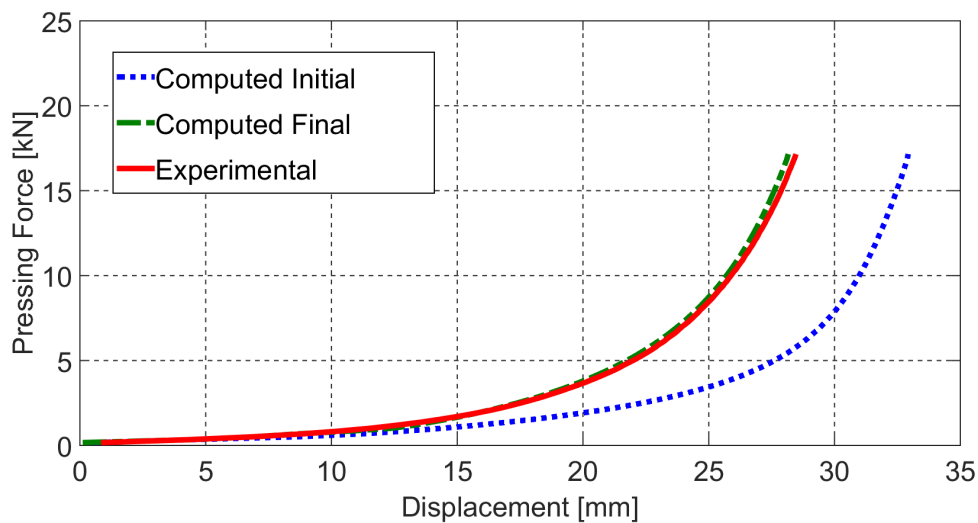


Figure 4.3. Experimental vs. computed curves (initialization 1)

From the above figure it can be seen that the solution to the inverse problem is found. However, since the problem at hand is rather complex and governed by an elevated number of parameters, it is important to check if the found solution represents a global minimizer of the objective function. The most common way to assess this is to use a different parameter initialization and perform an additional inverse analysis. If the procedure converges to the same solution as before, only then other checks (for example, comparison against experimentally determined values) are worthwhile to perform. In the following figure, the compaction curve obtained on the basis of IA procedure starting from a different initialization is visualized.

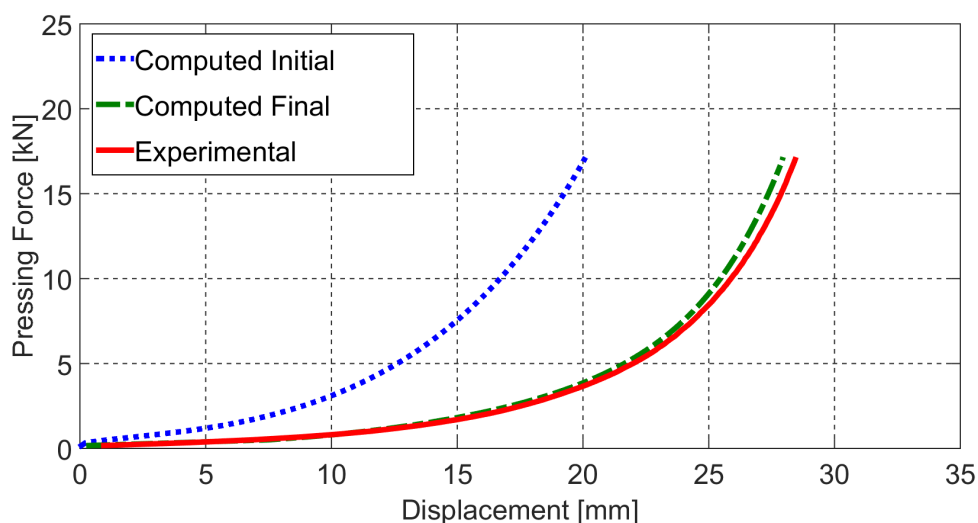


Figure 4.4. Experimental vs. computed curves (initialization 2)

As can be seen, both the above figures give a good agreement between the experimental and simulated curve. This indicates that the minimum was found in both cases. The final parameters at the end of IA procedure are compared in the following table 4.1. The parameters were evaluated for a density range of 0.5-0.9 and their transition can be obtained by equation (3.3) .

Table 4.1. Final parameters corresponding to two different initializations

Parameter	Initial Value		Final Value		Exponent	
	<i>Init-1</i>	<i>Init-2</i>	<i>Init-1</i>	<i>Init-2</i>	<i>Init-1</i>	<i>Init-2</i>
Young's modulus	0.024 [GPa]	0.059 [GPa]	0.766 [GPa]	0.729 [GPa]	4.230	4.733
Poisson's ratio	0.223	0.251	0.238	0.256	1.205	1.068
Material cohesion	0.494 [MPa]	0.435 [MPa]	2.141 [MPa]	3.087 [MPa]	1.929	1.573
Friction angle	54.304 ^[o]	56.279 ^[o]	59.229 ^[o]	58.963 ^[o]	1.315	0.971
Cap eccentricity	0.268	1.064	0.199	0.271	2.931	4.358
Hydrostatic yield stress	0.185 [MPa]	0.149 [MPa]	44.081 [MPa]	25.933 [MPa]	2.853	2.867
Friction Coefficient	0.256			0.248		

Although the compaction curves are nominally the same, it can be realized from table 4.1 that there is a noticeable difference in the values of the parameters. For example, there is a difference of more than 30% in cohesion value between the two sets, while the cap parameters (i.e. R and p_b) have even larger discrepancy. Following figures are further demonstrating the mentioned difference, by comparing these parameters over the whole considered range of relative density.

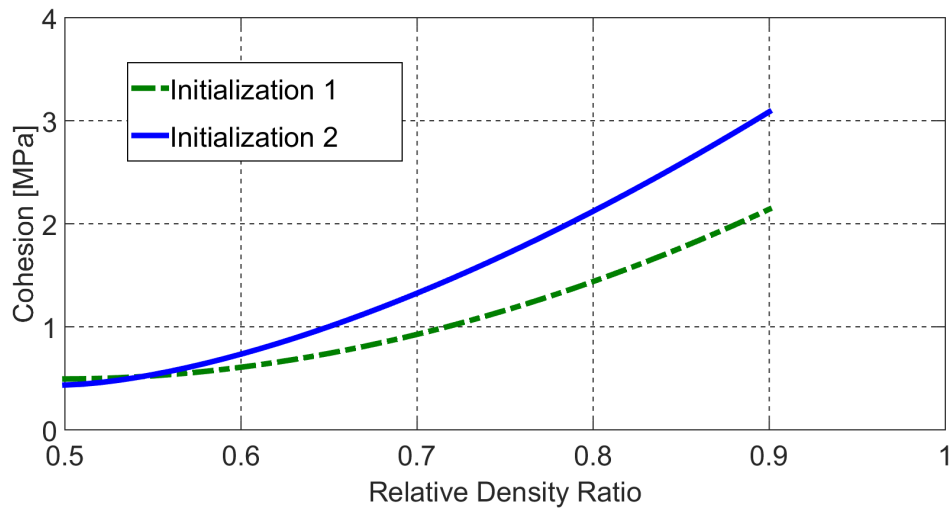


Figure 4.5. Cohesion corresponding to initialization 1 and 2

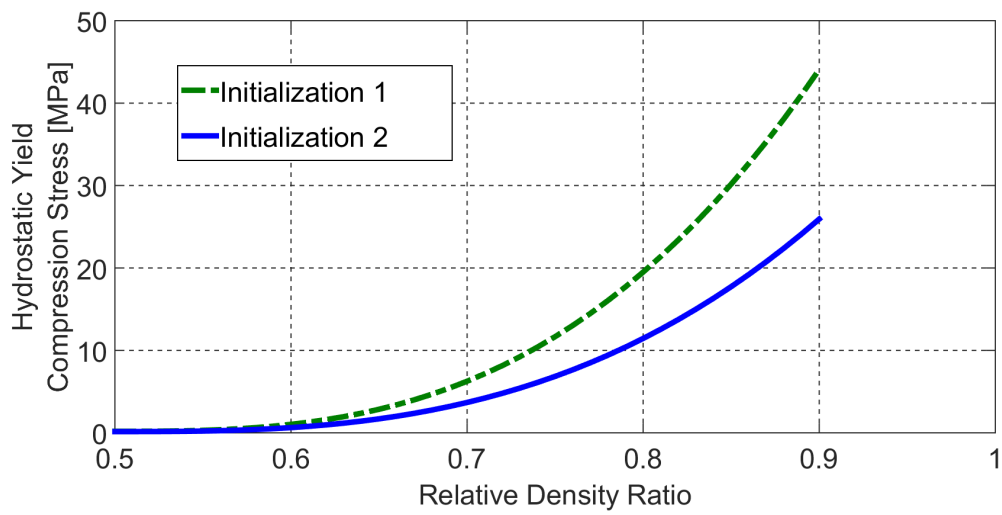


Figure 4.6. Hydrostatic yield compression stress corresponding to initialization 1 and 2

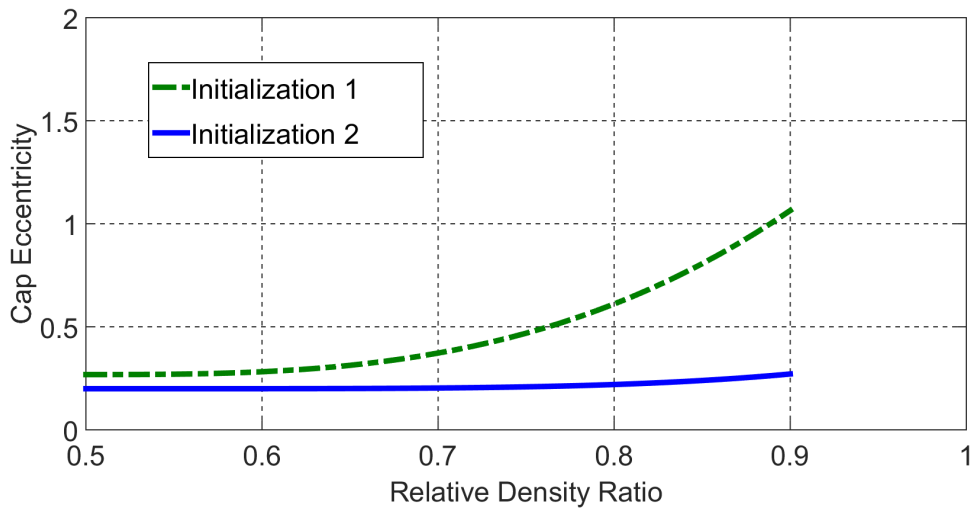


Figure 4.7. Cap eccentricity corresponding to initialization 1 and 2

Previous results clearly illustrate that the inverse problem is "ill-posed" as the objective function is not featured by only one well defined global minimum. Therefore, neither of the parameter sets, which represent the solution of the inverse problem, can be regarded as the representative material parameters. This ill-posedness usually occurs when the measured data from the simulations are not "rich-enough", meaning that the sensitivity with respect to sought parameters is questionable. In the flat cylindrical geometry (configuration-1) considered above, the stress state is fairly homogeneous. The stress distribution over the sample can be visualized in figure 4.8. The simulation leading to the visualized result in the figure is performed without friction, in order to demonstrate the influence of specimen's geometry only to the stress distribution. Note that the model considered here is 3-D for comparison purposes later on.

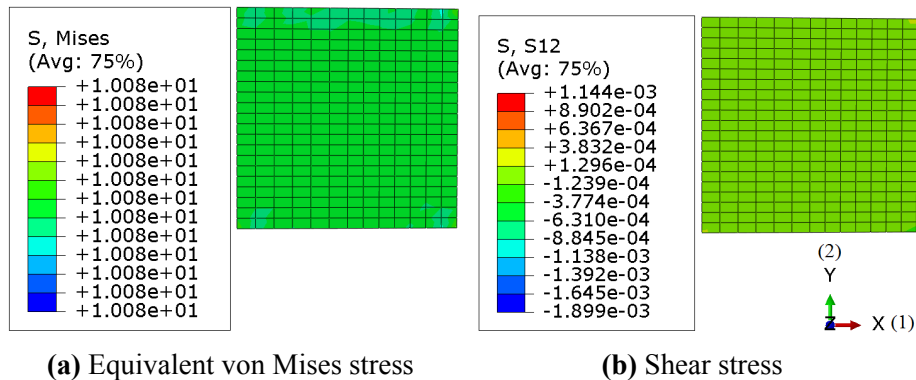


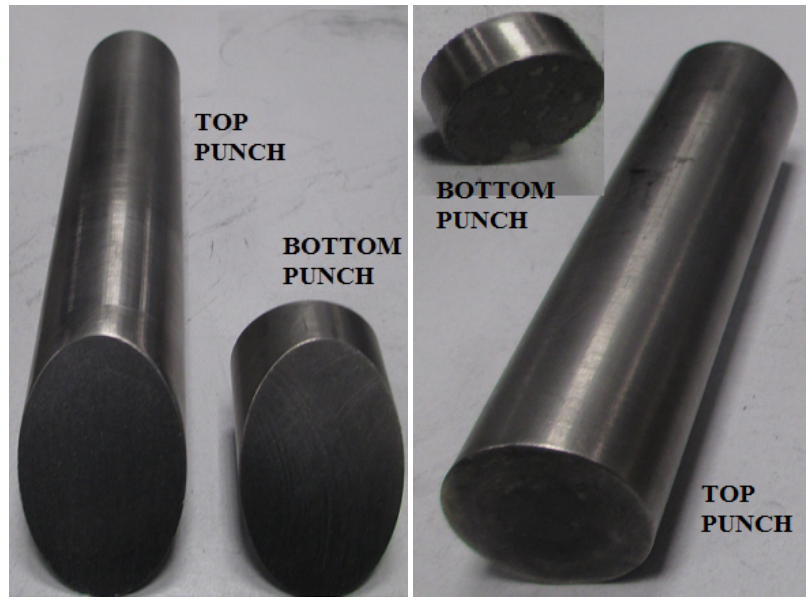
Figure 4.8. Stress distribution in configuration-1

Such stress distribution implies uniform density distribution throughout the sample. Given the complexity of the model with a high number of parameters, it is of vital importance to have a fairly reasonable density distribution over the sample, so that the overall response of the simulation is more sensitive to the sought parameters. Particular difficulty related to the use of curve collected from configuration-1 alone is that the shear component of the stress (figure 4.8b) in the considered geometry is practically equal to zero. This results in the fact that the sensitivity of measurable quantities with respect to cohesion and friction angle, defining the shear failure line, are rather low.

From what precedes, it is clear that more complex geometries need to be considered to have heterogeneous stress distribution within the sample. In particular, the sensitivity of shear failure parameters must be increased by producing specimen which has zones with dominant shear component of the stress. To fulfill these requirements, different geometries will be manufactured in order to address the above mentioned needs. Prior to the selection of these new geometries, first numerical simulations of experiments with different shapes of green body are done. A systematic sensitivity analysis of these designs is carried out to motivate the geometry selection. Some selected results are given in what follows.

4.1 Sensitivity Analysis

The first proposed step for the selection of geometries is to make sure that there is a zone with reasonably large shear component of stress. The most logical way to do so is to use an inclined punch with an angle of 45° , as it represents the surface with maximal value of shear stress. Figure 4.9a shows the proposed punch design. With a view to maximize the heterogeneity in the stress distribution, different geometries are formed combining the flat punch (figure 4.9b) and the newly proposed punch. As opposed to only flat punches used conventionally to form cylindrical green bodies, here, different shapes of the green body are realized by substituting either the top, the bottom or both punches, with the inclined (proposed) geometry. A schematic representation of few such geometries that are considered for the stress distribution evaluation (hereafter, referred as configurations) is given in the figure 4.10.



(a) Proposed punch design

(b) Cylindrical design

Figure 4.9. Proposed punch design along with the conventional cylindrical one

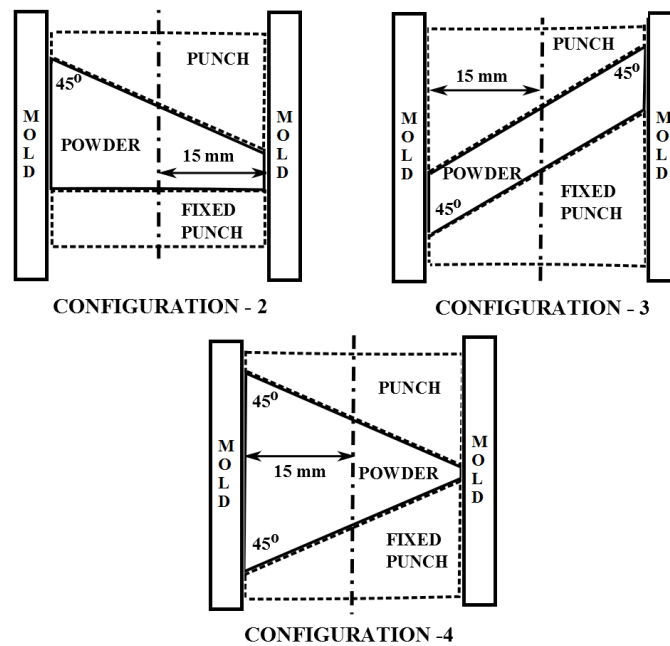


Figure 4.10. Schematic representation of proposed green body configurations

To study the stress distribution, numerical simulations of the above shown configurations are performed within a force control regime. Considered models are three dimensional exploiting planar symmetry. The specimens are discretized into 3200 eight node fully integrated tri-linear iso-parametric elements (marked by C3D8 in ABAQUS). To ensure similar conditions, number of elements are kept the same for all configurations

and a compaction force of 20 kN is considered. In order to have the same starting density (in an averaged sense), the initial height (mean value of longer and shorter heights) is also kept equal for all simulations. Frictionless contact is defined between the powder and mold/punch to emphasize the effect to stress distribution coming only from the different geometry considerations. The study of effects of friction to the stress distribution is given in the following section 4.2. All other simulation conditions are explained in section 3.1.2. The results of stress distribution are given in Figures 4.11 to 4.13.

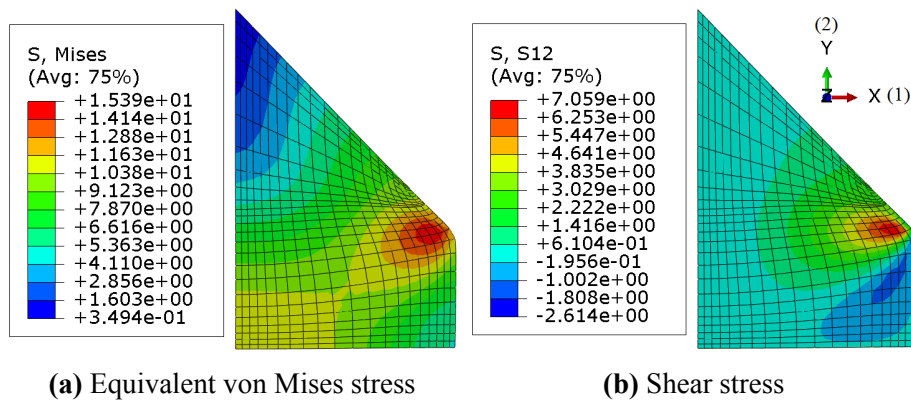


Figure 4.11. Stress distribution in configuration-2

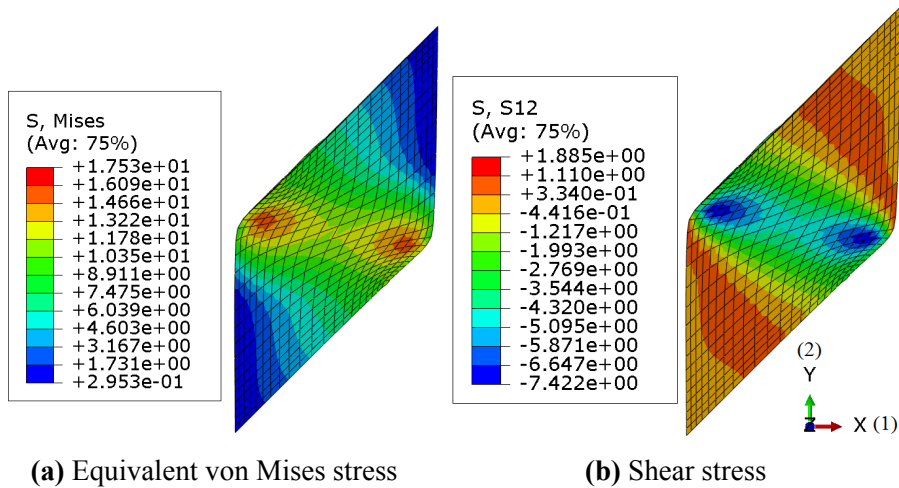


Figure 4.12. Stress distribution in configuration-3

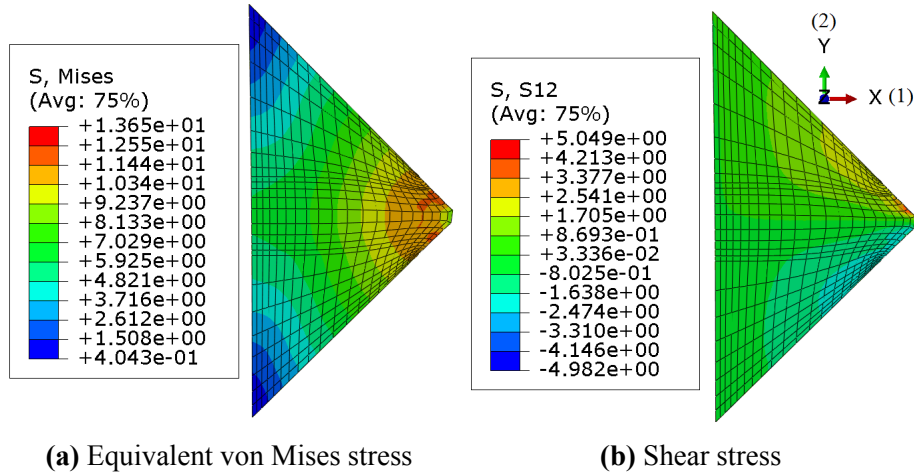


Figure 4.13. Stress distribution in configuration-4

From the above figures, it can be visualized that incorporating such geometries produces a heterogeneous stress distribution within the compacted powder. In particular, the equivalent von Mises stress distribution is most diverse in the configuration-2, while configuration-3 gives the highest value for shear stress. These results justify the choice to use the proposed design, as the source of experimental results to calibrate considered constitutive model. Figures 4.11 to 4.13 show only the final stress distribution over the sample upon the completion of the compaction process. More detailed observations can be made by studying the complete history of a few material points within the sample over the whole compaction experiment.

To perform a quantitative study, stress state of the material points circled in the figure 4.14 is analyzed throughout the compaction and their relative position is kept the same for the comparison purpose. For these material points, stress state over the complete compaction process is presented in a form of hydrostatic pressure (p) vs. equivalent von Mises stress (q) graph, given in Figures 4.15 to 4.18.

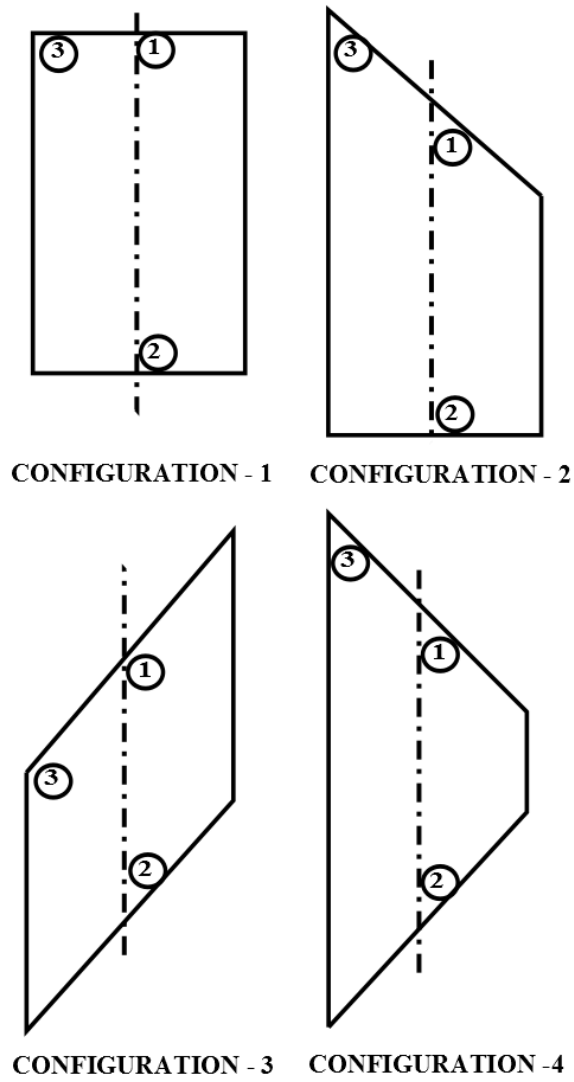


Figure 4.14. 2-D Schematic representation of specimen to show material point locations

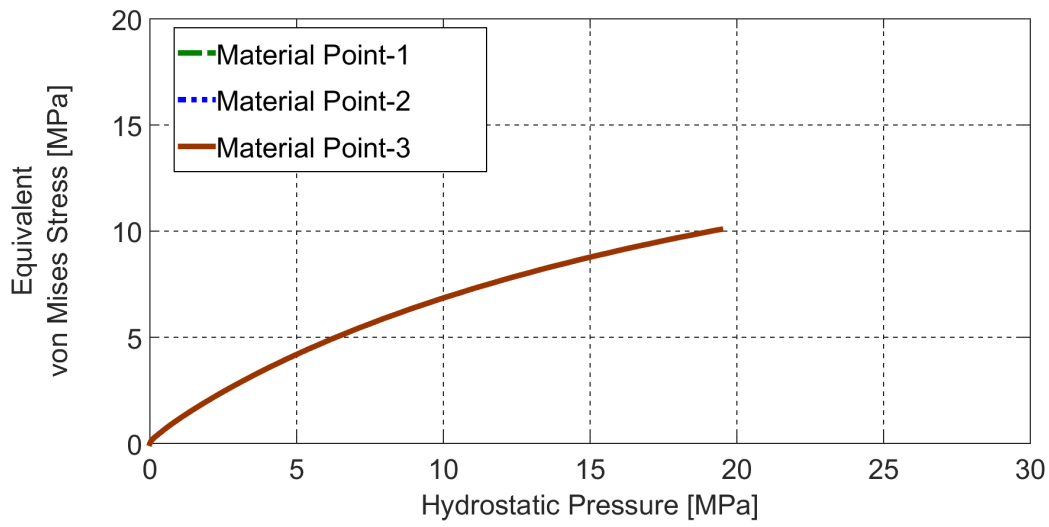


Figure 4.15. Stress path of selected material points in configuration-1

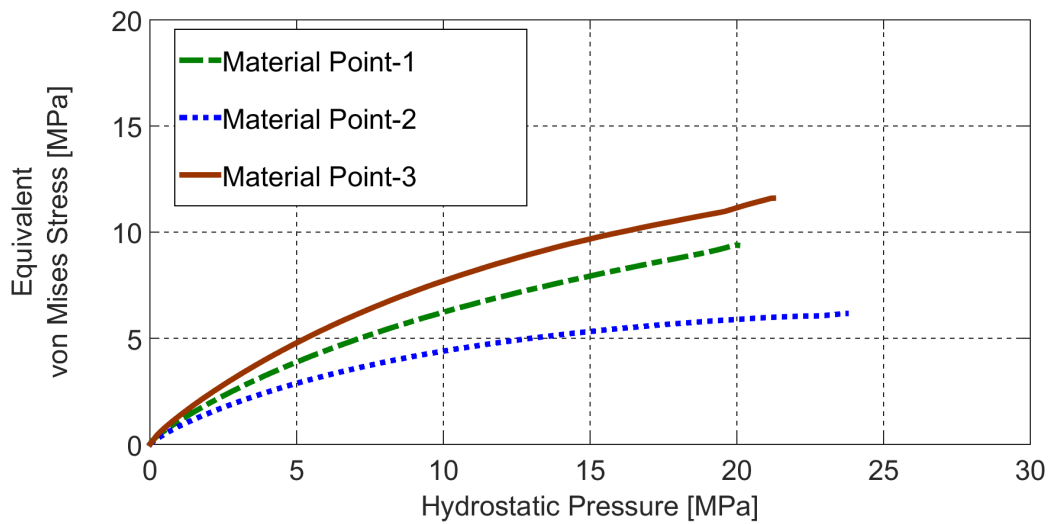


Figure 4.16. Stress path of selected material points in configuration-2

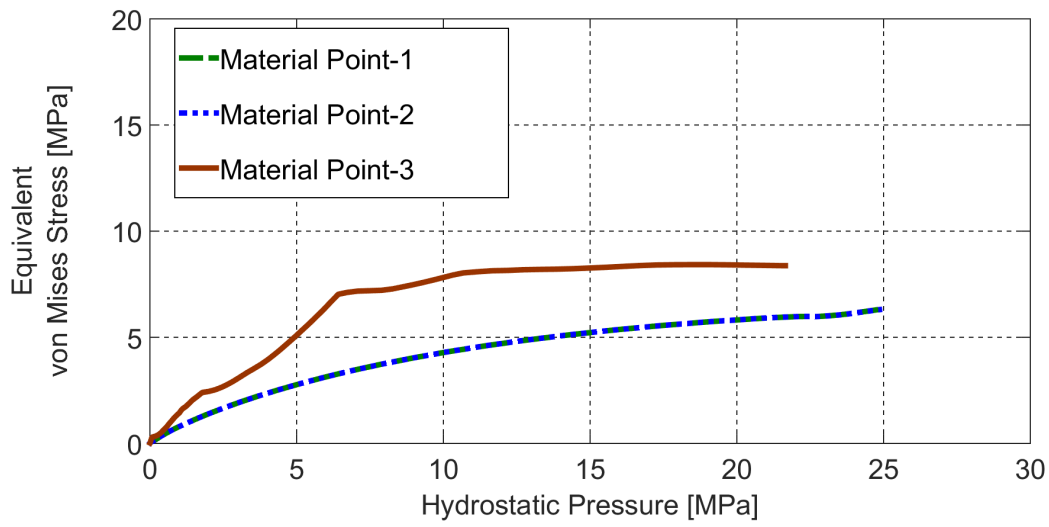


Figure 4.17. Stress path of selected material points in configuration-3

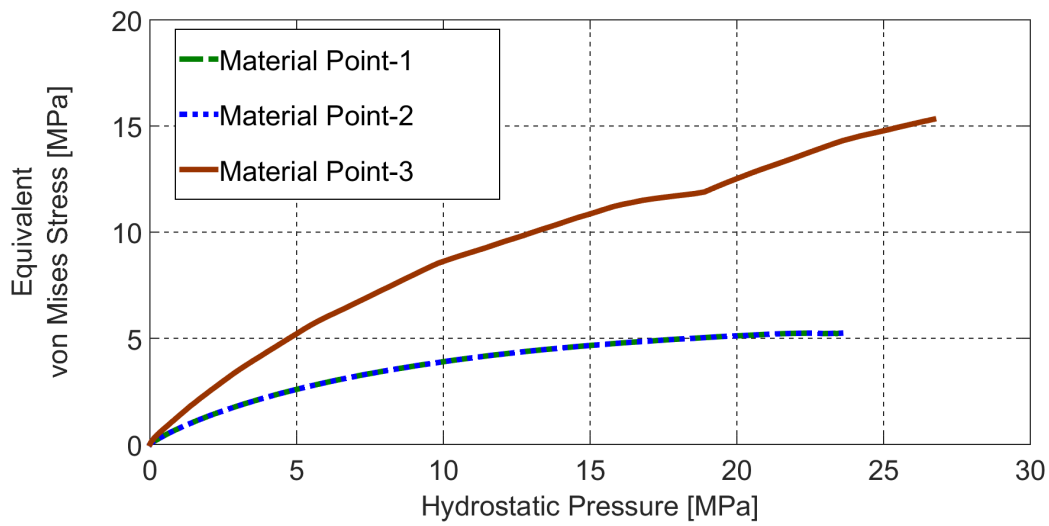


Figure 4.18. Stress path of selected material points in configuration-4

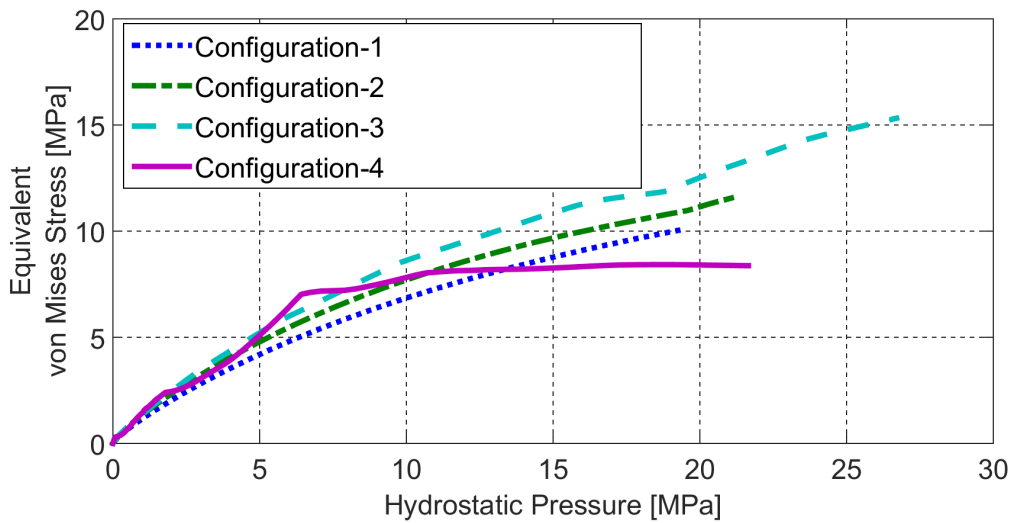


Figure 4.19. Stress path of material point-3 in all configurations

From the above figures, following conclusions can be derived: (a) The plots corresponding to material point 1, 2 and 3 are all distinct in figure 4.16, implying the most diverse stress distribution in configuration-2. (b) In figure 4.19, the stress path of configuration-3 shows comparatively higher values of q for the same p . This suggests that such a loading path of some of the material points (e.g. material point 3 here) in configuration-3 will lie in closer vicinity of shear failure line, making the measurable quantities from configuration-3 the most sensitive to cohesion and friction angle. (c) The plot of material point 3 in figure 4.18 shows a changing stress path within the same element in configuration-4. This further contributes to the heterogeneity in the stress distribution.

Another advantage of employing multiple experiments is that it helps to regularize the inverse problem by providing enriched measurable quantities. Regularization here implies dealing with situations when measurable quantities are sensitive with respect to the parameters but a compensation happens as a result of parameters having opposite effects on the measured data. This leads to circumstances where one parameter (or more) has a lower value, which is compensated by a higher value of the other(s). This would result in multiple combinations of parameters fitting the same experiment, however, none of them would be representative of the material's properties. Such problems were encountered by Bolzon et. al. [8] in an attempt to characterize "mystical" materials through indentation tests. The study used indentation curve (typical output of indentation test) as an input

for IA procedure in order to identify three parameters: Young's modulus, yield limit and exponent of hardening. The latter two compensated for each other's influence as they had opposing effects on the indentation curve. This led to the situation where two (or more) different sets of parameters had exactly the same response.

To tackle this problem, researchers used imprint of the indenter (on the sample) as an additional measurable quantity along with the indentation curve. The imprints were fairly distinct for different sets of parameters that gave similar indentation curve. The parameter set representing the material's properties must also fit the imprint along with the indentation curve, hence, introduction of imprints helped to regularize the inverse problem. In the current work, elevated number of parameters (19) are evaluated presenting a strong probability for such compensation. Therefore, to overcome the possible parameter compensation, employing multiple experiments represents a reasonable strategy.

The results from the numerical simulations of the above mentioned geometries strongly motivate their selection, however, contact friction has not been considered in the performed simulations. Since it is well evidenced in the literature [21, 28] that friction leads to density distribution, it is important to study the effect of contact friction coefficient on the compaction. This study is presented in what follows.

4.2 Effects of Friction

Friction between the powder and punch/mold leads to a heterogeneous stress distribution within the compacted sample, demonstrated in figure 4.20. This heterogeneity in stress caused by friction affects the measurable quantities and it is visualized in the figure 4.21. Since the measurable quantities are sensitive to the friction, it is important to assess the value of coefficient of friction, otherwise the DPC parameters will be estimated erroneously.

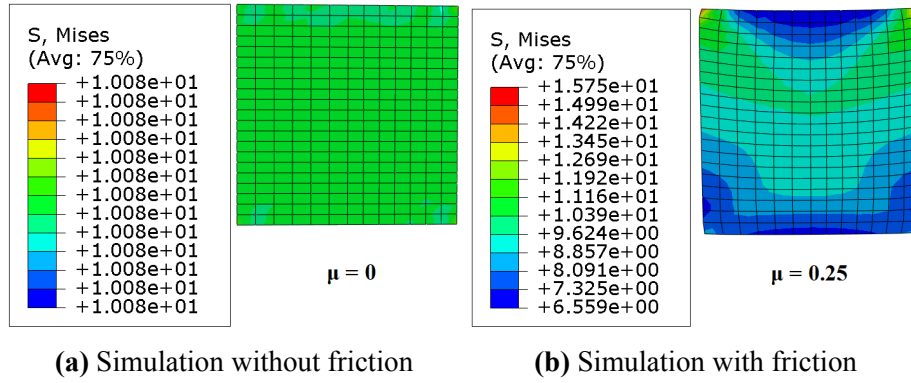


Figure 4.20. Stress distribution highlighting effect of friction in configuration-1

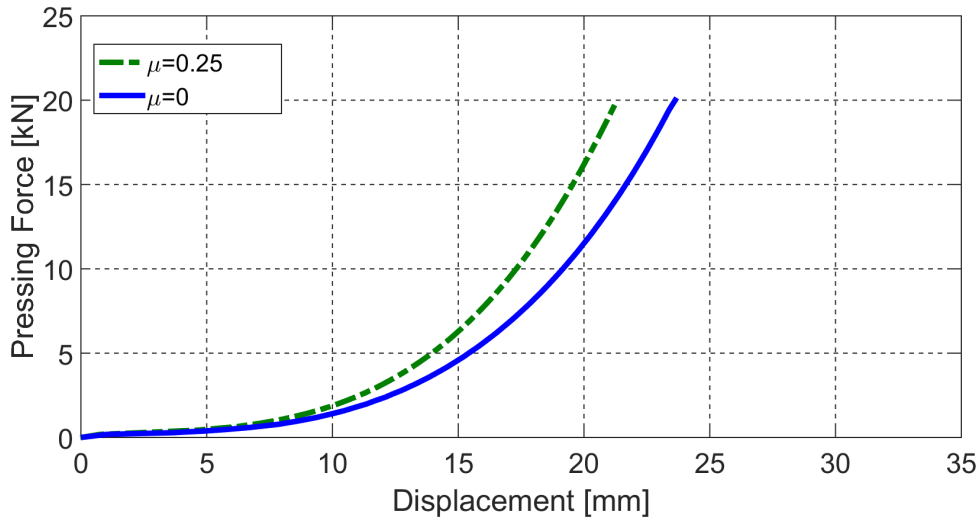


Figure 4.21. Comparison of simulated compaction curves with and without friction

In the works so far, friction coefficient is either fixed as a constant value for the compaction process [26] or it is evaluated using the Janssen-Walker theory [45]. Due to friction, the load transmitted to bottom punch (usually kept fixed during the compaction) is lower than that applied on the top punch. The difference between the loads of the top and the bottom punch can be used to estimate the friction coefficient (μ) utilizing the radial stress measured from the die-wall (mold) based on the Janssen-Walker theory as follows:

$$\mu = \left(\frac{D}{4H} \right) \left(\frac{\sigma_B}{\sigma_r} \right) \left(\frac{\sigma_T}{\sigma_B} \right)^{\frac{z}{H}} \ln \left(\frac{\sigma_T}{\sigma_B} \right) \quad (4.1)$$

where σ_T , σ_B are the stress at the top and bottom punch respectively, σ_r is the radial stress, z is the distance of the strain gage from the top punch, while H and D are the height and diameter of the sample respectively.

In the research of Han et. al. [28] on compaction of pharmaceutical tablets, friction coefficient was identified using the above formula (4.1). Similar approach was used by Zhou et. al. [70] for studying mixed metal powders, Diarra et. al. [23] in their research on cosmetic products, Almanstötter in his work on doped tungsten powder and many others [31, 35, 58] etc. Cunningham et. al. [21] conducted a detailed study on evaluating friction between powder/tooling using the above equation (4.1). The research recommended to perform compaction using single action press for friction estimation as the maximum effects of friction are observed in the compacted specimen, while a double action press was suggested to evaluate the material parameters of the DPC model since it will minimize the frictional effects. Therefore for accurate determination of constitutive parameters along with the friction coefficient, two different compaction experiments are needed in addition to all the destructive tests. Another possible drawback is that such estimation based on the above relation could potentially represent an additional source of error as the quantity of interest (friction) is not directly measured but rather recalculated from the other available measurements.

As a remedy to overcome the above mentioned difficulties, friction coefficient can be evaluated directly through the IA procedure using the measured radial stress from the die-wall. Due to the friction, the transmitted load keeps on decreasing along the height of the specimen when moving farther from the top punch. This drop in load is larger for a higher value of friction coefficient. Such gradient in the force would lead to different values of radial stresses at different locations within the sample. This implies that the radial stress (measurable data) is directly affected by the coefficient of friction (quantity of interest) between the powder and mold. Hence, extracting the stress at multiple locations from the sample and using it as an input for the IA procedure offers the solution to quantify friction.

To the purpose of obtaining radial stress values, strain gages are fitted on the mold. Strain gages 1, 2 and 3 visualized in figure 4.22 are at a distance of 13 mm, 35 mm and 55 mm from the bottom of the mold, while the distance of these gages from the bottom of sample is 3 mm, 25 mm and 45 mm, respectively. For configurations 2-4 the gages are

placed on the longer side of the sample (i.e. left side of samples in figure 4.10). Schematic representation is given in figure 4.23 showing only 2 configurations here for brevity.

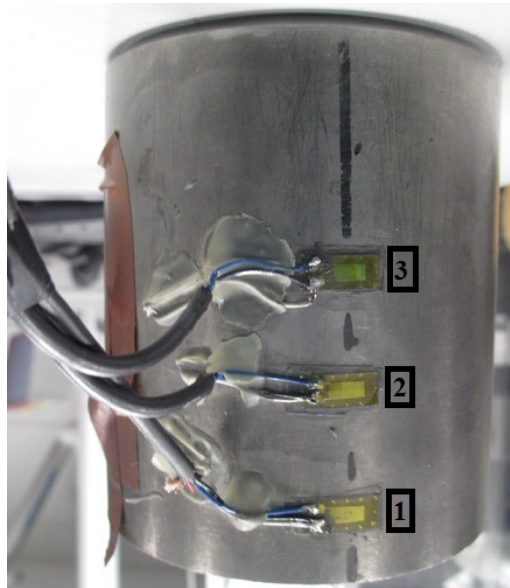


Figure 4.22. Fitted strain gages on the mold

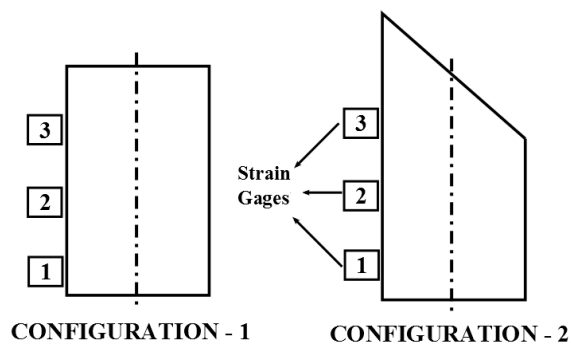


Figure 4.23. Schematic representation of strain gage locations on the sample

The value of the strain recorded from these gages is converted to the stress, with details on this given in appendix A. The stresses are also extracted from the simulations. The experimental and simulated measurements are fed to IA in the form of pressing force vs. radial stress curve visualized in the figure 4.24, corresponding to stress measurement from one strain gage

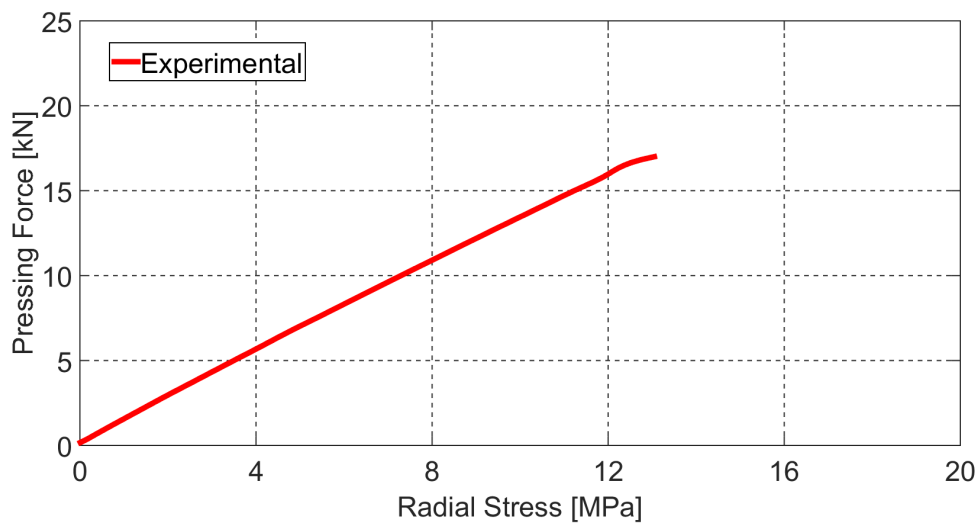


Figure 4.24. Force vs. radial stress from compaction experiment

Inverse analysis relies on the collected data from the experiment and simulation, therefore, the quantification of friction is independent of the type of compaction experiment (single or double action press). Further on, since the parameters are directly evaluated from the measured data within IA, any possible errors coming from recalculation, such as those in equation (4.1), can be avoided.

From the investigations summarized in this chapter, it can be realized that employing proposed geometries is essential for successful implementation of IA in the present context. However, it is important to determine how many of these different experiments (configurations) are needed. To this purpose, compaction curve and radial stress curve from different combinations of these mentioned geometries are going to be used as inputs for IA procedure. On the basis of these results, minimum number of such experiments required for successful calibration are going to be established. The results of the parameter identification employing various combinations of configurations are presented in the next chapter.

Chapter 5

RESULTS

Described test procedures are employed as resources of experimental results to be used for the assessment of constitutive parameters entering Drucker-Prager Cap (DPC) yield criterion through developed methodology based on Inverse Analysis (IA). Comparative IA employing different combinations of configurations should serve to draw a conclusion about minimum amount of data required for identifying representative material parameters. For comparison the same parameters are evaluated by relying on the currently adopted methods following the guidelines laid out in Chapter 2. The test conditions and details regarding material used are given in what follows.

5.1 Materials and Experiments

In the current research, alumina graphite powder mixture is studied. Alumina has high thermal, wear and corrosion resistance, and can operate in the temperature range of 1500 °C - 2000 °C. On the other hand, graphite acts as a binder and has low thermal expansion coefficient ($1.2 \times 10^{-6} \text{ }^\circ\text{C}^{-1}$ - $8.2 \times 10^{-6} \text{ }^\circ\text{C}^{-1}$) [47], high thermal conductivity ($25 \text{ W m}^{-1} \text{ K}^{-1}$ - $470 \text{ W m}^{-1} \text{ K}^{-1}$) [47] and a low wettability by the slag. Combination of the two powders provides excellent thermo-mechanical properties, thus, making the mixture a popular choice for refractory linings of ladles in steel making processes, shrouds for transferring molten steel from tundish to continuous casters, etc. [43, 52, 71].

For the current study, the powder mixture is manufactured by the partner on this project, *Vesuvius Inc.* (Mons, Belgium). The absolute density of the mixture is

determined through pycnometry and found to be equal to 2.638 g/cm^3 . Figure 5.1 shows the Scanning Electron Microscope (SEM) micro-graph [32] of the powder. Long, plate like, particles are graphite, while the irregularly shaped ones are the alumina particles, present in different sizes. This mixture is a topic of research at *Vesuvius Inc.*, a partner in this research, and due to the industrial constraints on sharing information, further details about the composition of powder cannot be provided. The compaction behavior of mentioned powder mixture is characterized in the current work and detailed description of the performed compaction experiments is presented in what follows.

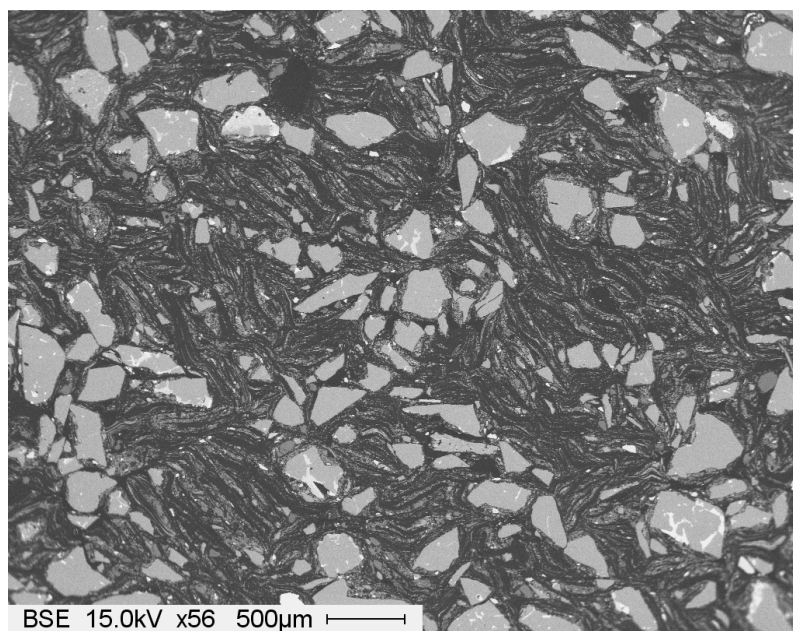


Figure 5.1. SEM micro-graph of alumina graphite powder

5.1.1 Compaction Tests

The compaction tests are performed in a closed die setup. Therefore, it is not possible to measure the displacement of the sample directly, rather the displacement of the punch is recorded. The punch displacement includes the deformation of the specimen and elastic compliance of various elements of the testing apparatus, namely the load cells and punches. This inevitably introduces errors in the measured compaction curve. To quantify the compliance of the experimental apparatus the top and the bottom punches are pressed together with no powder in the die. Load is applied on the top punch, and force displacement response is measured, which has a form as presented in the figure

5.2. This curve is subtracted from the compaction curve of the pressed powder, to give corrected response. All the compaction curves shown in this thesis have been adjusted for this error due to machine compliance.

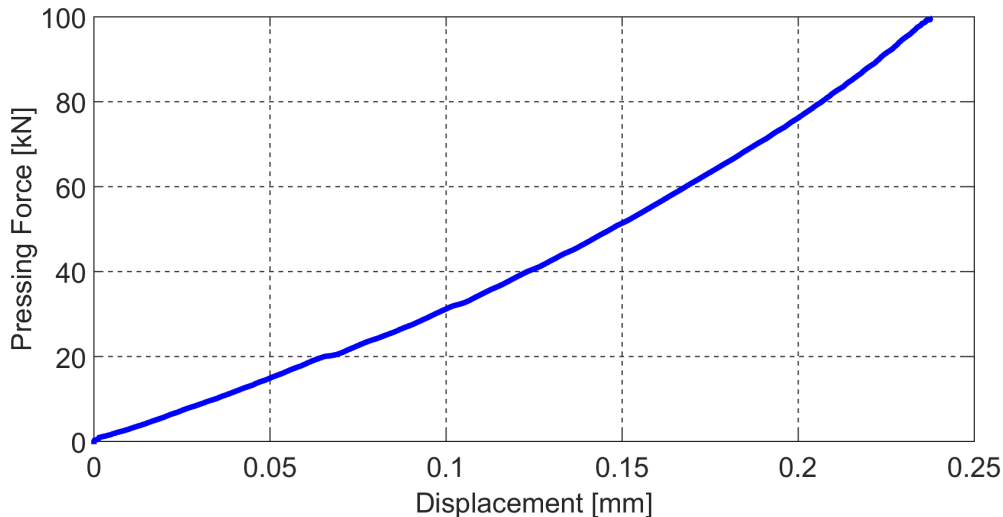


Figure 5.2. Elastic deformation of the testing system

To protect the tooling (mold and punches) against the potential corrosion and wear, nitriding treatment is performed on it. Nitriding is case hardening treatment making the outer metal surface harder while keeping the inner surface intact. Prior to being used within the compaction experiment, the tooling is lubricated by the ceramic lacquer manufactured by *Sogelub* special lubricants. The mold employed for the compaction made from steel subjected to nitriding is 150 mm high with a cylindrical opening of 30 mm in diameter. The load is applied on the top punch moving at a speed of 1.5 mm/min throughout the pressing, while the bottom punch is kept fixed. For the purpose of applying force, an "Instron" testing machine is used and details on this can be found in section 3.1.1. Using this setup, flat cylindrical green bodies of different densities are formed for the destructive tests (crush and Brazilian), while for the calibration through inverse analysis, also additional green bodies of newly proposed shapes are produced, with relevant details outlined in section 4.1. Clearly, for these green bodies different punches are used, but the mold is the same.

Sample Preparation for Crush Tests

For the crush test, samples are produced in a relative density range of 69%-93%. The diameter of the samples is 30 mm while the height ranged from 50-53 mm, giving the height to diameter ratio of 1.75 approximately. The compaction force and the weight of powder is adjusted for preparing required samples. Two green bodies are formed corresponding to the same level of relative density to control the reproducibility of the results. Experimental details are given in table 5.1. Prepared samples for crush tests are visualized in figure 5.3. Compaction curve corresponding to sample of 93% relative density is given in figure 5.4, while others are omitted for brevity.

Table 5.1. Experimental details of the compaction tests performed to prepare crush test samples

Sample Name	Sample Mass [g]	Compaction Force [kN]	Sample Height Final [mm]	Relative Density	Relative Density Averaged
93-1	90	24.84	51.88	0.9303	0.9279
93-2			52.15	0.9255	
89-1	87	13.85	52.46	0.8893	0.8903
89-2			52.35	0.8912	
83-1	80	7.86	51.49	0.8332	0.8314
83-2			51.71	0.8296	
81-1	78	6.86	51.48	0.8125	0.8105
81-2			51.73	0.8086	
78-1	77	5.36	53.02	0.7791	0.7806
78-2			52.80	0.7820	
73-1	70	2.36	51.05	0.7353	0.7319
73-2			51.52	0.7286	
69-1	65	1.16	50.54	0.6897	0.6903
69-2			50.45	0.6909	



Figure 5.3. Prepared samples for crush tests

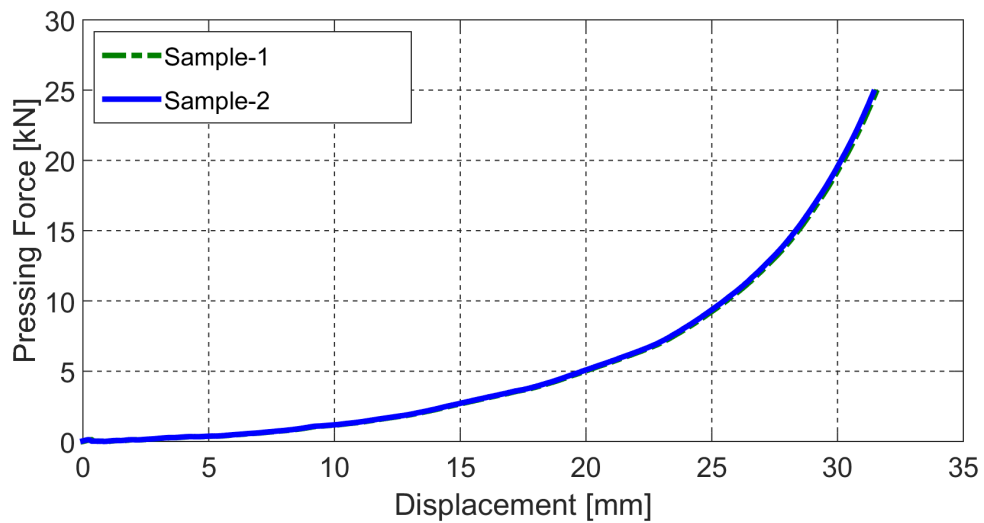


Figure 5.4. Compaction curves of the crush test samples of 93% relative density

Sample Preparation for Brazilian Tests

The Brazilian test is performed in accordance with the ASTM standard D3967-95a [4] which specifies that the height to diameter ratio of the sample must be between $0.2 \div 0.75$. Following the ASTM guidelines, the green bodies are formed with a diameter of 30 mm, while the height varied from 18-21 mm (for different relative densities), corresponding to the aspect ratio of $0.6 \div 0.7$. It is worth noting that here it is crucial to produce green bodies that have the same relative densities as those of the samples prepared for the crush test. This is to ensure that the failure stresses from both the destructive tests (i.e. crush and Brazilian test) are obtained at the same relative density and therefore, cohesion and friction angle, defining the shear failure line, at that particular level of relative density can be determined. To achieve the desired height and the aspect ratio mandated by ASTM standard, the weight of the powder along with the compaction force need to be adjusted accordingly. Relevant experimental details regarding diverse experiments are given in table 5.2. The formed samples are shown in figure 5.5. Compaction curve of the specimen of 93% relative density is given in figure 5.6, while the rest are skipped for brevity.

Table 5.2. Experimental details of the compaction tests performed to prepare Brazilian test samples

Sample Name	Sample Mass [g]	Compaction Force [kN]	Sample Height Final [mm]	Relative Density	Relative Density Averaged
93-1	36	24.92	20.73	0.9313	0.9302
93-2			20.67	0.9340	
89-1	33	13.87	19.94	0.8875	0.8895
89-2			19.88	0.8902	
83-1	30	7.86	19.45	0.827	0.8300
83-2			19.38	0.8301	
81-1	28	7.46	18.52	0.8107	0.8098
81-2			18.6	0.8073	
78-1	27	5.62	18.56	0.7801	0.7809
78-2			18.51	0.7822	
73-1	25	2.56	18.27	0.7338	0.7320
73-2			18.36	0.7302	
69-1	23	1.46	17.85	0.6910	0.6898
69-2			17.93	0.6879	



Figure 5.5. Prepared samples for Brazilian tests

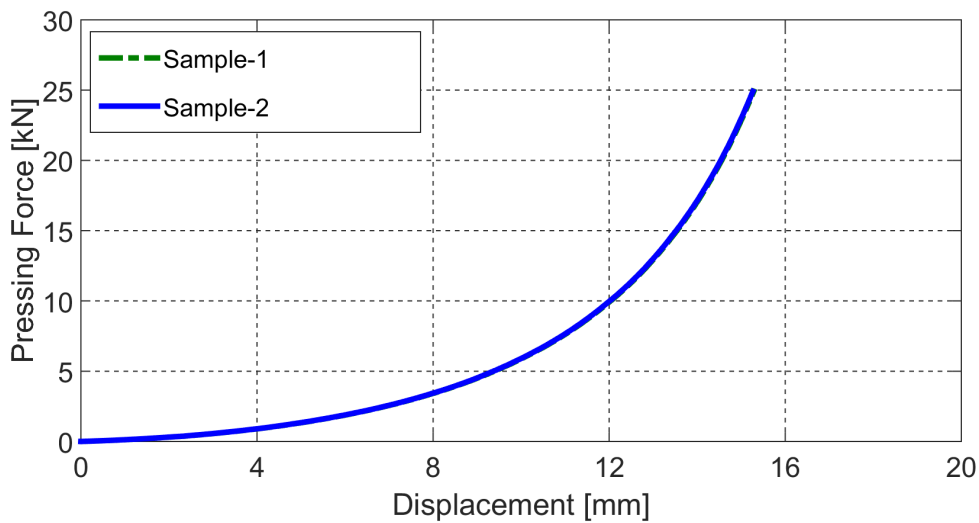


Figure 5.6. Compaction curves of the Brazilian test samples of 93% relative density

For each of the seven relative density values, namely, 69%, 73%, 78%, 81%, 83%, 89% and 93%, two samples are formed for both of the tests (i.e. crush and Brazilian test). Upon performing these tests, cohesion and friction angle are estimated at a particular relative density level. Experimental description and results of the destructive tests are given in section 5.1.2.

Sample Preparation of the Proposed Geometries for Calibration through IA

For calibration through IA, green bodies of various shapes (figure 4.10) along with the flat cylindrical one (figure 4.1a) are formed. For all configurations, pressing force of 17 kN is applied to compact 60 g of the powder in already described mold with cylindrical opening of 30 mm in diameter. Along with the measured force displacement curves, also radial stresses are acquired from the die-wall using the calibrated strain gages with details

given in appendix A. The locations of the strain gages on the mold are visualized figure 4.22.

Relevant experimental details are given in table 5.3. Figure 5.7 shows the formed samples. Resulting compaction and radial stress curves are visualized in figures 5.8 to 5.10. Note that a high compaction force is used so as to form green bodies with a high relative density and therefore, the radial stress from the top gage (gage-3) is not considered. With progressing compaction, the sample gradually leaves the zone where the top strain gage is positioned, and hence the radial stress measurement is not available throughout the whole compaction experiment.

Table 5.3. Experimental details of the compaction tests performed to prepare samples for calibration through IA

Configuration	Initial Height [mm]		Final Height[mm]		Average Relative Density
	Longer	Shorter	Longer	Shorter	
1	64.60	64.60	36.18	36.18	0.888
2	79.12	49.13	51.87	21.89	0.873
3	63.84	63.81	37.79	37.75	0.843
4	87.78	27.80	64.39	4.41	0.865

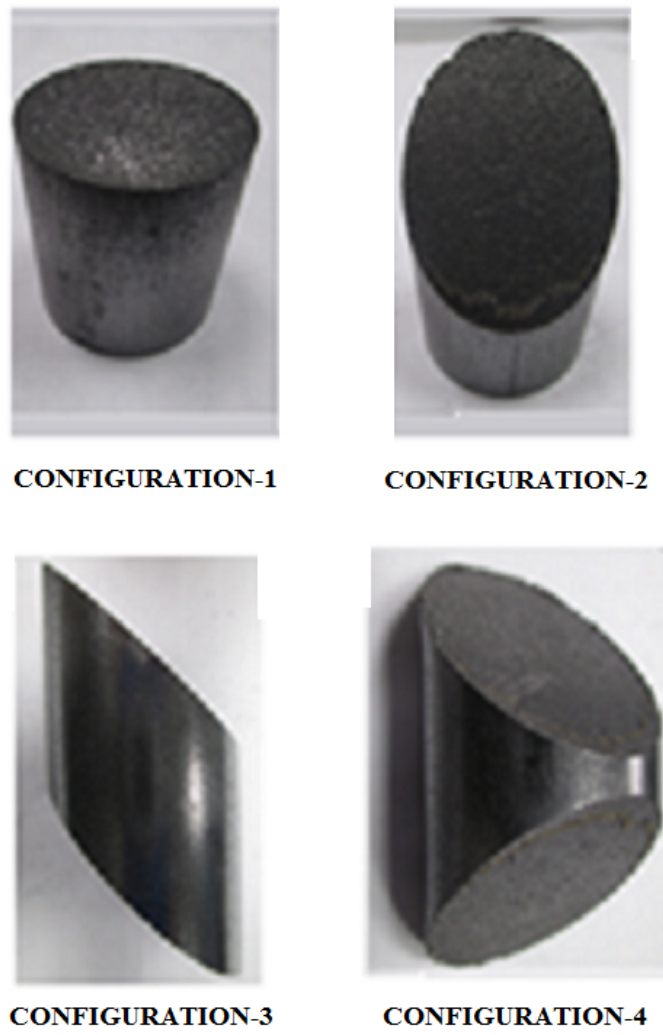


Figure 5.7. Prepared samples for calibration through IA

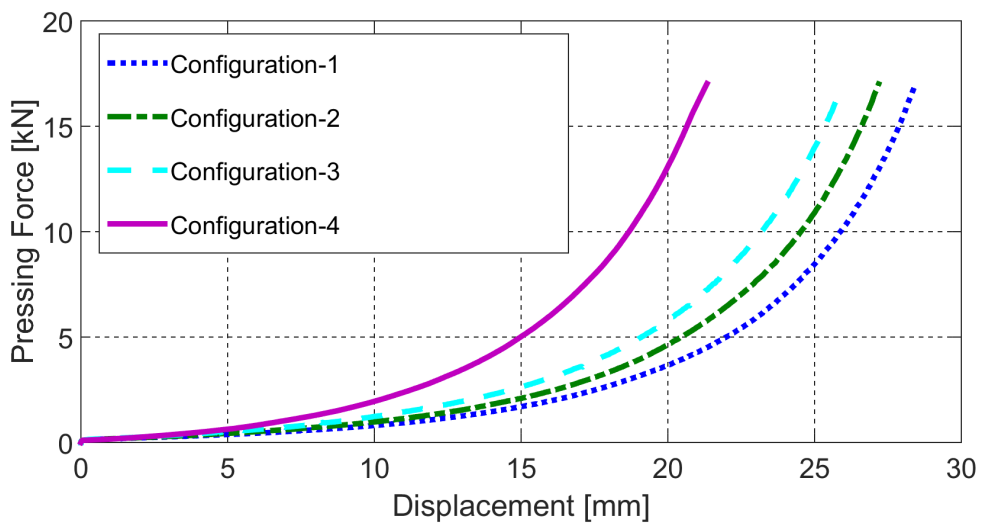


Figure 5.8. Compaction curve corresponding to configuration-1 to configuration-4

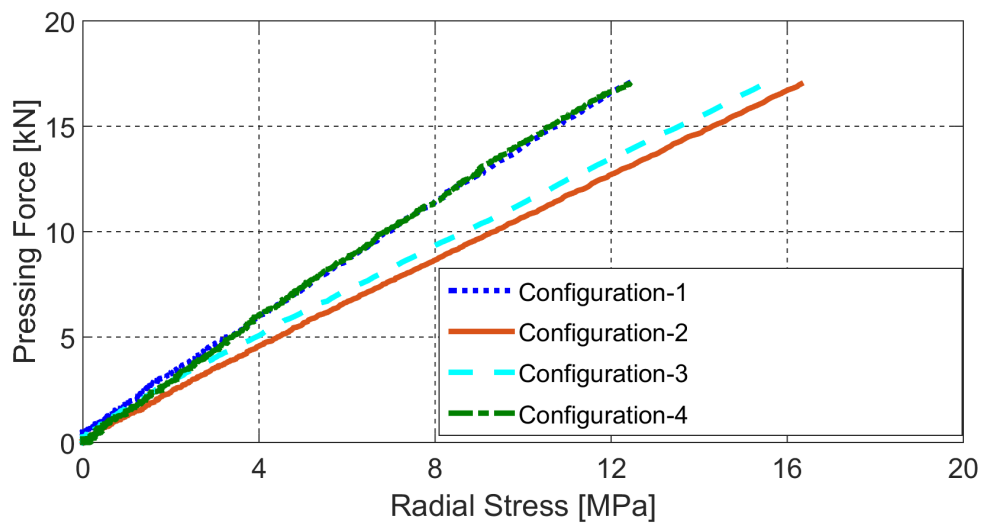


Figure 5.9. Radial stress curves corresponding to configuration-1 to configuration-4 for middle strain gage

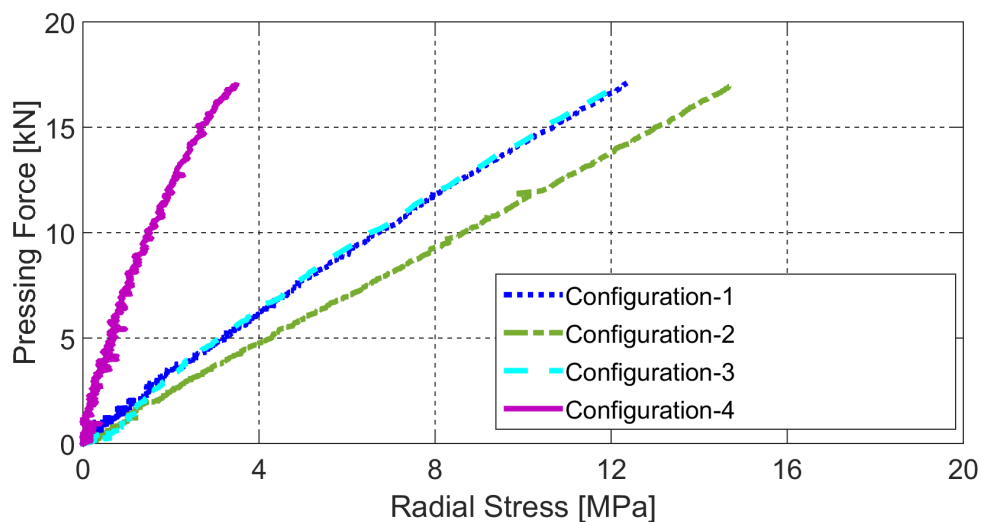


Figure 5.10. Radial stress curves corresponding to configuration-1 to configuration-4 for bottom strain gage

Resulting compaction curves and the radial stress curves corresponding to configuration-1 to -4 are further used as inputs for the IA procedure and the results are given in section 5.3. The radial stress curves shown here will also be utilized to obtain cap surface parameters based on methods of calibration applied as current praxis, with detailed description of the procedure provided in section 5.2. In what follows, Brazilian tests and crush test results of the compacted samples are reported.

5.1.2 Crush and Brazilian Tests

The samples shown in figures 5.3 and 5.5 are subjected to crush and Brazilian tests respectively. These destructive tests are performed on a Tinius Olsen H50KT type press within this research. The force is applied on the top punch which is moving at a speed of 0.3 mm/min, while the bottom punch is kept fixed. A load cell of 10 kN is used, which has an uncertainty of less than 0.05% in force measurement. The machine is shown in figure 5.11. Experimental setup corresponding to crush and Brazilian tests are visualized in figure 5.12 and 5.13 respectively.

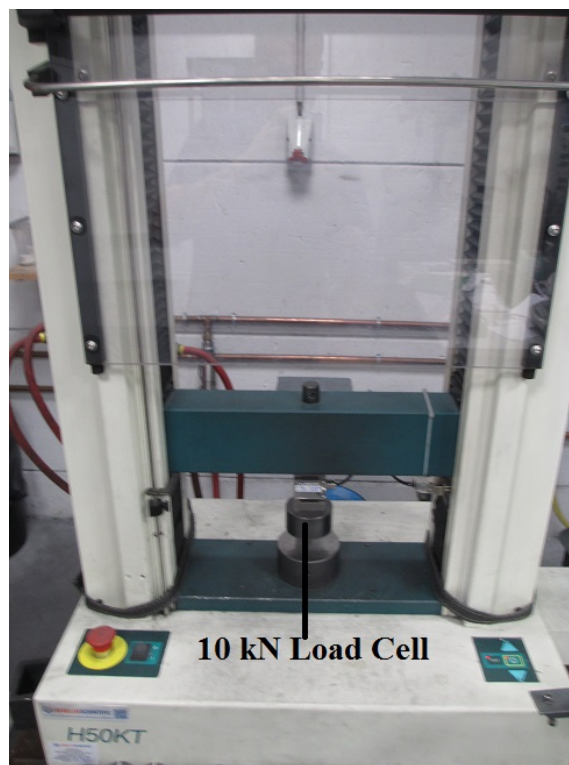


Figure 5.11. Tinius Olsen H50KT press for performing destructive tests

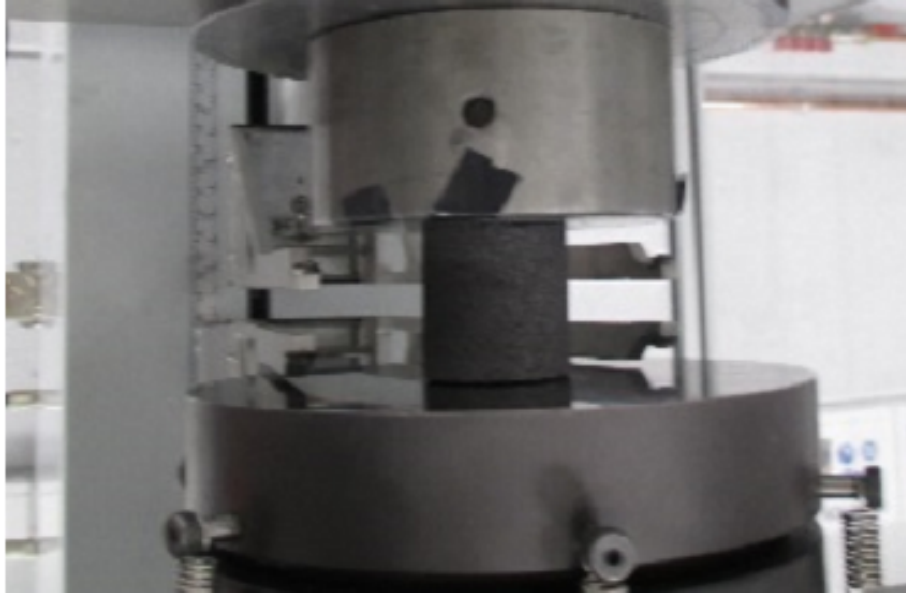


Figure 5.12. Experimental setup of crush test



Figure 5.13. Experimental setup of Brazilian test

Typical output of both these experiments is a force vs. displacement curve, where the maximum force is a quantity required for further calculations. It is used to compute the failure stress corresponding to the two tests using equations (2.10) and (2.11). For more details on these calculations, refer to section 2.2.1. Specimens subjected to the crush and

Brazilian tests are shown in 5.14 and 5.15, respectively. The force vs. displacement curves measured from the crush tests performed on the samples of relative densities 93% and 78% are given in figures 5.16 and 5.17, respectively, as the most representative ones. Similarly, figures 5.18 and 5.19 show the Brazilian test results for the green bodies of 93% and 73% relative density. The other force-displacement graphs of crush and Brazilian tests have been omitted for brevity.

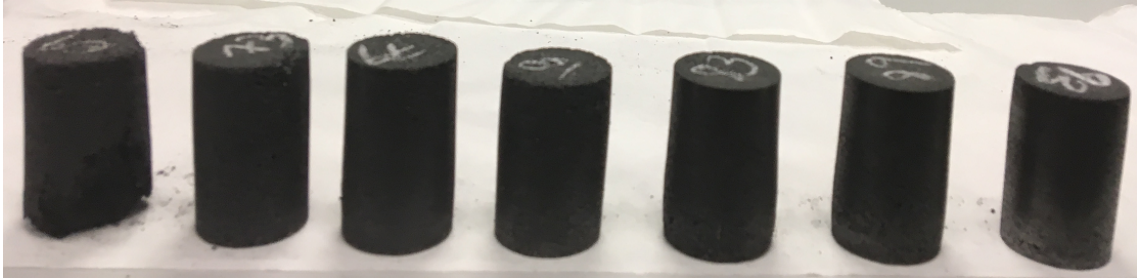


Figure 5.14. Samples corresponding to 69% to 93% relative density (left to right) subjected to crush test

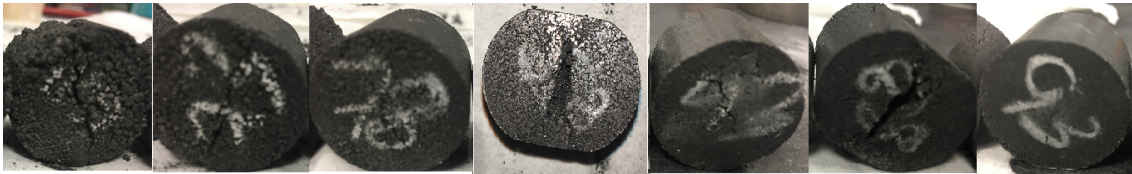


Figure 5.15. Samples corresponding to 69% to 93% relative density (left to right) subjected to Brazilian test

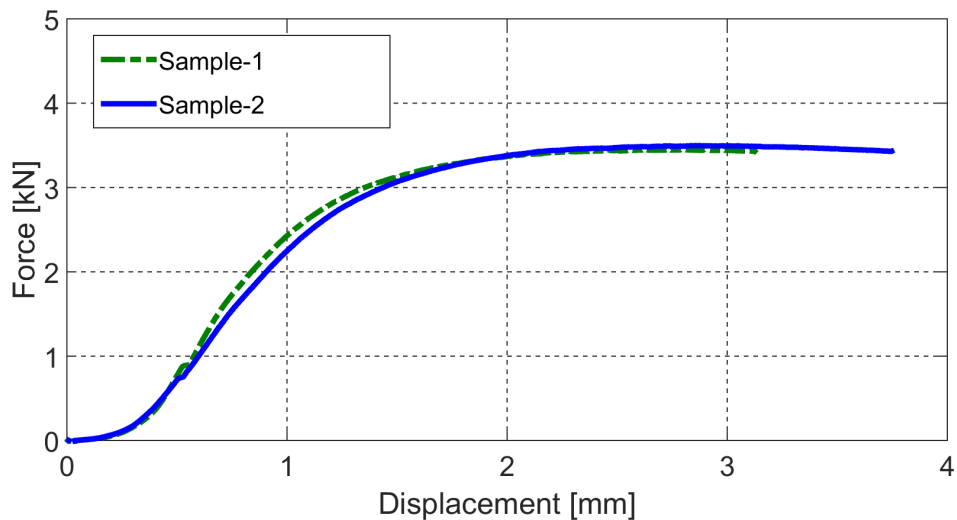


Figure 5.16. Resulting curves of crush test performed on samples of 93% relative density

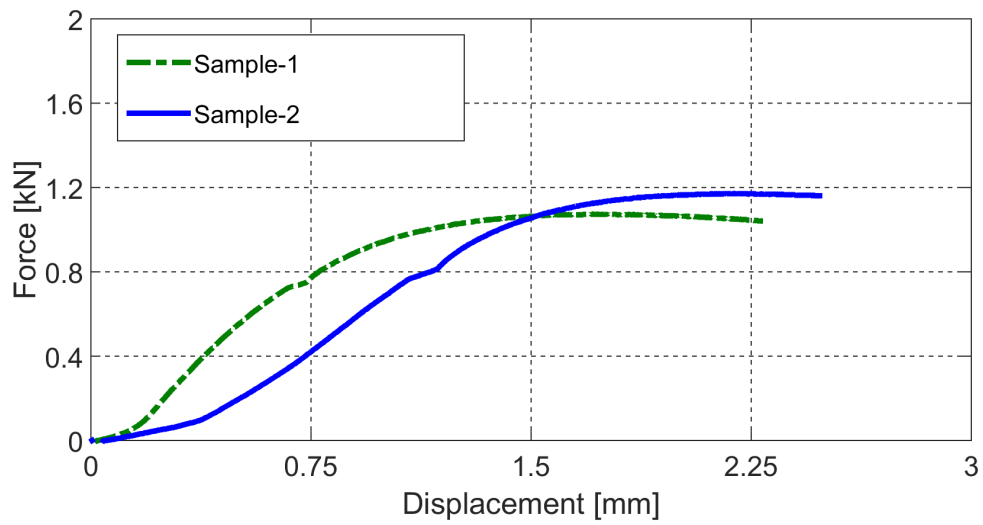


Figure 5.17. Resulting curves of crush test performed on samples of 78% relative density

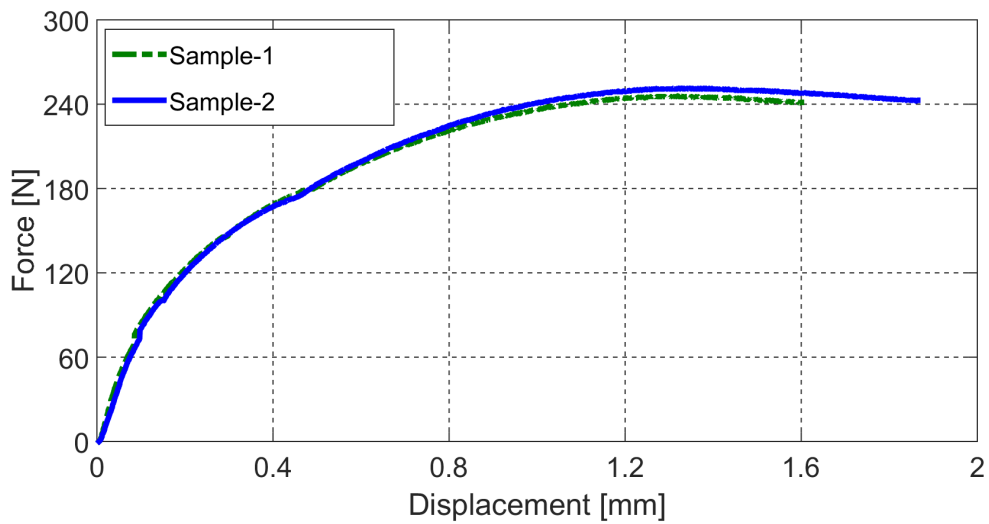


Figure 5.18. Resulting curves of Brazilian test performed on samples of 93% relative density

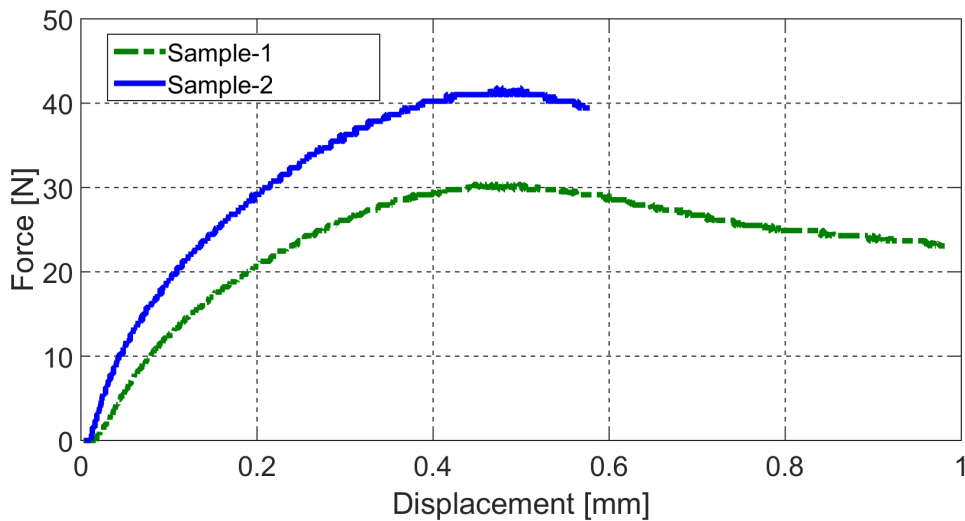


Figure 5.19. Resulting curves of Brazilian test performed on samples of 73% relative density

The bulging in the samples which can be seen in figure 5.14 and crack on the diametrical surface, visualized in figure 5.15, are characteristics of the specimens subjected to crush and Brazilian test, respectively. Force vs. displacement curves of the crush test shown in figure 5.17, corresponding to the sample of a relative density 78% demonstrates that the curves of the two specimens having the same relative density are fairly different. Similar is observed for Brazilian test samples of relative density 73% given in figure 5.19. Such behavior is typically encountered in this research when specimens of low relative density are subjected to destructive tests. As the relative density of the sample increases, the force vs. displacement curves of the two samples at the same density start becoming coherent. Indeed, no such dispersion is noticed on the curves corresponding to samples with higher density, like those in figures 5.16 and 5.18. The difference between the two curves at lower relative densities can be corroborated to the fact that powder particles are still very loosely bonded together. This can clearly be observed from the samples, like those visualized on the left side in figures 5.14 and figure 5.15. The discrepancy between the curves is even more pronounced as the density decreases. Therefore, the results of the commonly used destructive tests are questionable at lower densities. Additional difficulty encountered with the powder studied here is that it turned out to be impossible to eject the samples from the mold, when relative density is lower than 70%. Such circumstances highlights the limitations of the currently applied

procedures for characterizing green body formed at low density, and puts a practical constraint on the specimens of relative density lower than 70%.

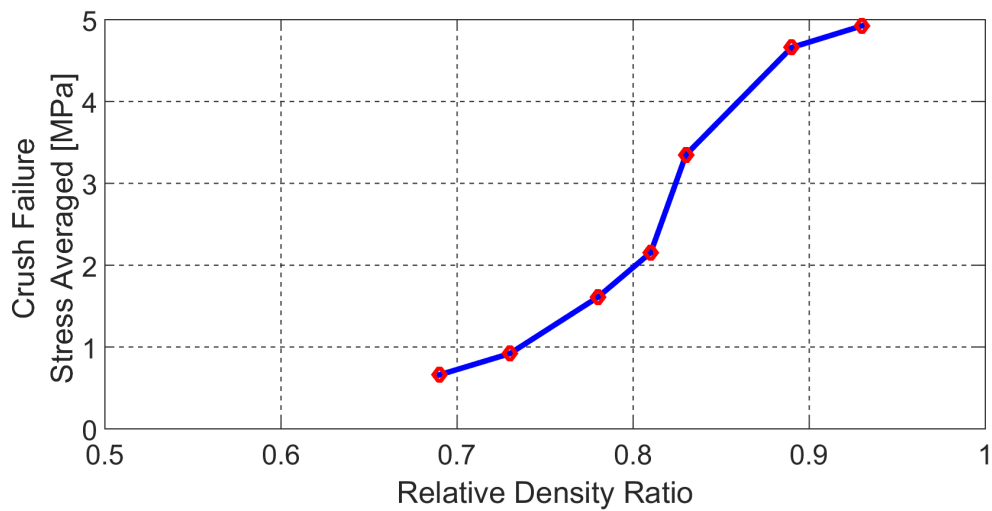
In order to deal more effectively with experimental data having significant variation, it is recommended to produce more samples (usually 5-10) at each density level for crush and Brazilian test to establish statistically meaningful results. However, this increases the number of experiments to be conducted making the procedure industrially very demanding. Since, in the current work destructive tests are performed only to provide reference values of the parameters, further tests are not done. All calculations are therefore performed on two samples for single density, and representative maximum load is taken as averaged value recorded in crush and Brazilian tests. Failure stress can then be calculated using equations (2.11) and (2.10) for crush and Brazilian test, respectively. The results of these calculations are given in the table 5.4 and 5.5. Figures 5.20 and 5.21 graphically show how the assessed failure stresses are changing with relative density.

Table 5.4. Results of the performed crush tests

Sample Name	Maximum Load [kN]	Maximum Load Averaged [kN]	Failure Stress [MPa]	Failure Stress Averaged [MPa]
93-1	3.506	3.48	4.96	4.92
93-2	3.456		4.89	
88-1	3.308	3.29	4.68	4.66
88-2	3.279		4.64	
83-1	2.353	2.37	3.33	3.35
83-2	2.382		3.37	
81-1	1.597	1.52	2.26	2.15
81-2	1.449		2.05	
78-1	1.187	1.14	1.68	1.61
78-2	1.088		1.54	
73-1	0.693	0.65	0.98	0.92
73-2	0.608		0.86	
69-1	0.530	0.47	0.75	0.66
69-2	0.403		0.57	

Table 5.5. Results of the performed Brazilian tests

Sample Name	Maximum Load [N]	Maximum Load Averaged [N]	Failure Stress [MPa]	Failure Stress Averaged [MPa]
93-1	256.43	248.75	1.05	1.02
93-2	241.08		0.99	
88-1	199.67	200.31	0.85	0.85
88-2	200.95		0.86	
83-1	162.92	158.97	0.71	0.69
83-2	155.03		0.68	
81-1	94.25	100.59	0.43	0.46
81-2	106.93		0.49	
78-1	70.84	74.67	0.32	0.34
78-2	78.50		0.36	
73-1	49.50	42.05	0.23	0.19
73-2	34.61		0.16	
69-1	19.76	27.83	0.09	0.13
69-2	35.90		0.17	

**Figure 5.20.** Averaged failure stress of all samples for crush tests

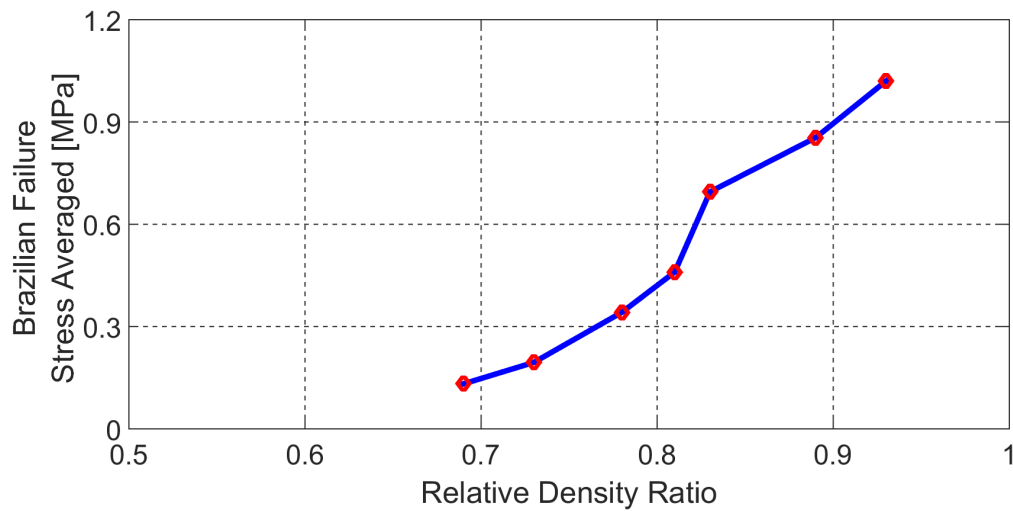


Figure 5.21. Averaged failure stress of all samples for Brazilian tests

5.2 Determination of Parameters Based on Currently Adopted Praxis

Drucker-Prager Cap (DPC) yield surface parameters can be divided into three groups: shear failure surface parameters (cohesion and friction angle), cap surface parameters (cap eccentricity and evolution pressure) and the transition surface parameter (transition surface radius). Here, the transition radius (α) is treated as a constant with an assumed value of 0.025 as usually it is suggested to be within the range of 0.01 and 0.05 [28, 70]. Comparative numerical results also confirmed that there is a very small influence of the value of this parameter to the pressing curve. Hydrostatic yield compression stress (p_b) can be calculated from the values of cohesion (d), friction angle (β), cap eccentricity (R) and evolution pressure (p_a) using equation (2.6). Therefore, four plastic parameters (d , β , R and p_a) along with the two elastic parameters (E and ν) need to be evaluated as a function of relative density for full characterization of the alumina-graphite mixture considered in this research. Clearly, these parameters cannot be assessed as a continuous function of relative density, but in a discrete manner corresponding to previously mentioned seven relative densities, for which the data are available. More precise "resolution" would require additional green bodies, and hence make the procedure even

more time consuming. The evaluation of above listed parameters is given in what follows.

5.2.1 Shear Failure Surface Parameters

In the 2-D p - q space, where p is the hydrostatic pressure and q is the equivalent von Mises stress, the shear failure surface is represented by a single line. Failure stress values of the samples having the same relative density from both crush and Brazilian test are used to find the corresponding point in p - q plane of the two tests for that particular density using equations (2.12), (2.13), (2.14) and (2.15). Point (p_c, q_c) of the crush test and (p_d, q_d) of the Brazilian test, represent two points in the p - q plane (refer to figure 2.4). Therefore, the shear failure line can be determined from these two points, where the slope of the line is the friction angle while the intercept on the y -axis is the cohesion, assessed from equations (2.16) and (2.17). For detailed description, see section 2.2.1.

The averaged failure stress values given in tables 5.4 and 5.5 are used to find the points (p_c, q_c) and (p_d, q_d) at each relative density. These values of p and q from both crush test and Brazilian tests are then utilized to assess material cohesion and friction angle. The parameters are determined at seven levels of relative densities namely, 69%, 73%, 78%, 81%, 83%, 89%, and 93%. Results are presented in table 5.6 and figures (5.22 and 5.23).

Table 5.6. Assessed parameters defining the shear failure surface of DPC yield function

Relative Density	p_c [MPa]	q_c [MPa]	p_d [MPa]	q_d [MPa]	Cohesion [MPa]	Friction Angle [Degrees]
0.93	1.64	4.92	0.68	3.68	2.80	52.22
0.88	1.55	4.66	0.57	3.07	2.16	58.18
0.83	1.12	3.35	0.47	2.52	1.93	51.89
0.81	0.72	2.15	0.31	1.66	1.29	50.16
0.78	0.54	1.61	0.23	1.23	0.95	50.76
0.73	0.31	0.92	0.13	0.69	0.52	52.34
0.69	0.22	0.66	0.09	0.47	0.34	55.12

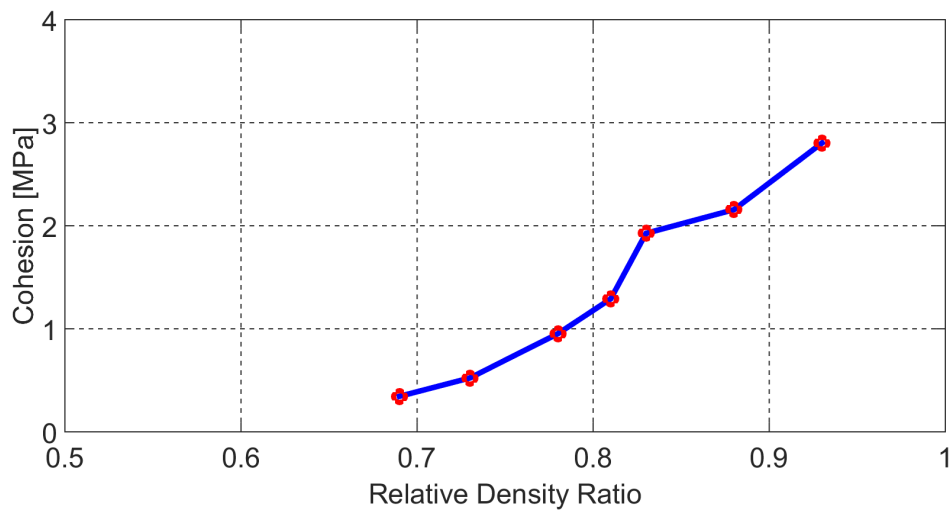


Figure 5.22. Experimentally determined cohesion as a function of relative density

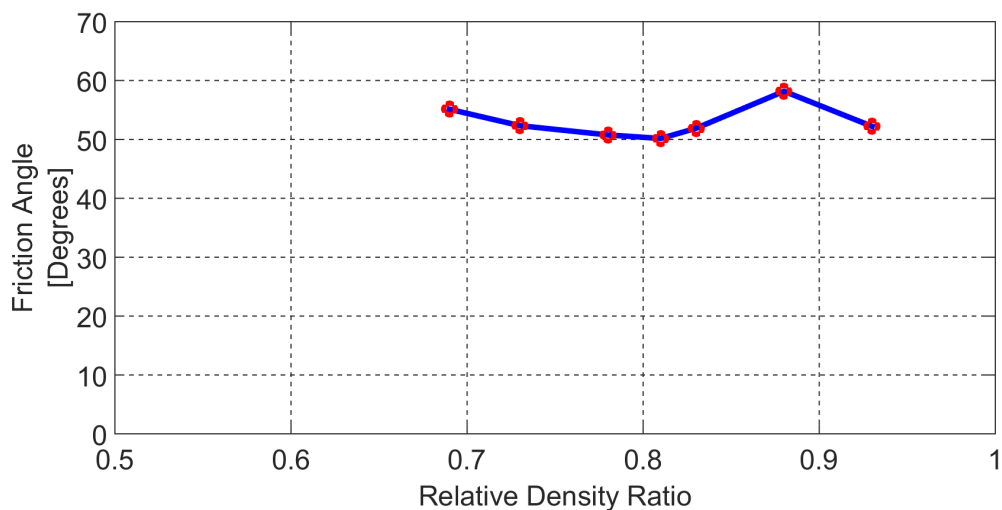


Figure 5.23. Experimentally determined friction angle as a function of relative density

5.2.2 Cap Surface Parameters

To determine R and p_a , stress state of the point corresponding to the intersection of loading path of the green body and the cap surface is analyzed (see figure 2.5). The stress state of this point can be fully characterized by the axial stress, axial strain and radial stress under the assumption that the die-wall is rigid. As the compaction progresses, cap surface continuously expands uniquely representing a particular density at every instance during the compaction. Since the point lies on the cap surface, yielding is active at this point and therefore, equation (2.4) is satisfied. Given that the information on the stress state of this

point is available, it can be converted to hydrostatic pressure (p_0) and equivalent von Mises stress (q_0) following equations (2.18) and (2.19). If the friction angle is known, R can be evaluated, by setting the radial plastic strain rate at (p_0, q_0) equal to zero (since the die-wall is assumed to be rigid), as visualized in equations (2.22) and (2.21). By substituting the value of R into formula (2.4), p_a can be determined as shown in equation (2.23), if the cohesion is known. Since the values of cohesion and friction angle are available only at discrete relative density points, R and p_a can also be evaluated only at these particular densities. Detailed explanations can be found in section 2.2.2.

Axial and radial stresses are continuously recorded throughout the compaction and the curves are given in figures 5.8 to 5.10. Given that the values of cohesion and friction angle are available only for relative densities of 69%, 73%, 78%, 81%, 83%, 89%, and 93%, consequently, R and p_a can be evaluated at these particular relative densities. However, in the current work, radial stresses were only measured from the samples that are formed for the calibration through IA. Therefore, the maximum relative density (see table 5.3) up to which R and p_a can be estimated is 89%, corresponding to configuration-1. Using the values of axial and radial stress (corresponding to bottom gage) from configuration-1 along with cohesion and friction angle from 5.6, cap eccentricity and evolution pressure are assessed from equations (2.22) and (2.23). Hydrostatic yield compression stress (p_b) is calculated from formula (2.6). The results are presented in table 5.7 and figures 5.24 to 5.26.

Table 5.7. Assessed parameters defining the cap surface of DPC yield function

Relative Density	p_0 [MPa]	q_0 [MPa]	Cap Eccentricity	Evolution Pressure [MPa]	Hydrostatic Yield Compression Stress [MPa]
0.88	17.84	10.74	0.71	8.94	20.70
0.83	11.56	7.08	0.66	6.57	13.41
0.81	9.68	5.92	0.63	5.93	11.24
0.78	7.41	4.54	0.63	4.51	8.61
0.73	4.55	2.96	0.61	2.80	5.33
0.69	2.67	1.80	0.62	1.54	3.14

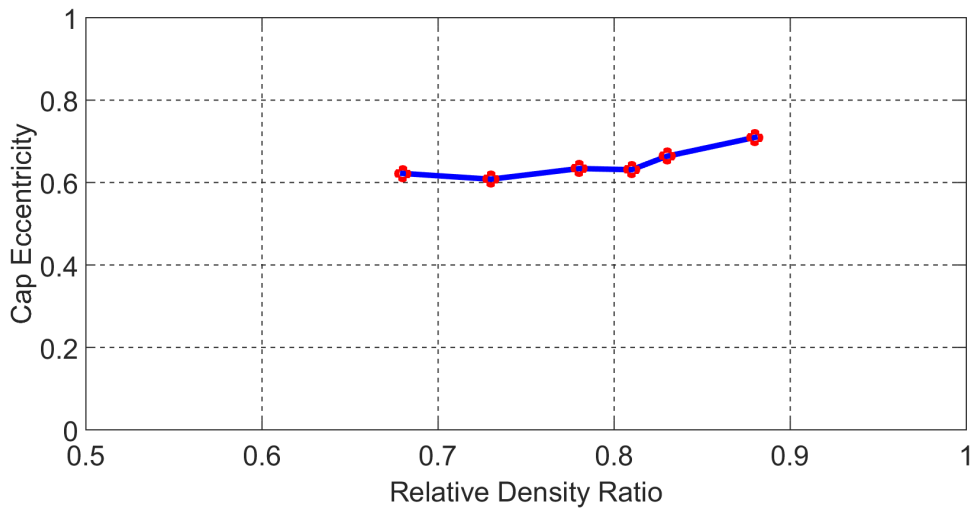


Figure 5.24. Experimentally determined cap eccentricity as a function of relative density

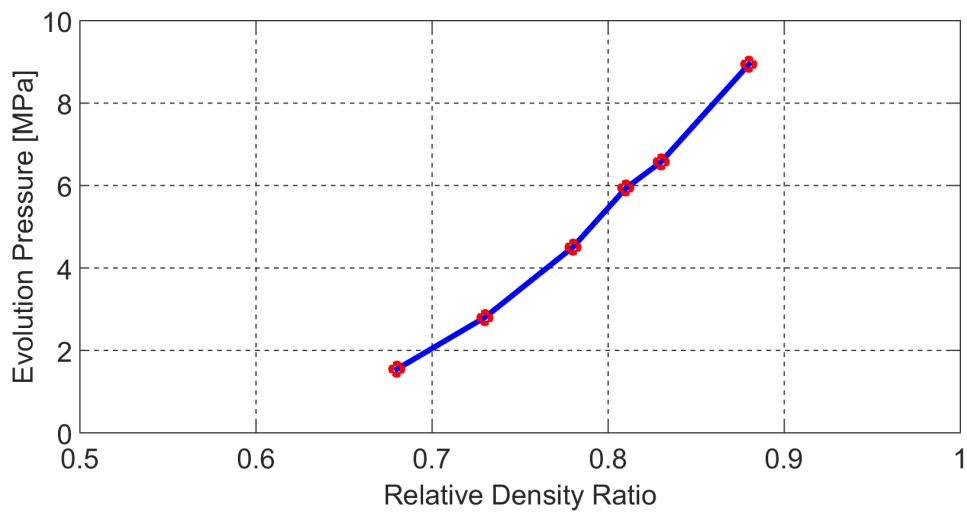


Figure 5.25. Experimentally determined evolution pressure as a function of relative density

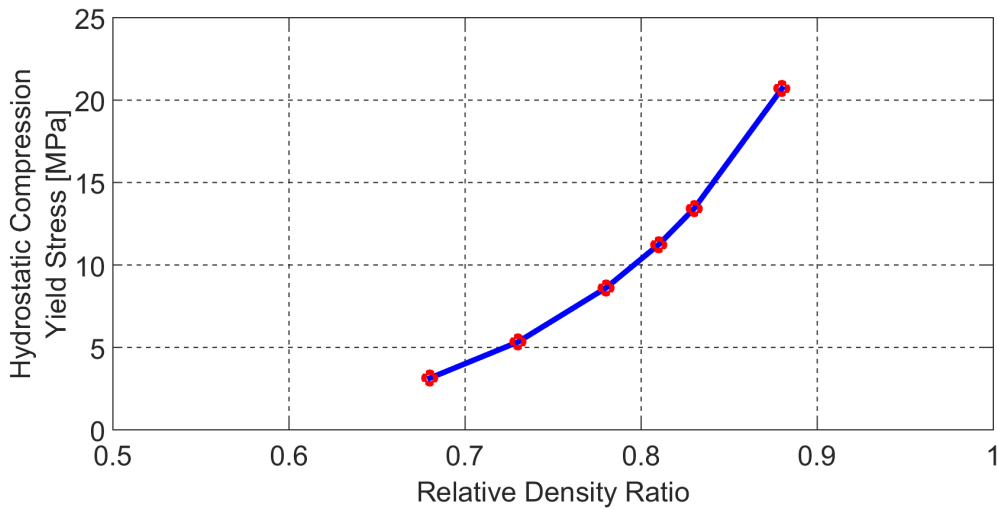


Figure 5.26. Experimentally determined hydrostatic yield compression stress as a function of relative density

5.2.3 Elastic Parameters

The elastic behavior of the compacting powder is assumed to be isotropic, therefore, only two elastic parameters, namely, Young's modulus (E) and Poisson's ratio (ν) are evaluated. Poisson's ratio is assessed from the slope of the unloading part of axial stress vs. radial stress curve following equation (2.31). Young's modulus is evaluated on the basis of formula (2.32) using Poisson's ratio and the slope of the unloading curve of axial stress vs. axial strain graph. This implies that axial and radial stresses need to be measured by forming green bodies at different relative densities.

In the current research, the focus is on applying new methodology for calibration of DPC yield function and hence, such extensive experimentations are not carried out. A simplified approach is followed and the Poisson's ratio is assumed to lie between 0.05 and 0.30, as this is the typical range for such powder mixtures. Force vs. displacement data of the compaction tests (to form crush test samples) is converted to axial stress vs. axial strain curve. The slope of the first 20% of the unloading curve is taken for the calculations. The slope of this 20% of the unloading plot along with the limit values of Poisson's ratio (0.05 and 0.3) are used as inputs to the equation (2.32) to give two corresponding limit values of Young's modulus. This is done for five different compaction curves corresponding to

samples of 93%, 89%, 83%, 78%, and 73% relative density. The results are presented in table 5.8 and figure 5.27.

Table 5.8. Assessed Young's modulus corresponding to Poisson's ratio of 0.05 and 0.3

Relative Density	Young's Modulus [GPa] for Poisson's Ratio = 0.05	Young's Modulus [GPa] for Poisson's Ratio = 0.30
0.93	2.62	2.12
0.88	2.37	1.85
0.83	1.92	1.46
0.78	1.68	1.27
0.73	1.15	0.86

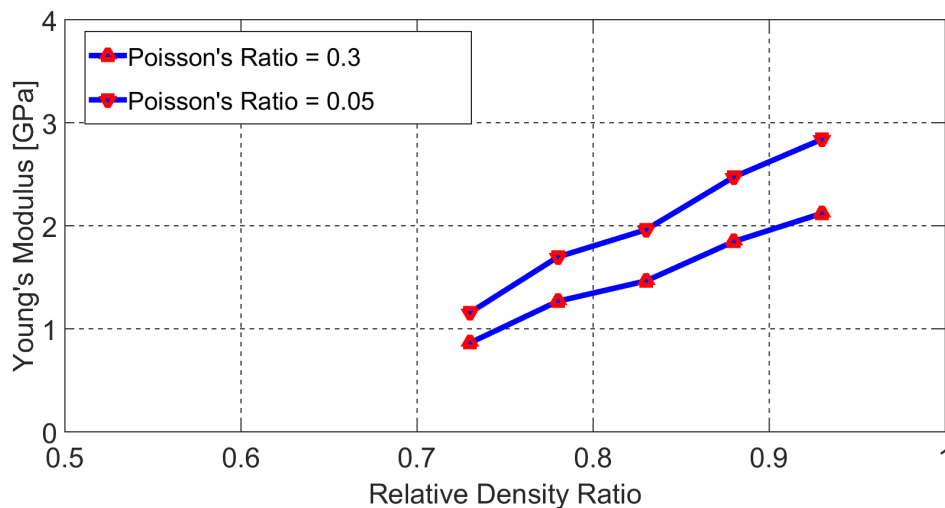


Figure 5.27. Experimentally determined Young's modulus as a function of relative density

5.3 Determination of Parameters based on Inverse Analysis

To setup the Inverse Analysis (IA) procedure, measurable quantities which are the compaction curve and radial stress measurements in two different points are collected from both the experiment and its simulation. Source of the experimental data to be considered as inputs to IA are the results of pressing tests (figures 5.8 to 5.10) performed to form green bodies of configurations -1 to -4 (see figures 4.1a and 4.10). Numerically computed counterpart of these quantities are collected from the simulations through

finite element models done in ABAQUS [1]. For each of the configurations -1 to -4, separate finite element models are built, corresponding to the experimental conditions given in table 5.3. Configuration-1 is modeled as 2-D to exploit the axial symmetry and the specimen is discretized into 672 four-node fully integrated axisymmetric elements (marked by CAX4 in ABAQUS), while 3-D models of configurations -2 to -4 contain 3200 eight-node fully integrated tri-linear iso-parametric elements (marked by C3D8 in ABAQUS). Other simulation conditions are those given in section 3.1.2.

Simulations are performed within the force control regime and a maximum load of 17 kN is used corresponding to peak force applied within the experiments to form green bodies exploiting configurations -1 to -4. Therefore, the displacements from the compaction curves along with the measured radial stresses corresponding to middle and bottom gage are considered (both from the experiment and its simulation) from all configurations, to form the residual vector, which is constructed as the difference between experimentally measured data and its simulated counter-parts. There are 300 entries in residual vector corresponding to one configuration, where 100 points are the differences between displacements corresponding to a certain level of force for the compaction curves, while 200 points (100 for middle and additional 100 for bottom gage) are the differences between the radial stresses. The collected measurements in the residual vector are then normalized for both displacements and radial stresses separately, to ensure similar contribution of these entities to the overall discrepancy between experimental and computed results. As the next step, discrepancy function is formed as the sum of the squares of the members of residual vector. Finally, the so formed discrepancy function is iteratively minimized with respect to the sought parameters. For minimization, Trust Region Algorithm (TRA) based on 2-D subspace minimization already implemented in MATLAB [41] is used. Detailed explanations on the construction of discrepancy function along with main features of TRA are outlined in Chapter 3.

The sought parameters are four plastic (d, β, R, p_b) and two elastic parameters (E and ν) along with the coefficient of friction between the powder and mold/punches. Note that in the numerical implementation of DPC yield criterion in ABAQUS, hydrostatic yield compression stress (p_b) is used instead of evolution pressure (p_a). Further on, transition

surface radius (α), to which usually a value is attributed within a range of 0.01 and 0.05 [1] is assumed as a constant here, throughout the compaction and therefore not subjected to the identification. In order to motivate this assumption, simulations are performed considering $\alpha = 0.01$ in one case, and $\alpha = 0.05$ in another, while keeping all the other parameters fixed. The results of the simulation can be visualized in figure 5.28. Indeed, the value of α has marginal influence on the compaction simulation as the curves are practically the same for both cases, justifying the assumption to treat α as a constant.

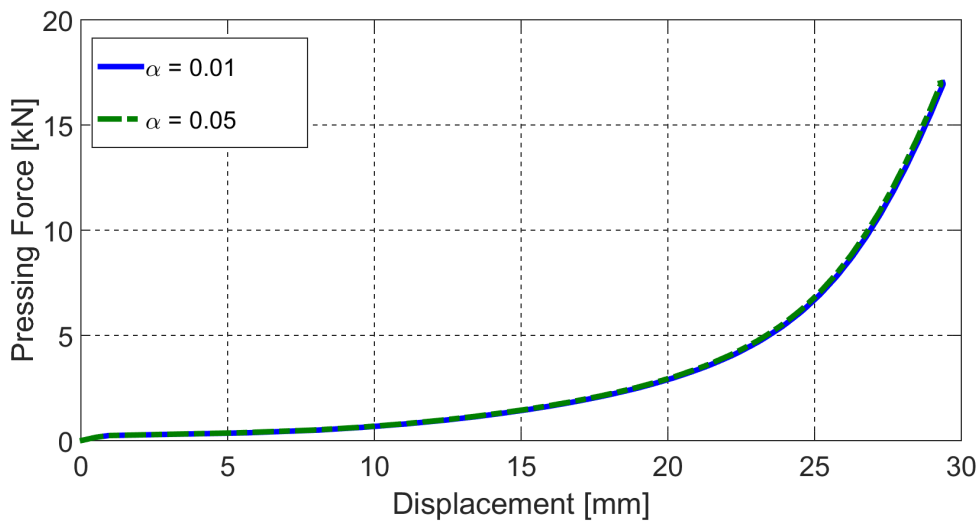


Figure 5.28. Effect of transition surface radius on the simulated compaction curve

Given that the DPC model is modified to include dependency of parameters on relative density, plastic (d , β , R , p_b) and elastic parameters (E, ν) are assessed as a function of relative density by using the proposed relation (3.3). According to it, each parameter is quantified by its initial value (corresponding to initial relative density, here specifically taken as 0.5), final value (final relative density, here adopted as 0.95) and the exponent governing the transition of the parameter from initial to final value. All the six material parameters (four plastic and two elastic) are assessed in this manner, while the friction coefficient is evaluated as a single value independent of the relative density, making a total of 19 parameters that are subjected to identification. The initial and final relative densities are *a priori* selected and not considered for the evaluation.

To start the IA procedure, parameters are initialized with some "expert" values and are searched within certain bounds which are selected based on the expected range of the

properties of alumina-graphite powder mixture. Further on, the parameters are normalized between 0 and 1, where 0 represents the lower bound and 1 is the upper bound. For the minimization of discrepancy function employing TRA, gradients are calculated using a forward difference with a perturbation of 10^{-4} . This implies that the number of simulations is one more than the number of sought parameters for one iteration. The iterative procedure is stopped when the change in the objective function is less than 10^{-6} or when the difference between the norm of the parameter vector within two consecutive iterations is lower than 10^{-2} . Note that the range of relative density (0.5-0.95) in which the parameters are assessed, the value of transition radius ($\alpha = 0.025$) and the mentioned algorithm tolerances are kept the same for all the inverse analyses shown in this Chapter.

As the final step to design a calibration protocol based on Inverse Analysis (IA) methodology, it is important to determine the minimum number of experiments needed to be used as inputs for the IA procedure. To this purpose, a combination of experiments (i.e. configurations -1 to -4) are selected and the results are presented in what follows.

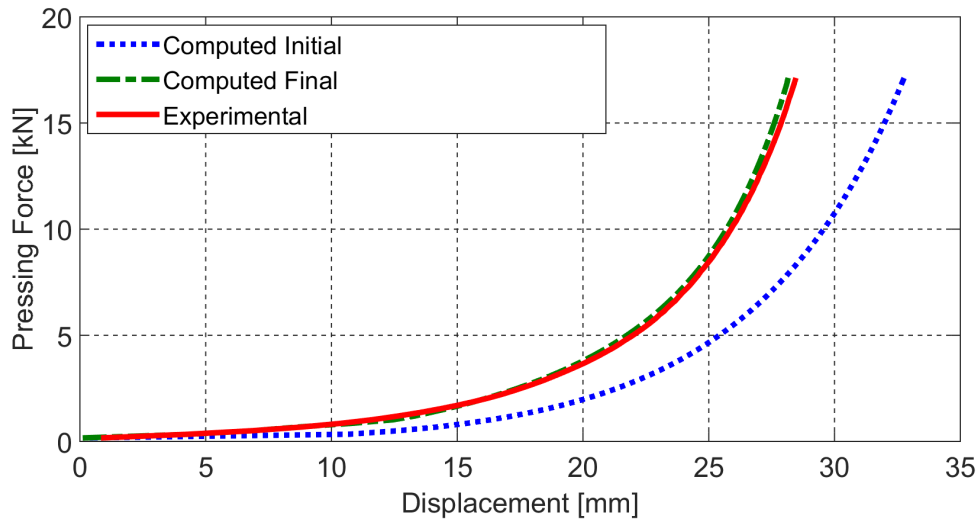
5.3.1 Results of IA by Employing Two Configurations

As shown in Chapter 4, employing only configuration-1 was not enough to evaluate the representative material properties. Therefore, the next logical step is to try and assess the parameters employing two configurations. In the first attempt, inverse analysis relying on the experimental data (compaction and radial stress curves) of two configurations (-1 and -2) was used. The IA procedure terminated after six iterations. Computations are done on a regular desktop computer with a 3.1 GHz (intel i-7) processor and 16 G-Byte RAM. The computational time required for one iteration on this computer is about 4 hours, implying total time needed for a full inverse analysis to be approximately 1 day.

Assessed parameters are given in table 5.9. Compaction curves corresponding to the final parameters are given in figures 5.29 and 5.30. Note that the radial stress curves corresponding to middle and bottom gages are also used as inputs to the IA procedure but the curves are omitted here for brevity.

Table 5.9. Final parameters corresponding to IA identification employing configuration-1 and -2 as inputs

Parameter	Initial Value ($\rho_0 = 0.50$)	Final Value ($\rho_f = 0.95$)	Exponent
Young's Modulus	0.031 [GPa]	1.041 [GPa]	4.082
Poisson's Ratio	0.112	0.241	1.587
Material Cohesion	0.367 [MPa]	2.796 [MPa]	1.596
Friction Angle	56.877 ^[o]	50.808 ^[o]	1.601
Cap Eccentricity	0.153	0.788	1.842
Hydrostatic Yield Stress	0.145 [MPa]	36.078 [MPa]	3.014
Friction Coefficient	0.247		

**Figure 5.29.** Experimental vs. computed compaction curves for configuration-1 corresponding to parameters identified through IA employing configuration-1 and -2 as inputs

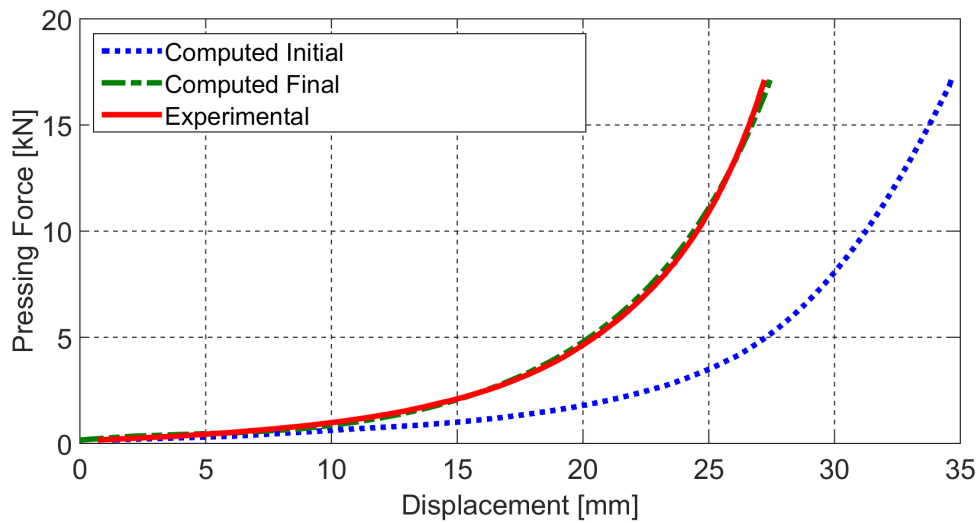


Figure 5.30. Experimental vs. computed compaction curves for configuration-1 corresponding to parameters identified through IA employing configuration-1 and -2 as inputs

The above figures show a good agreement between the experimental and computed curves, as the inverse converged to a global minimum. To assess if the parameters identified are the representative material parameters, configurations -3 and -4 are simulated using the same parameters. The compaction curves corresponding to the two configurations are given in 5.31 and 5.32.

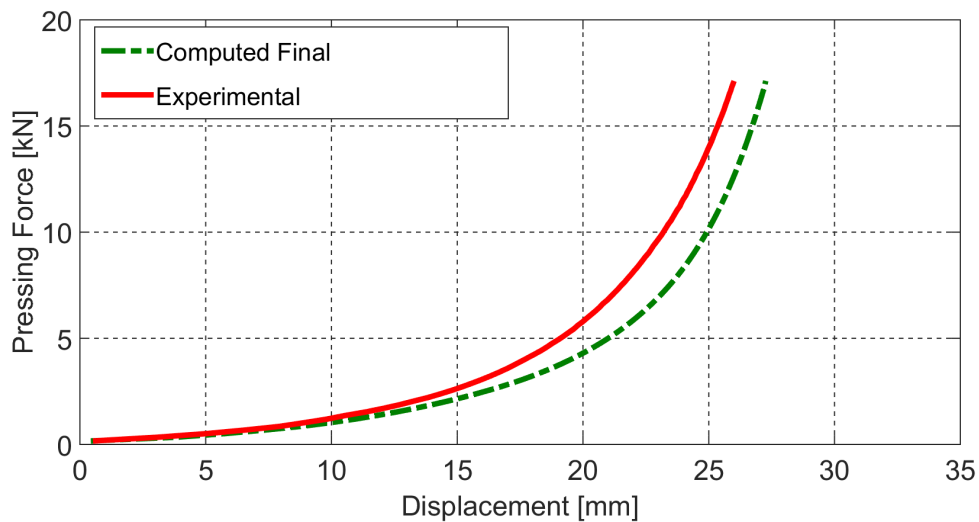


Figure 5.31. Experimental vs. final compaction computed curve for configuration-3 corresponding to parameters identified through IA employing configuration-1 and -2 as inputs

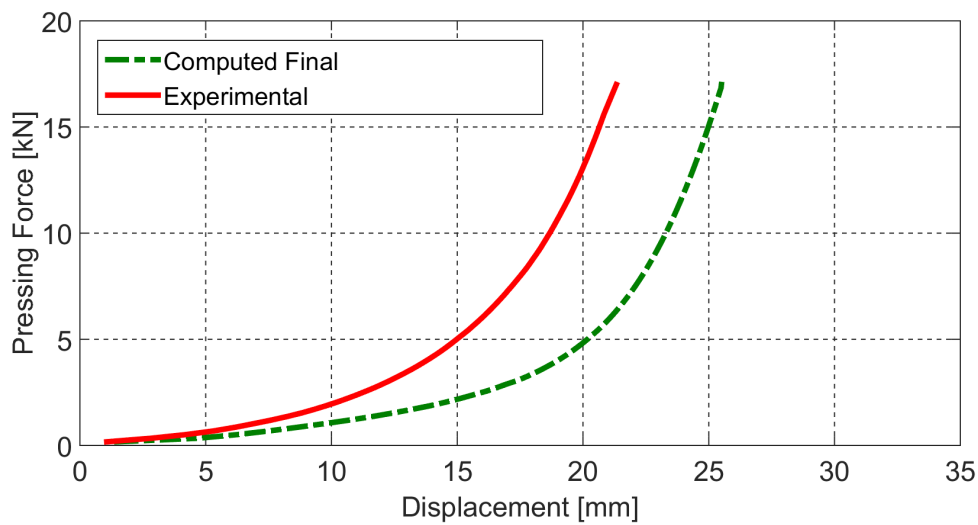


Figure 5.32. Experimental vs. final computed compaction curve for configuration-4 corresponding to parameters identified through IA employing configuration-1 and -2 as inputs

Clearly, it can be observed that the parameters assessed by employing only two configurations are not representative material parameters, as they cannot fit other experiments. Therefore, similarly to the identification where only one configuration is used, the solution to the inverse analysis represents a fitting of data specific to the experiments, and clearly are not possessing the uniqueness of the solution. Similar results are observed when using other combinations like configuration -1 and -3, configuration -2 and -4, etc. These investigations illustrate that the measurable quantities collected from two experiments are not rich enough to calibrate the DPC model. For further enrichment of the experimental data, the combination of three configurations is considered. Assessed results are given in what follows.

5.3.2 Results of IA by Employing Three Configurations

Three configurations selected as the source of input data to IA procedure are configurations -1, -2 and -3. Configuration-2 has the most heterogeneous state of stress, while the stress path of certain elements in configuration-3 lies in the close vicinity of shear failure line of DPC yield function (see 4.1). It is therefore expected that this combination provides reasonable diversity of stress paths covered by certain material points, generating experimental data good enough to calibrate all the parameters of the

considered model. Indeed, the combination of these configurations turned out to be enough to calibrate the DPC model parameters. IA procedure is started using compaction and radial stress curves from these three configurations. The IA procedure finished after only 7 iterations in a total time of about 45 hours. The solution to the inverse problem is found as demonstrated in figures 5.33 to 5.41. Identified parameters are given in table 5.10.

Table 5.10. Final parameters corresponding to IA identification employing configuration-1, -2 and -3 as inputs

Parameter	Initial Value ($\rho_0 = 0.50$)	Final Value ($\rho_0 = 0.95$)	Exponent
Young's Modulus	0.248 [GPa]	2.907 [GPa]	1.577
Poisson's Ratio	0.048	0.204	3.128
Material Cohesion	0.257 [MPa]	3.274 [MPa]	2.909
Friction Angle	49.640 ^[o]	56.836 ^[o]	1.272
Cap Eccentricity	0.521	0.740	1.166
Hydrostatic Yield Stress	0.230 [MPa]	35.581 [MPa]	3.032
Friction Coefficient	0.051		

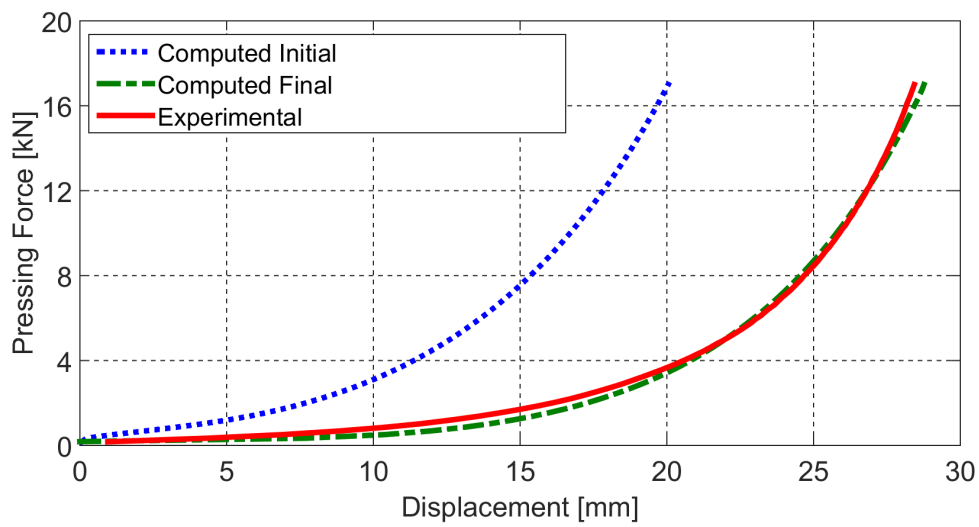


Figure 5.33. Experimental vs. computed compaction curves for configuration-1 corresponding to parameters identified through IA employing configuration-1, -2 and -3 as inputs

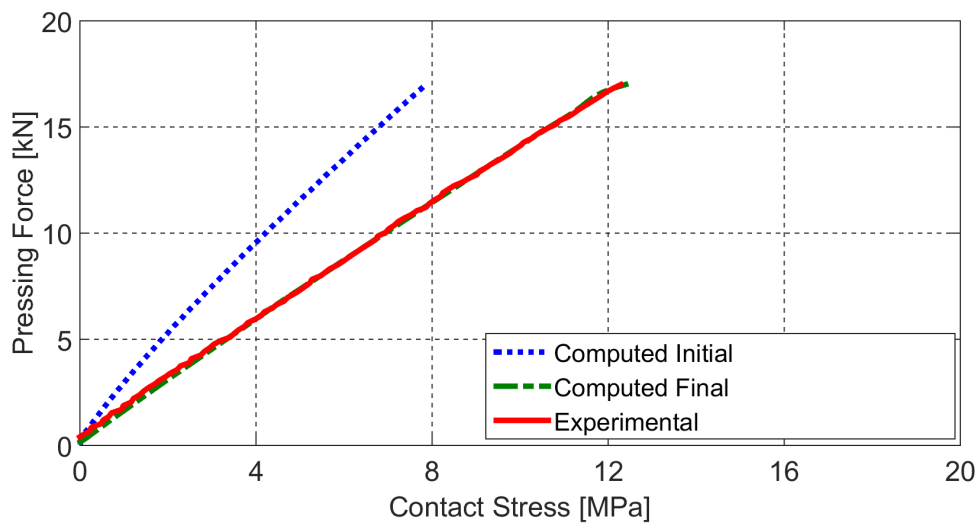


Figure 5.34. Experimental vs. computed radial stress curves (middle gage) for configuration-1 corresponding to parameters identified through IA employing configuration-1, -2 and -3 as inputs

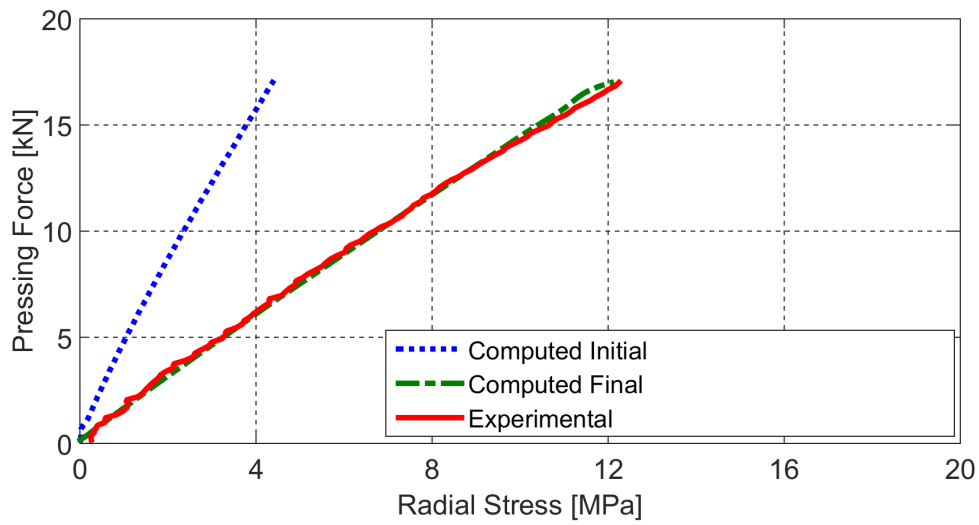


Figure 5.35. Experimental vs. computed radial stress curves (bottom gage) for configuration-1 corresponding to parameters identified through IA employing configuration-1, -2 and -3 as inputs

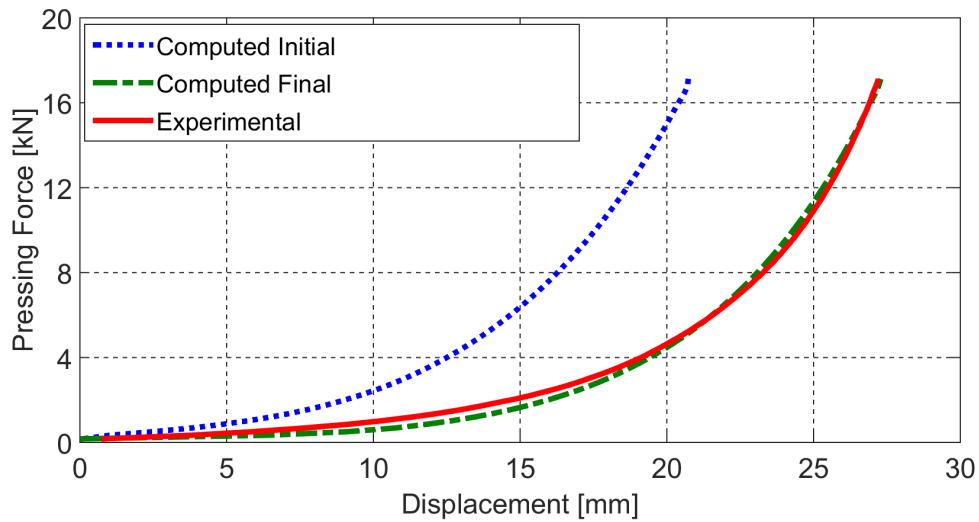


Figure 5.36. Experimental vs. computed compaction curves for configuration-2 corresponding to parameters identified through IA employing configuration-1, -2 and -3 as inputs

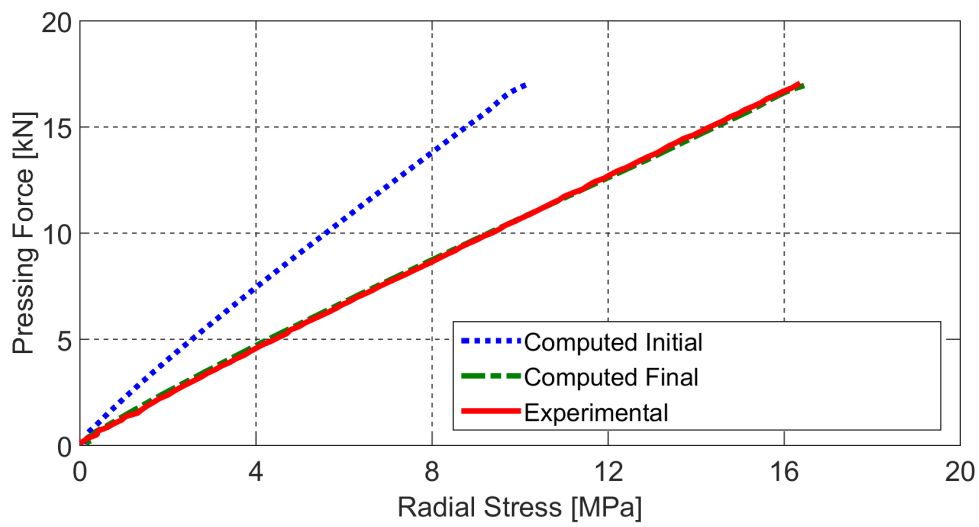


Figure 5.37. Experimental vs. computed radial stress curves (middle gage) for configuration-2 corresponding to parameters identified through IA employing configuration-1, -2 and -3 as inputs

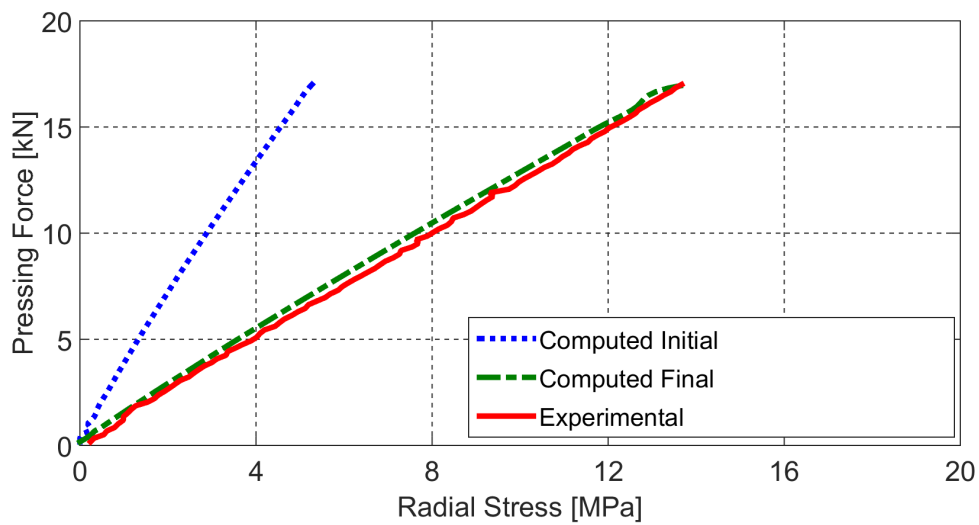


Figure 5.38. Experimental vs. computed radial stress curves (bottom gage) for configuration-2 corresponding to parameters identified through IA employing configuration-1, -2 and -3 as inputs

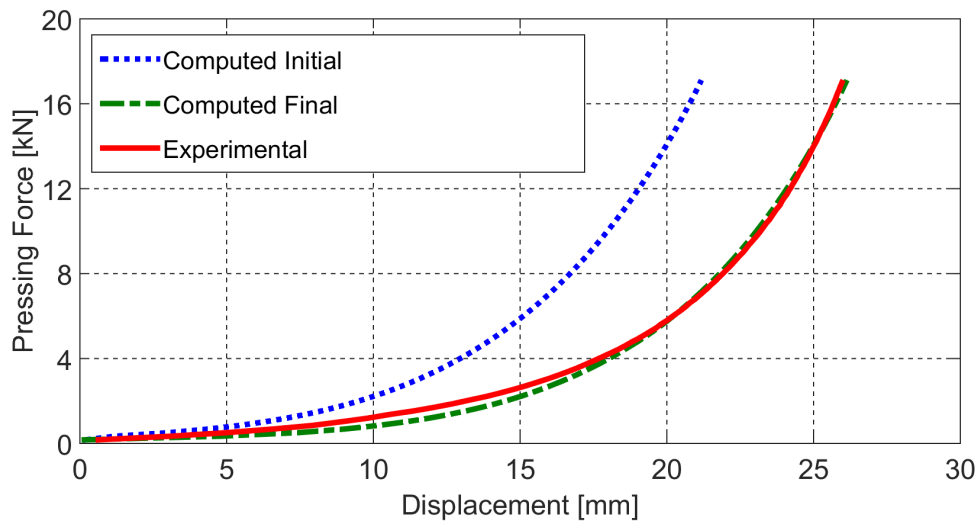


Figure 5.39. Experimental vs. computed compaction curves for configuration-3 corresponding to parameters identified through IA employing configuration-1, -2 and -3 as inputs

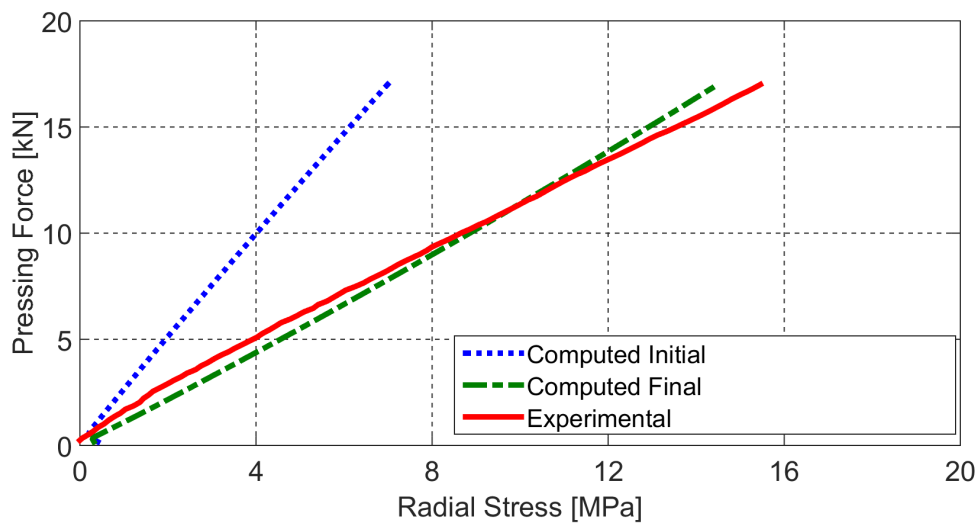


Figure 5.40. Experimental vs. computed radial stress curves (middle gage) for configuration-3 corresponding to parameters identified through IA employing configuration-1, -2 and -3 as inputs

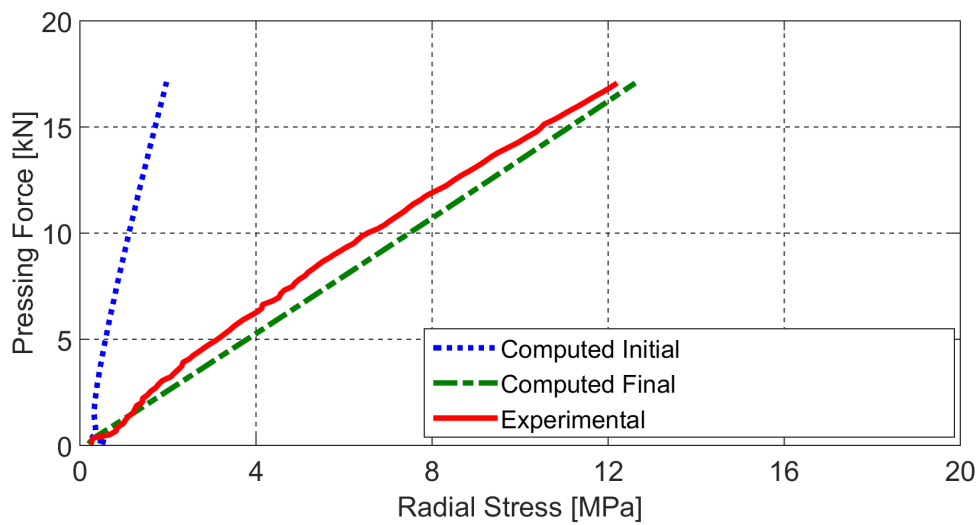


Figure 5.41. Experimental vs. computed radial stress curves (bottom gage) for configuration-3 corresponding to parameters identified through IA employing configuration-1, -2 and -3 as inputs

From the above figures it can be observed that there is a good agreement between the experimental and the final computed curves (both compaction and radial stresses curves) for configurations -1, -2 and -3. For verification purposes, the assessed parameters are used to simulate the configuration-4. Corresponding compaction curve along with the experimental one given in 5.42 shows an excellent agreement between the two.

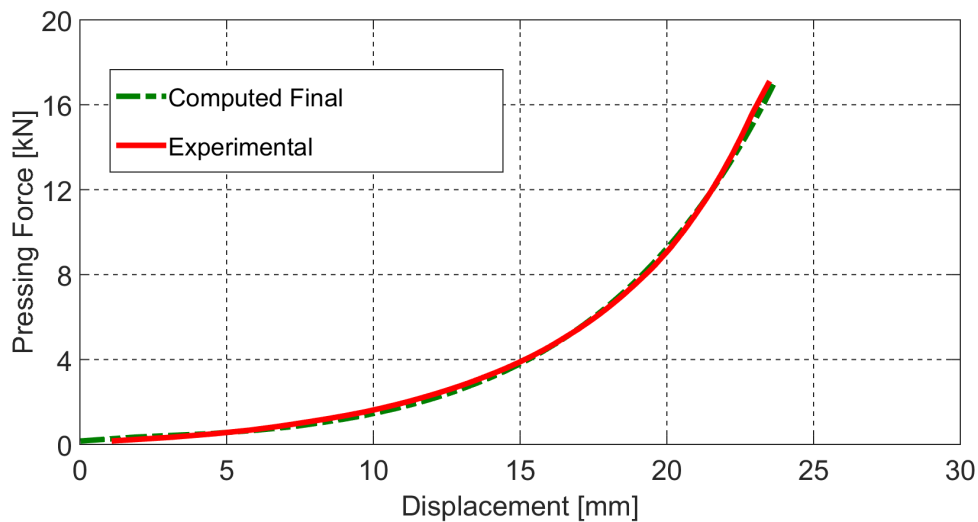


Figure 5.42. Experimental vs. final computed compaction curve for configuration-4 corresponding to parameters identified through IA employing configuration-1, -2 and -3 as inputs

To further verify the uniqueness of the solution, an additional IA is performed using a different parameter initialization. The IA procedure required 7 iterations taking a total time of about 42 hours. The obtained compaction curves corresponding to configurations -1, -2 and -3 are given in figures 5.43 to 5.45. Radial stress curves are not shown here for brevity.

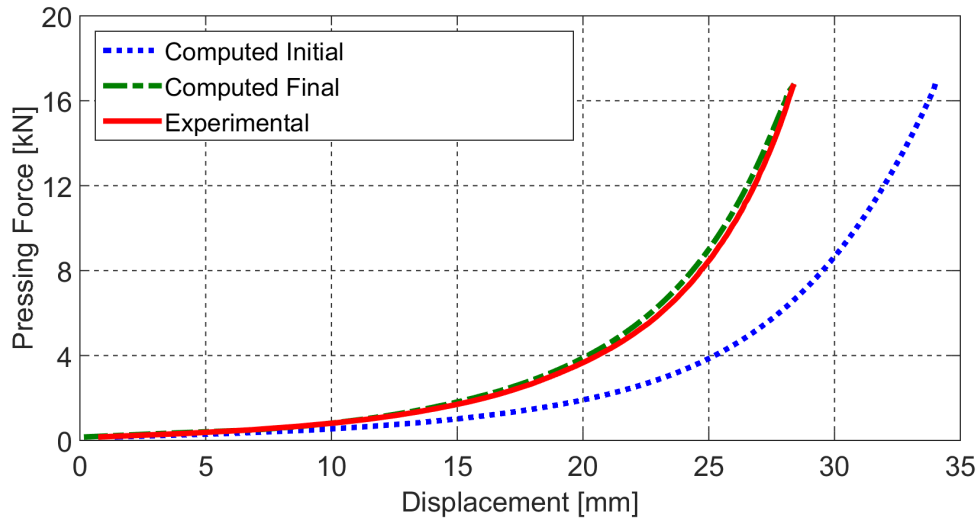


Figure 5.43. Experimental vs. computed compaction curves for configuration-1 corresponding to parameters identified through IA starting from a different initialization

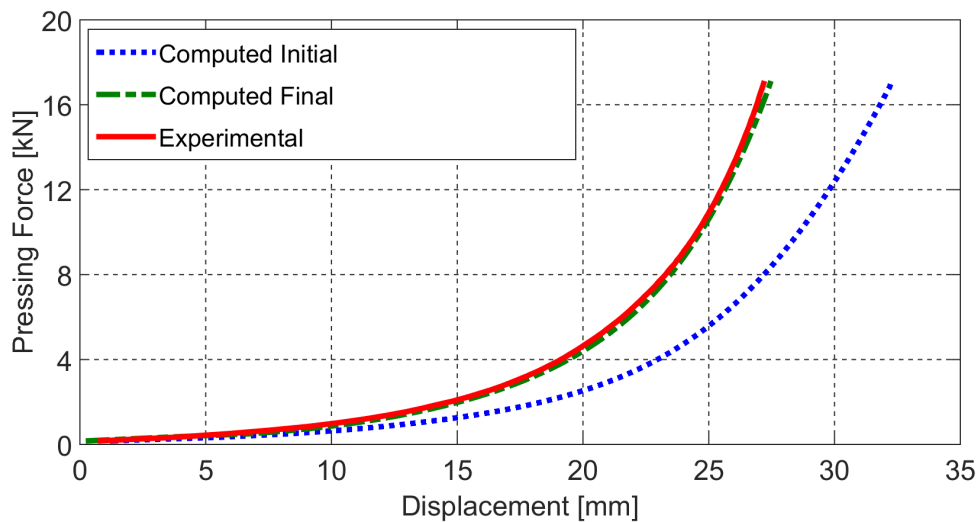


Figure 5.44. Experimental vs. computed compaction curves for configuration-2 corresponding to parameters identified through IA starting from a different initialization

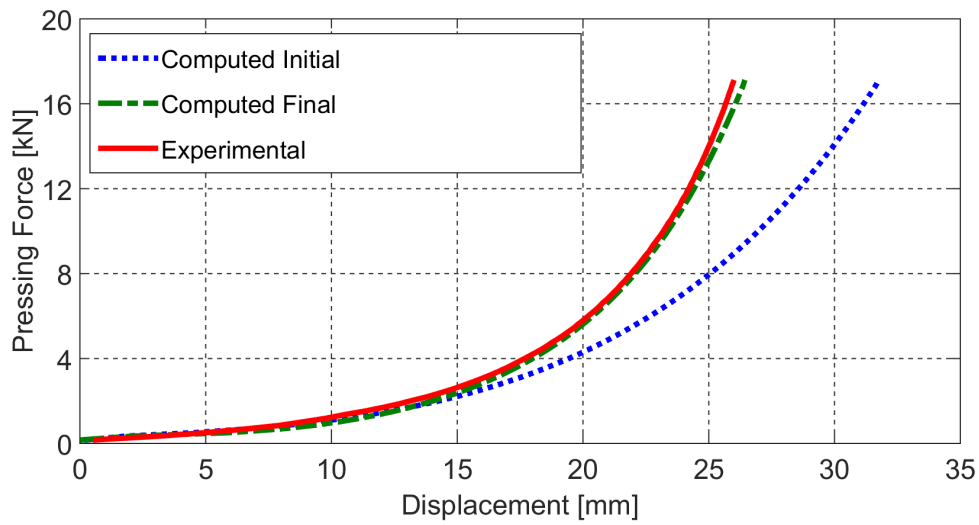


Figure 5.45. Experimental vs. computed compaction curves for configuration-3 corresponding to parameters identified through IA starting from a different initialization

Identified parameters upon starting IA from a different initialization led to a good agreement between the experimental and computed compaction curves. Assessed parameters from the two initializations are also found to be very similar. The change in the values of some selected parameters over the course of IA for both initializations are demonstrated in the form of convergence plots given in figures 5.46 to 5.47. Here, initialization-1 refers to results contained in table 5.10, while initialization-2 is the second one.

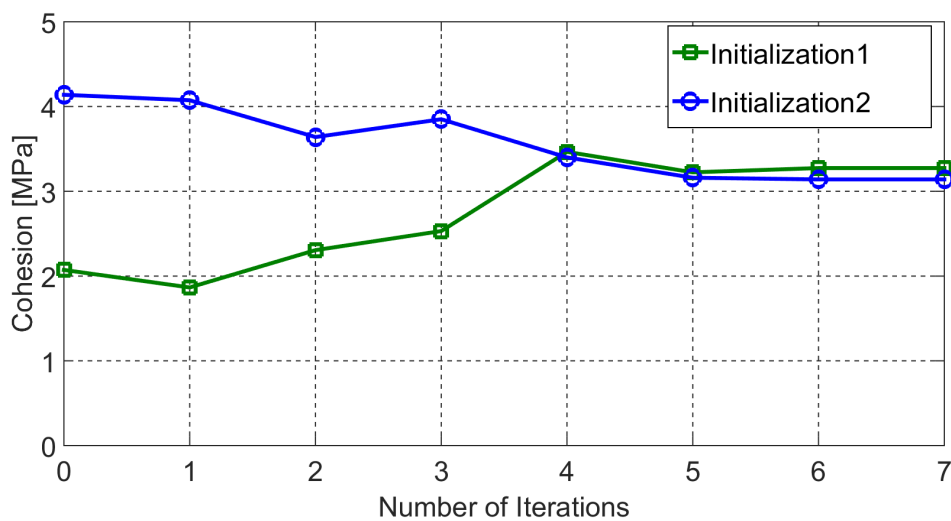


Figure 5.46. Convergence plot of cohesion for IA starting from 2 different initializations

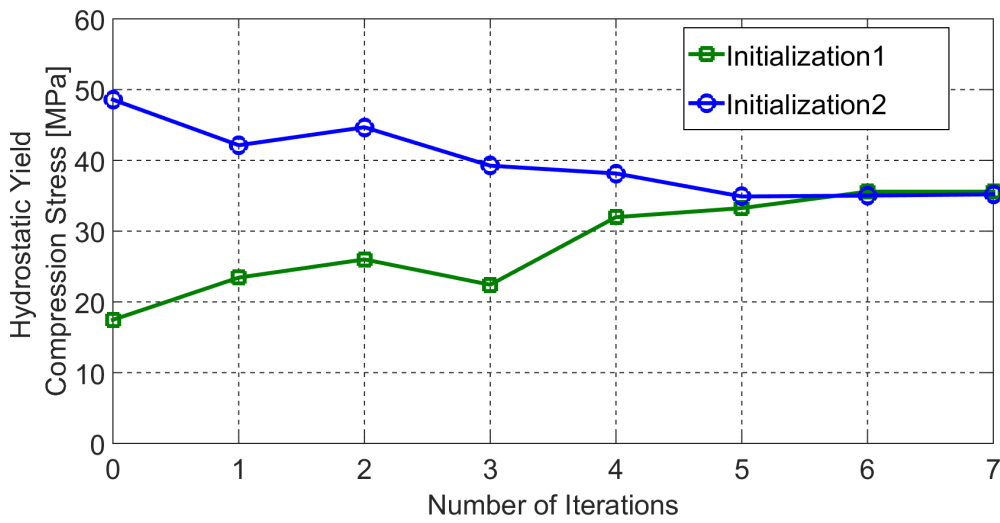


Figure 5.47. Convergence plot of hydrostatic yield compression stress for IA starting from 2 different initializations

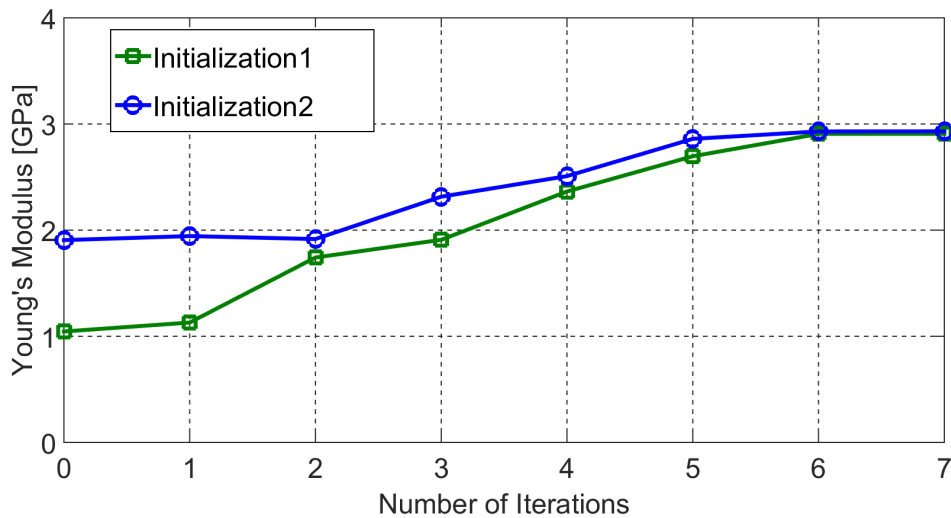


Figure 5.48. Convergence plot of Young's modulus for IA starting from 2 different initializations

Figures visualizing the compaction curves and the convergence plots, contribute to the conclusion that the designed inverse problem is well-posed. In a view of performing further checks, the results are validated by comparing parameters' values assessed through IA against the experimentally determined ones given in section 5.2. Additionally, the assessed parameters are used to simulate compaction test for complex geometries, not considered within calibration. The comparison is summarized in what follows.

5.4 Simulation of Complex Geometries Using Parameters Obtained from IA

To analyze if the assessed parameters can be used to model the compaction of alumina-graphite powder, miniaturized green bodies typically resembling industrial parts are produced and their compaction is modeled through DPC model using the obtained parameters from the developed IA procedure. The schematic representation of these different shapes can be visualized in the following figure.

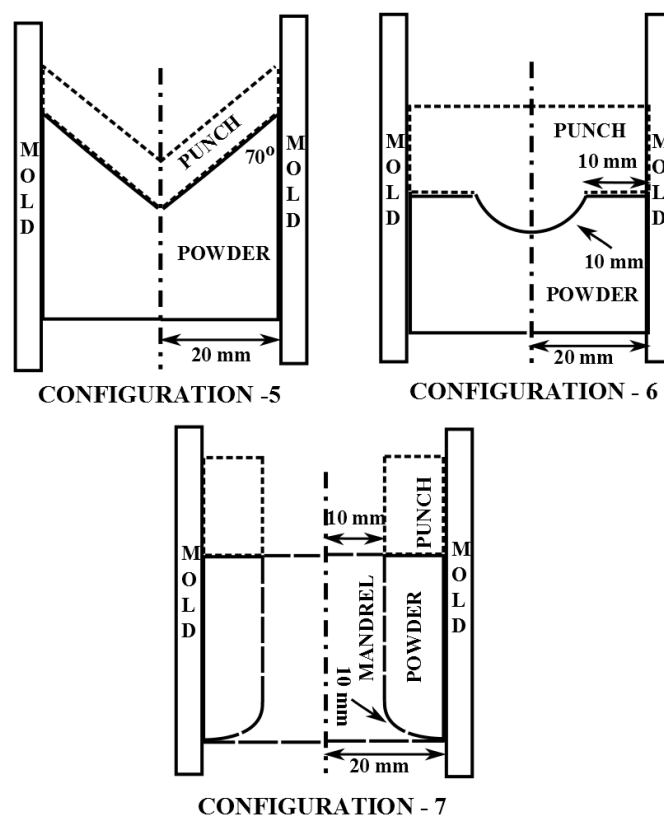


Figure 5.49. Schematic representation of configurations -5 to -7

To produce samples corresponding to the shapes given in figure 5.49, the top punches are designed as shown in figure 5.50, while a flat cylindrical punch is used as the bottom one. The mold employed for the pressing has a cylindrical opening with a diameter of 40 mm and 150 mm height, made from nitrided steel. Compaction is performed on the same "Instron" testing machine (upper part of figure 3.2). A load of 20 kN is applied to compact 60 g of alumina-graphite powder, with the top punch moving at a speed of 1.5 mm/min,

while the bottom punch is kept fixed. All the mentioned experimental conditions are kept the same for all configurations and the other relevant details are given in table 5.11. The formed samples are visualized in 5.50.

Configuration	Sample Height Initial [mm]	Sample Height Final [mm]	Relative Density Averaged
5	80.929	53.447	0.886
6	78.953	52.209	0.885
7	73.249	47.808	0.873

Table 5.11. Experimental details of the compaction tests performed to prepare samples for configurations -5 to -7



Figure 5.50. Samples made from alumina-graphite powder along with the required punches to produce configurations -5 to -7 (Left to Right)

Simulation of the compaction test for configurations -5, -6 and -7 is done in ABAQUS. All finite element models are designed as axially symmetric. The specimens for all configurations are meshed into 2480 four node fully integrated axially symmetric elements (marked as CAX4 in ABAQUS). Simulations are performed within a force control regime using a maximum load of 20 kN, corresponding to experimental details listed in table 5.11. Other simulation conditions are the same as those listed in section

3.1.2. Performed simulations led to the curves which are compared against the experimental in the figures 5.51 to 5.53.

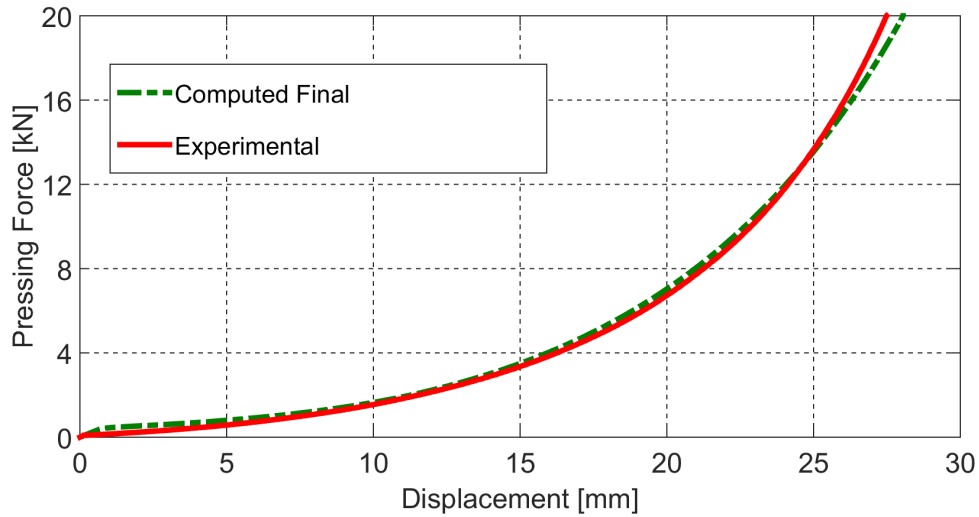


Figure 5.51. Experimental vs. final computed compaction curve for configuration-5 corresponding to parameters identified through IA employing configuration-1, -2 and -3 as inputs

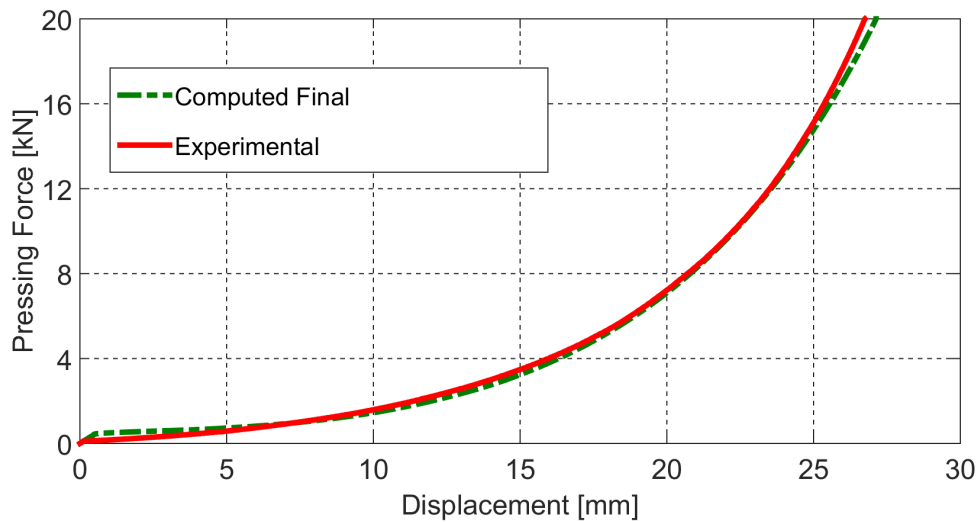


Figure 5.52. Experimental vs. final computed compaction curve for configuration-6 corresponding to parameters identified through IA employing configuration-1, -2 and -3 as inputs

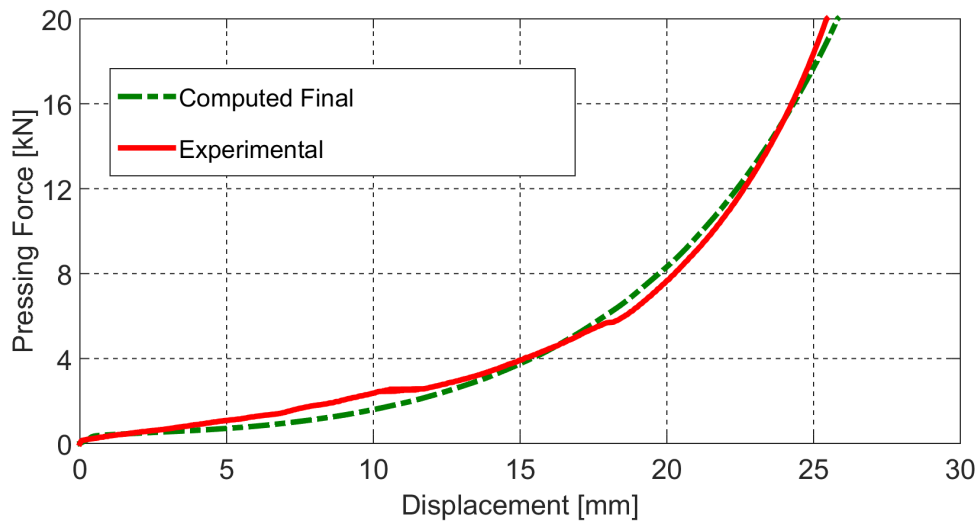


Figure 5.53. Experimental vs. final computed compaction curve for configuration-7 corresponding to parameters identified through IA employing configuration-1, -2 and -3 as inputs

A good agreement between the experimental and simulated compaction curves given in figures 5.52 to 5.53 shows that the obtained parameters through IA can be used to model compaction involving an arbitrary geometries. These results confirm that the calibration protocol relying on IA methodology offers an alternative, and a more effective route to calibrate the DPC model instead of the currently adopted methods based on destructive tests. To conclude this comparative study, values assessed through developed IA procedure are finally compared to those evaluated on the basis of a lot more time consuming destructive tests. The results are given in the following section.

5.5 Inverse Analysis Approach vs. Currently Adopted Praxis

Through the IA procedure, plastic parameters namely, cohesion (d), friction angle (β), cap eccentricity (R) and hydrostatic compression yield stress (p_b), and the two elastic parameters Young's modulus (E) and Poisson's ratio (ν) are assessed in a relative density range of 0.5-0.95. To establish reference values of parameters, four plastic parameters and Young's modulus are also evaluated from the existing methods relying on crush tests, Brazilian tests and acquiring radial stresses from the die-wall, as demonstrated in

section 5.2. From the experimental route, evolution pressure (p_a) is assessed, while via IA, p_b is evaluated. The values of p_a and p_b are related through the equation (2.6). The comparison of the parameters obtained from the two approaches are visualized in figures 5.54 to 5.59.

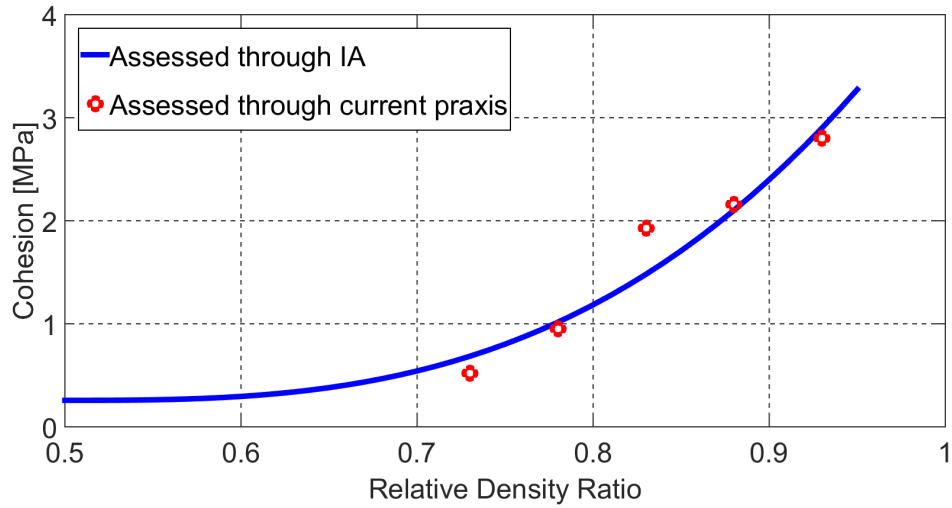


Figure 5.54. Comparison of material cohesion assessed from IA vs. experimentally determined values

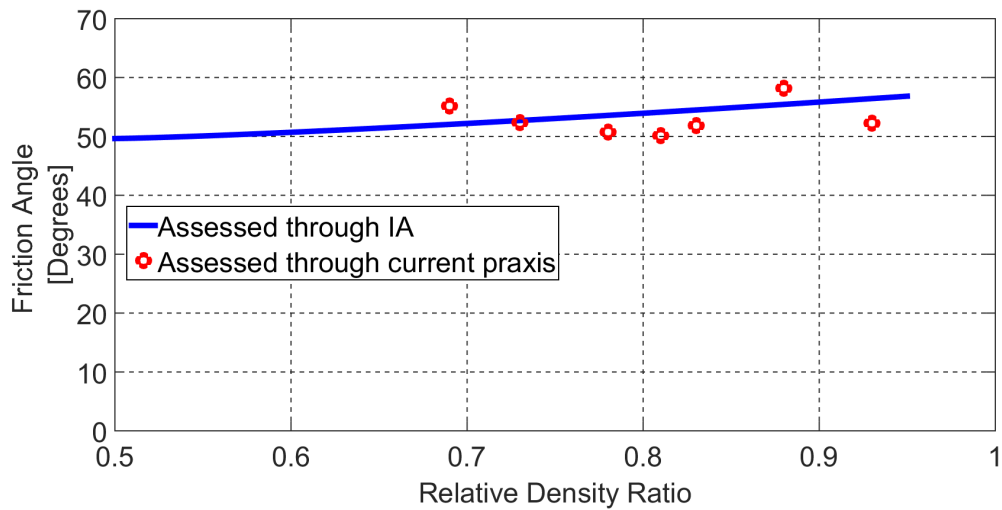


Figure 5.55. Comparison of friction angle assessed from IA vs. experimentally determined values

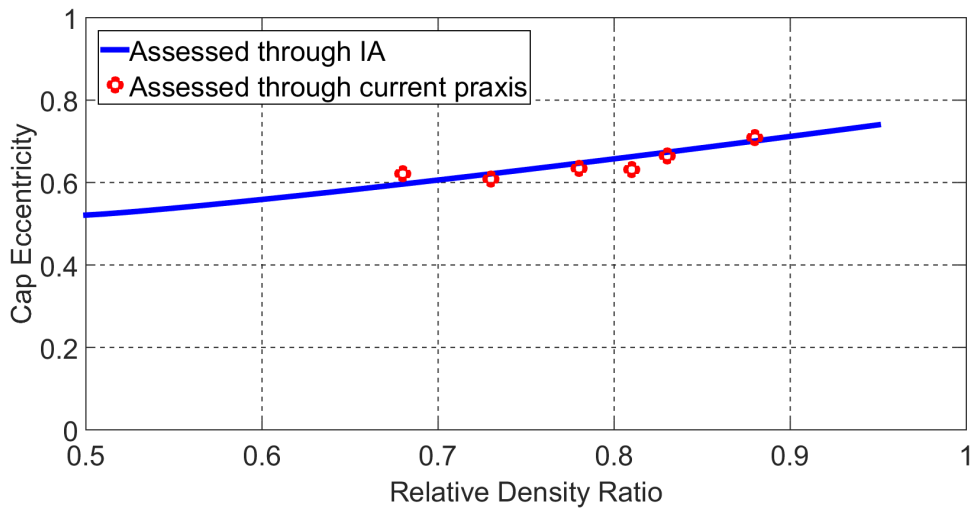


Figure 5.56. Comparison of cap eccentricity assessed from IA vs. experimentally determined values

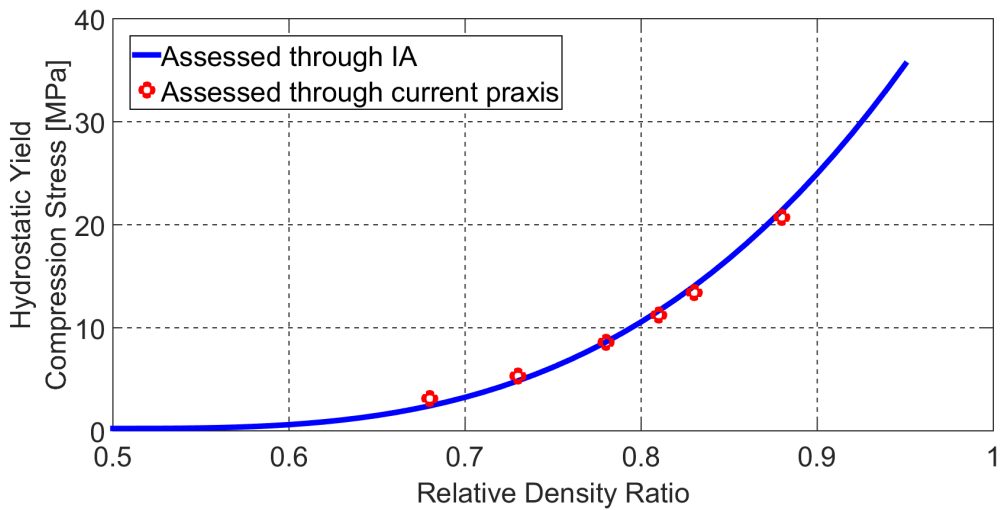


Figure 5.57. Comparison of hydrostatic yield compression stress assessed from IA vs. experimentally determined values

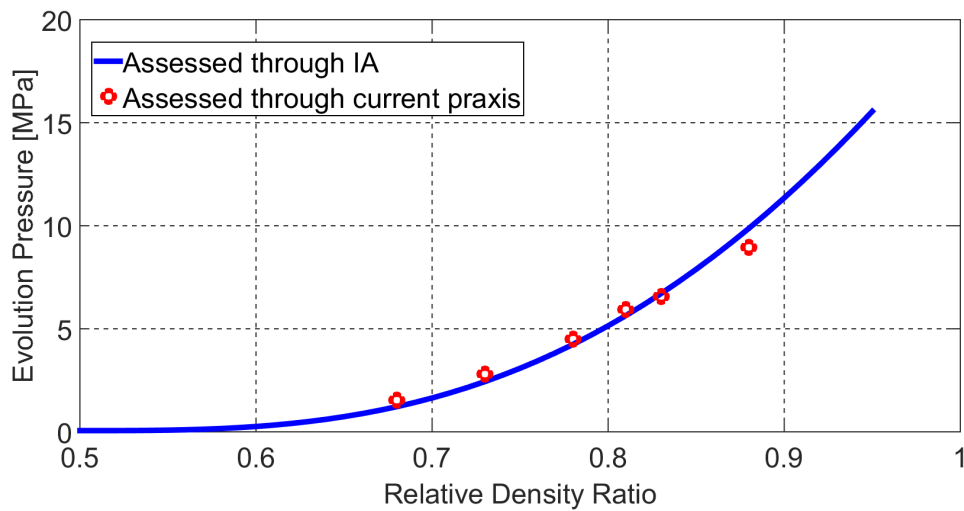


Figure 5.58. Comparison of evolution pressure assessed from IA vs. experimentally determined values

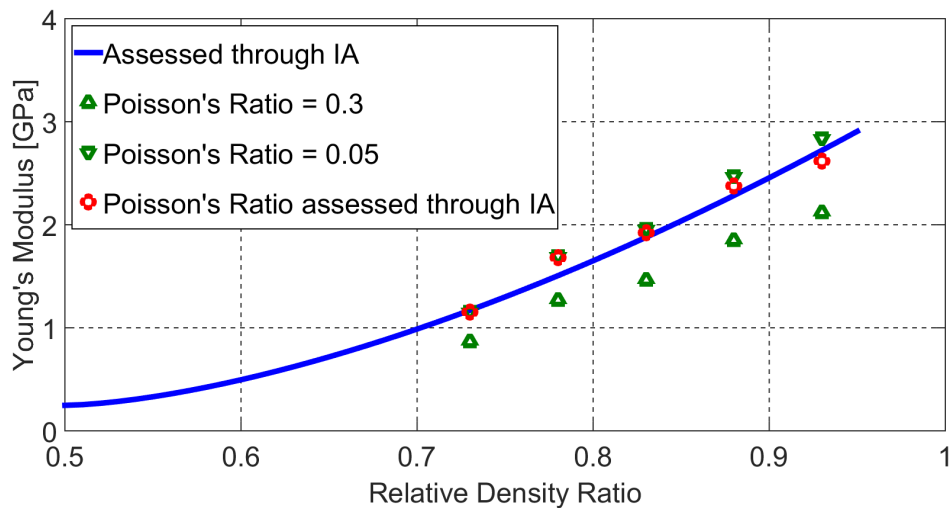


Figure 5.59. Comparison of Young's modulus assessed from IA vs. experimentally determined values

From the above figures, it can be realized that the parameters identified through IA are in a good agreement with those evaluated on the basis of the industrially adopted praxis of performing destructive tests. Obtained results contribute to the conclusion that relationship between the parameters and relative density proposed by equation (3.3) is general enough to capture both exponential trend (encountered for cohesion, for instance) as well as the linear one (for friction angle).

Furthermore, the parameters are assessed as a continuous function of relative density, within the proposed IA approach, while through the currently adopted praxis, material parameters can only be evaluated at discrete points of relative density. It is noteworthy that even though IA provides richer results, it still involves a much fewer number of experiments for calibration. This is evidenced by the fact that identifying parameters using IA approach requires only three compaction experiments (configuration -1, -2 and -3), while through current methods, assessing a parameter at only a particular relative density requires performing a minimum of four compaction and four destructive tests (i.e. at least two samples for both crush and Brazilian tests) making a total of 56 experiments for parameters estimated at only 7 relative density points in the current work.

Another advantage of IA is that it can be used to assess parameters in low relative density range, while the same is not true when the method based on destructive tests is employed. As demonstrated in section 5.2, the lowest possible relative density to produce and test green bodies turns out to be 73%. Therefore, the accuracy of assessed cohesion and friction angle at this level of relative density or lower is arguable. Within the IA approach, the parameters are determined at relative densities as low as 50%. One can even go lower to represent the initial relative density of the specimen if needed, as the parameters are evaluated using the available measurements from the compaction tests. Even though the sample cannot be ejected or tested further, the data from the compaction experiment is at the disposal to perform IA to determine the parameters in this low relative density range.

From what precedes, it can be realized that inverse analysis offers a feasible, more flexible and a very efficient approach to identify material parameters of models employed in powder compaction. Such features of IA make it a promising alternative for calibration within the industries, as opposed to the tedious and experimentally demanding approach followed currently. The developed IA protocol is summarized in what follows.

5.6 Summary of the Inverse Analysis Protocol

- Compaction experiments are performed to form green bodies of three different configurations (-1, -2 and -3) with geometries given in figures 4.1a and 4.10. From the experiment, measurable quantities are collected in the form of a digitalized pressing force vs. displacement curve along with radial stresses corresponding to two strain gages installed at different locations on the mold.
- Simulation of compaction tests corresponding to configurations -1, -2 and -3 is done by employing finite element method (here, through commercial code ABAQUS). Considered material model for simulation is the "modified" DPC model. Modification is done to include field dependencies of constitutive parameters of DPC model on relative density by using the "USDFLD" subroutine already available in ABAQUS. Once the simulation is finished, force-displacement graph along with radial stress vs. pressing force curves corresponding to the same location of the strain gages as in the experiment, are extracted.
- Residual vector is formed as the difference between experimentally measured data and their computed counter-parts. Entries to the residual vector are taken to be the displacements (100 points) from the compaction curves and the radial stresses (100 points each from bottom and middle gages) from radial stress plot corresponding to a certain level of force.
- Discrepancy function is formed as the sum of the squares of the residual vector members. Trust region algorithm based on 2-D subspace minimization is used to minimize the discrepancy function. The parameters which minimize the discrepancy function is the solution to the inverse problem and also the representative material parameters.

Chapter 6

CALIBRATION OF NOVEL MATERIAL MODEL THROUGH INVERSE ANALYSIS

Employing the Drucker-Prager Cap (DPC) model for powder compaction modeling is a reasonable strategy to test the calibration procedure based on Inverse Analysis (IA) methodology, developed within this research. This is due to the obvious advantages offered by DPC model, such as, availability in commercial codes and stable numerical implementation. Moreover, there is still a good amount of powder compositions, whose behavior under certain conditions, can be modeled accurately enough through this constitutive model.

However, the main limitation of continuum plasticity models, like DPC, is that they do not model well the transition of the powder under compaction, from its granular to fully dense state. It is experimentally observed that the powder compaction features three phases: (1) granule sliding and rearrangement; (2) granule deformation and (3) granule densification [50, 51]. It is furthermore evidenced that the cohesion of green body starts to develop only within second phase, while already during the first phase there is some growth in relative density. Clearly, models like DPC, which relate equivalent plastic strain to the relative density, fail to take into account this transition, namely to identify the level of relative density at which cohesion starts to develop. This peculiarity of powder compaction is not addressed within the currently adopted models

for simulation of compaction, hence, posing a need to develop a novel constitutive model. The task of formulating the novel model was a topic of research of the group at the University of Trento who are partners at the current (CERMAT-2) project. Description of the developed model is presented in section 6.1.

From the viewpoint of calibration, the complexities are further enhanced when such a sophisticated model is considered. The most obvious difficulty is an elevated number of parameters. Further on, the numerical implementation and testing of the novel model showed unstable simulations for certain combinations of parameters. The assessment of parameters based on the developed IA procedure so far relied on the minimization of objective function which is achieved by using Trust Region Algorithm (TRA) throughout this research. Employing TRA involves calculations of first derivatives which are approximated by finite forward differences. Such feature of TRA makes the use of developed IA procedure rather difficult when combined with an unstable model, exhibiting convergence difficulties for certain combinations of parameters.

As a remedy to solve the minimization problem, Genetic Algorithms (GA) can be used which are capable of finding a global minimum for a discontinuous function even with high non-convexity. However, the number of function evaluations when employing GA is considerably elevated, usually larger by one to two orders of magnitude as compared to TRA. Given that the function evaluation here involves a Finite Element (FE) simulations, minimization technique based on GA is rendered unfeasible for practical purposes. The only way in which this approach can be made applicable is to develop a faster alternative to replace the FE simulations.

Potential replacement of Finite Element Model (FEM) is offered by an appropriately designed Reduced Basis Model (RBM). Such techniques are relying on “correlation” of numerically computed data, in order to design a subspace with significantly reduced dimensionality. This approach offers a substantial reduction of computing time preserving almost the same accuracy as that of the original model by extracting the most meaningful information from it. Different kinds of RBM have already been employed in various fields of science and engineering, such as transient thermal analysis [6], damage detection in structures [56], human face recognition methods [60], analysis of turbulent flows [5] and many others [34, 39, 62]. In particular, the work of Buljak and Maier [16]

is a typical example of the application of RBM in structural mechanics. In that research, material characterization based on instrumented indentation tests was done by performing numerical simulations of the experiment through RBM, instead of computationally expensive FEM simulations.

In the present research, implementation of RBM for the acceleration of numerical simulations of powder compaction is studied. To assess the parameters of the novel model, IA procedure is designed, relying on the combination of GA and RBM. In what follows, an overview of the novel model is given, preceded by a brief description on genetic algorithm and reduced basis model employed for the acceleration of non-linear simulations.

6.1 Novel Constitutive Model for Powder Compaction

During powder compaction, material transforms from a loose to a dense state. Modeling powder compaction accurately, through continuum plasticity, requires the yield criterion to take into account the evolution of a material undergoing compaction from granular to dense state. Most of the authors are using the modified Drucker-Prager Cap (DPC) yield criteria to this purpose [28, 70], while some have also employed modified Cam Clay (CC) criterion [24]. The modified DPC and CC criterion model the powder compaction fairly well, however, these yield functions fail to provide any information about the particular point at which the material is no longer granular and starts developing cohesion. To address this shortcoming, yield function formulated by Bigoni and Piccoloroaz [7] can be used.

The model presented here is based on Bigoni-Piccoloroaz (BP) yield function, two micro-mechanical hardening laws and elasto-plastic coupling. Short description of these different ingredients is given in what follows.

6.1.1 Bigoni-Piccolroaz Yield Function

BP yield criterion has an important capability to change the shape of yield surface. In the present context, this feature is exploited to describe the transition between two distinctly different states of a material undergoing compaction [51]. Figure 6.1 visualizes the evolution of BP yield surface as the compaction progresses. Here, the breakpoint pressure (p_{cb}) marks the onset of 2nd phase of compaction, namely, granule deformation. Cohesion is almost negligible throughout the 1st phase and substantially starts to increase in the 2nd phase, as seen from figure 6.1. Density of the green body also grows rapidly during the 2nd phase, which is observed by the steep increase in slope in figure 6.2.

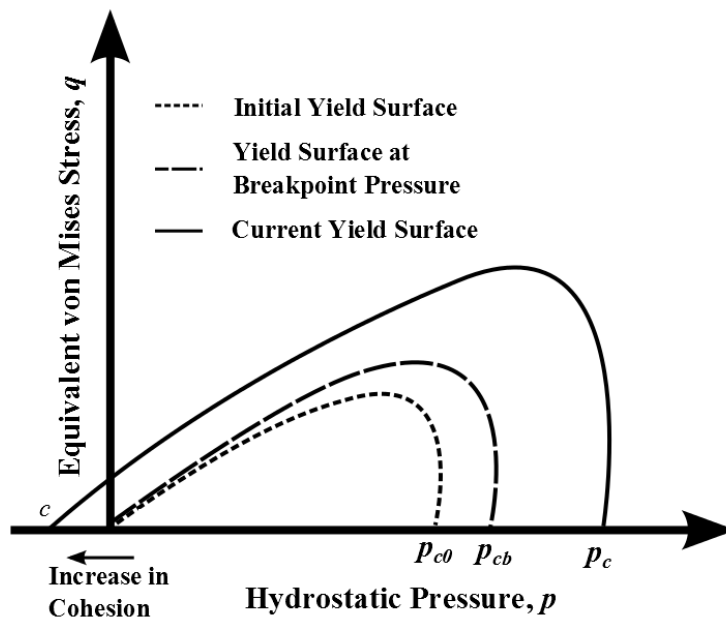


Figure 6.1. Bigoni-Piccolroaz yield surface at three different instances during compaction

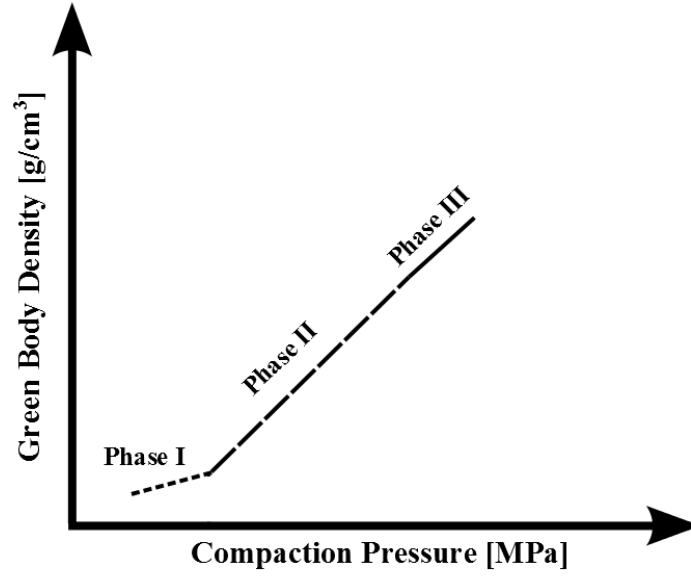


Figure 6.2. Semi logarithmic plot of compact density vs. applied pressure

Mathematical formulation of Bigoni-Piccolroaz yield function is given as:

$$F(\boldsymbol{\sigma}, M, p_c, c) = f(p, M, p_c, c) + \frac{q}{g(\theta)} \quad (6.1)$$

where, $f(p, M, p_c, c)$ is the meridian function describing the pressure sensitivity part of the function, while $(q/g(\theta))$ is the deviatoric function defining the Lode dependence of yielding. Here, $\boldsymbol{\sigma}$ is the stress tensor, p is the hydrostatic pressure, M is the pressure sensitivity parameter of the material, p_c is the hardening parameter, c is the cohesion, q is the equivalent von Mises stress and θ is the Lode's angle.

Analytical expression of $f(p, M, p_c, c)$ reads:

$$f(p, M, p_c, c) = \begin{cases} -Mp_c \sqrt{[\varphi - \varphi^m] [2(1 - \alpha)\varphi + \alpha]}, & \text{if } \varphi \in [0, 1] \\ \infty, & \text{otherwise} \end{cases} \quad (6.2)$$

here, α and m are shape factors of meridian section of the yield surface, while φ and M respectively, are defined as:

$$\varphi = \frac{p + c}{p_c + c} \quad (6.3)$$

$$M = M_0 + \frac{k_1}{\delta} \frac{(1 + \delta J_2^p)^{n_1-1} - 1}{(n_1 - 1)(1 + \delta J_2^p)^{n_1-1}} \quad (6.4)$$

where, M_0 is the initial pressure sensitivity parameter, k_1 , δ and n_1 are the parameters defining the transition of M during the compaction and J_2^p is the second invariant of the deviatoric strain.

The $g(\theta)$ part of the deviatoric function is expressed as:

$$\frac{1}{g(\theta)} = \cos \left[\frac{\beta\pi}{6} - \frac{1}{3} \cos^{-1} (\gamma \cos 3\theta) \right] \quad (6.5)$$

where, β and γ are shape factors of deviatoric section of the yield surface and Lode's angle is defined in the form below:

$$\theta = \frac{1}{3} \cos^{-1} \left[\frac{3\sqrt{3}}{2} \frac{J_3}{J_2^{3/2}} \right] \quad (6.6)$$

The plastic flow rule used in combination with the BP yield function can take both, associative and non-associative form, depending on the value of parameter η , helping to model behavior of different types of powders [51]. The analytical formulation of the flow rule is given as:

$$\dot{\epsilon}^p = \dot{\lambda} \left[\mathbf{Q} - \frac{1}{3} \eta (1 - \varphi) (\text{Tr } \mathbf{Q}) \mathbf{I} \right], \quad \text{and} \quad \mathbf{Q} = \frac{\partial F}{\partial \boldsymbol{\sigma}} \quad (6.7)$$

here, $\text{Tr } \mathbf{Q}$ is the trace of matrix \mathbf{Q} , $\dot{\epsilon}^p$ is the plastic strain rate tensor, $\dot{\lambda}$ is the plastic flow multiplier and \mathbf{I} is the identity matrix. For $\eta=0$ the flow is associative, while for other values of η it is non-associative.

The parameters needed to be quantified in order to define this plasticity model are: cohesion (c), hardening (p_c), pressure sensitivity parameters (M_0 , k_1 , δ and n_1), plastic flow (η), meridian shape factor (α and m), deviatoric shape factor (β and γ). Parameters controlling the shape of BP yield surface, namely: α , m and γ are evaluated for both initial (α_1 , m_1 and γ_1) and final state (α_2 , m_2 and γ_2) of the powder, while β is identified as a single constant assumed not to change during compaction. Initial hardening parameter (p_{c0}) is also needed to describe the phase (1) of the powder compaction. The increase in cohesion and evolution of parameter p_c with plastic deformation is dealt under hardening,

which is given in what follows. For more detailed description of BP yield function and developed plasticity model for powder compaction, refer to [7].

6.1.2 Description of Hardening Rules

Two hardening rules are defined by the dependency of hardening parameter (p_c) and cohesion (c) on the volumetric plastic strain (e_v^p). The relation between p_c and e_v^p is determined by employing Cooper-Eaton hardening law which describes the densification behavior of the material under isotropic compression. Cooper-Eaton formula takes into account first two phases of the compaction through a double exponential law as given in equation (6.8), where the exponents a_1 and A_1 correspond to the 1st phase, while the exponents a_2 and A_2 represent the 2nd phase. Constants a_1 and a_2 denote the increment of void ratio (e_0) that would be achieved at infinite pressure by each of the two mechanisms of compaction. Coefficients A_1 and A_2 are the values of pressure at which the 1st and the 2nd phase of compaction become dominant, respectively.

$$e_v^p = -\frac{e_0}{1 + e_0} \left\{ a_1 \exp\left(-\frac{A_1}{p_c}\right) + a_2 \exp\left(-\frac{A_2}{p_c}\right) \right\} \quad (6.8)$$

The second hardening rule models the growth in cohesion with progressing compaction. Given that the relation between p_c and e_v^p is established, increase in cohesion can be defined as a function of hardening parameter (p_c) by the formula given as:

$$c = c_\infty [1 - \exp(-\Gamma_c \langle p_c - p_{cb} \rangle)] \quad (6.9)$$

where, c_∞ is the limit value of cohesion after substantial plastic deformation, p_{cb} is the breakpoint pressure marking the onset of phase (2) of compaction and Γ_c controls the growth of cohesion from initial to final state of the powder. The Macaulay operator " $\langle \rangle$ " implies that value contained in it is non-negative, since the cohesion is null before p_{cb} is reached.

Parameters needed to characterize the two hardening rules are: $a_1, A_1, a_2, A_2, c_\infty, p_{cb}$ and Γ_c . Definition of hardening rules and the BP yield function constitute the plastic part of novel model, while the formulation of elasticity law is given in what follows.

6.1.3 Elastic Response and Elasto-Plastic Coupling

The elastic response of the powder becomes stiffer as the compaction progresses, as evidenced in figure 1.2. In the initial phase of compaction, the granular material obeys the non-linear elastic law, while compacted powder behaves like a dense solid following the linear elastic law [49]. In order to take these details into account, elastic rule is defined such that: a) it incorporates transition from non-linear elastic law to a linear one (i.e granular to solid) during the compaction and b) elasto-plastic coupling is defined in order to include the dependence of elastic properties on the plastic deformation.

The mathematical formulation of the elastic law is given as:

$$\boldsymbol{\sigma}(\boldsymbol{\epsilon}_e, e_v^p) = \left\{ -\frac{2}{3}\mu e_v^e + c + (p_0 + c) \left[\left(d(e_v^p) - \frac{1}{d(e_v^p)} \right) \frac{(1 + e_0)e_v^e}{\kappa} - \exp \left(-\frac{(1 + e_0)e_v^e}{d(e_v^p)^{1/n}\kappa} \right) \right] \right\} \mathbf{I} + 2\mu\boldsymbol{\epsilon}^e \quad (6.10)$$

where,

$$d = 1 + \Gamma_E \langle p_c - p_{cb} \rangle, \quad \mu(d) = \mu_1 + c \left(d - \frac{1}{d} \right) \mu_2 \quad (6.11)$$

In equation (6.10), $\boldsymbol{\epsilon}_e$ is the elastic strain tensor, e_v^e and e_v^p are volumetric elastic and plastic strains respectively, μ is the shear modulus such that μ_1 and μ_2 correspond to initial (granular) and final (dense) state of the powder respectively, p_0 is the initial confinement pressure (i.e. pre-consolidation pressure before compaction starts), d is elastic transition parameter, n is the constant defining the exponential decay of d , e_0 is the initial void ratio, κ is the bulk modulus, while Γ_E in formula (6.11) controls how quickly the elastic response changes from granular to compacted material. From the above relations, the elastic law of the granular material can be recovered by setting $d=1$. For detailed explanations, see [51].

In the numerical implementation of the model, I Lamé parameter (λ) is used instead of bulk modulus, while shear modulus represents I Lamé constant (μ). The parameters required to model the elastic behavior are: Lamé's parameter I and II corresponding to the initial (λ_1 and μ_1) and final (λ_2 and μ_2) state of the powder respectively, initial void

ratio (e_0), pre-consolidation pressure (p_0), exponential decay term n and parameter Γ_E controlling the change in the elastic behaviour.

From the outline of the novel model presented here, a total of 28 parameters (13 for yield function, 7 for hardening, 8 for the elasticity) are needed to define the model. Out of these 28, two elastic parameters, namely initial void ratio (e_0) and exponential decay term (n) are assumed as *a priori* known constants and are not subjected to the identification. The remaining model parameters, which are given in table 6.1, are subjected to the identification through inverse analysis procedure designed by combining the concepts of genetic algorithms and reduced basis modeling, outlined in the following sections.

Table 6.1. Parameters defining the novel constitutive model

Serial Number	Parameter	Units	Parameter Description
Yield Surface Parameters			
1.	p_{c0}	[MPa]	<i>Initial Hardening</i>
2.	M_0	-	<i>Pressure Sensitivity</i>
3.	k_1	-	
4.	δ_1	-	
5.	n_1	-	<i>Meridian Shape Parameters</i>
6.	m_1	[MPa]	
7.	m_2	-	
8.	α_1	-	
9.	α_2	-	<i>Deviatoric Shape Parameters</i>
10.	β	-	
11.	γ_1	-	
12.	γ_2	[MPa]	<i>Plastic flow</i>
13.	η	-	
Hardening Parameters			
14.	a_1	-	<i>Cooper-Eaton Hardening</i>
15.	λ_1	[MPa]	
16.	a_2	-	
17.	λ_2	[MPa]	
18.	p_{cb}	[MPa]	<i>Cohesion Related Hardening</i>
19.	c_∞	[MPa]	
20.	Γ_c	[MPa ⁻¹]	
Elastic Parameters			
21.	\mathcal{A}_1	[MPa]	<i>Lame's Constants</i>
22.	μ_1	[MPa]	
23.	\mathcal{A}_2	[MPa]	
24.	μ_2	[MPa]	
25.	Γ_F	[MPa ⁻¹]	<i>Elasto-plastic Coupling</i>
26.	p_0	[MPa]	

6.2 Genetic Algorithms

Genetic Algorithms (GA) represent a methodology to solve both constrained and unconstrained minimization problems, iteratively. In the present context, the solution of the minimization problem are the constitutive parameters of the novel material model. Within the GA jargon, these candidate solutions (i.e. different parameter sets of novel model) are referred to as members of the "population". During each iteration ("generation" in GA terminology), the population is modified by the process of "natural"

selection. Through this process (sometimes also referred as "selection rules"), members of the current population are used to produce three different types of "kids", namely, "elite", "cross-over" and "mutation" kids, to form the next generation. Over subsequent generations, the population "evolves" towards an optimal solution. The working principle of GA is given in what follows.

- At the beginning of the minimization, the initial population is formed by randomly generated members (i.e. parameter vectors), which represent different points in the parameter space. The domain is defined by an "expert" such that it correctly limits the values of each of the sought parameter.
- The value of the objective function (referred as "fitness" function in GA jargon) is calculated for the members of the current generation. This step is computationally most demanding as each evaluation of the objective function represents solving of the forward problem, which in the present context, involves finite element simulations.
- Once the values of the objective function are assessed, they are sorted in an ascending order. Further on, the current population is modified through the natural selection process, to form a new generation by creating kids, by employing the following operations:
 - ★ Selection of the elite kids: These are the members with best (i.e. smallest) value of the objective function within the current generation. They are directly passed to the next generation without any modification, hence, preserving the members with currently the best value of fitness function. Usually, the elite kids amount 2-5% of the population size.
 - ★ Forming cross-over kids: A certain number of members are chosen as "parents" which contribute their "genes" (i.e. parameter values) to create the cross-over kids. The selection of the parents can be random, however, the most common criterion is to consider the members from best to intermediate values of the fitness function to be treated as the parents. Usually 50%-70% of the population is used as the parents, which are then randomly combined to form "couples". Obviously with such an implementation, repetition of the same parent in different couples is possible. After the couples are formed, the crossing-over of the genes of each

parent is performed to produce cross-over kids. A straightforward cross-over rule which is also adopted in the present work, generates random vector of the same size as the parameter vector, with only zeroes and ones as entries. Applying this rule to the previously formed couple, one cross-over kid is constructed on the basis of this random vector such that entry 1 means taking the corresponding parameter value from the first parent, while entry 0 means taking it from the second one. As an example, crossing over two parents, $\mathbf{X}=[X_1, X_2, X_3, X_4]^T$ and $\mathbf{Y}=[Y_1, Y_2, Y_3, Y_4]^T$ with the random vector $\mathbf{R}=[1, 1, 0, 1]^T$, results in $[X_1, X_2, Y_3, X_4]^T$. The number of cross-over kids is controlled by the "cross-over ratio", which is the fraction between cross-over kids and total remaining members after the elite are passed to the next generation. Clearly, total number of members per generation remains unchanged.

- ★ Forming mutation kids: These are created by applying mutation (i.e. random changes) to all the parameters of members remaining in the population after the elite and cross-over kids are formed. The remaining members in the population represent the worst ones (in terms of the objective function values). Therefore, wasting these members by applying a fully random modification to create new ones is a reasonable strategy, since, it may produce better members. The amount of mutation that the parameters are subjected to is governed by a factor called "mutation range". This factor plays a very important role by preventing GA to be trapped in a local minima. A simple one-dimensional example to demonstrate this is given in figure 6.3. It can be clearly visualized from the figure, that with a small amount of mutation the algorithm will not have the capability to jump out from the local minimum. In the present work, the parameters are all normalized within the range of zero (lower bound) and one (upper bound), and the mutation used is equal to ± 0.1 to ± 0.4 , specified in more details in section 6.5.

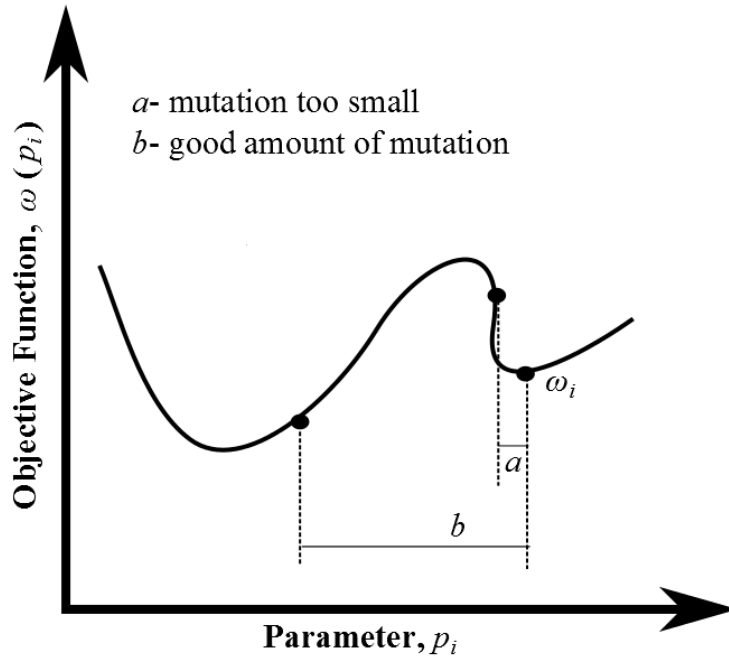


Figure 6.3. The influence of amount of mutation to demonstrate capability of algorithm to avoid trapping in local minima

- Using this procedure, a new generation is formed, replacing the old one. The process iteratively continues until the stopping criteria are met. Two most commonly used rules for terminating the minimization, adopted also in this study are: a) when a maximum number of generations is met, or, b) when the number of "stalling" generations reaches a previously prescribed value, which represents the number of consecutive generations with no improvement in the objective function value. For more detailed explanation of GA, refer to [13, 42].

From the outline of GA presented above, it can be realized that this algorithm is a zero-order, since it computes only the value of the objective function, and not its derivatives. Such feature plays a very important role in minimizing discontinuous, non-differentiable or highly nonlinear objective functions. However, this aspect of GA comes at the expense of increased computational cost. The total number of objective function evaluations (and therefore, FEM simulations in the present context) is equal to the product between the size of the population and the total number of generations required within the minimization procedure. Given that the total number of parameters of the novel model to be evaluated is 26, from statistical reasons it is expected to have at least about 150-200 members in each population, while the number of generations could

be between 100 and 150. Clearly, the total number of FEM simulations is at least two orders of magnitude larger than what is needed when traditional derivative based algorithms (like, trust region) are employed. It is not practically possible to run such a huge amount of simulations on a regular desktop computer as total time needed will be measured by months. This contributes to the conclusion that the only viable option to use GA for characterizing the novel model is to reduce significantly the computational time required for FEM simulations. To this purpose, reduced basis modeling appears to be a promising prospective. The description of the adopted form of reduced basis model is outlined in what follows.

6.3 Reduced Basis Model

Reduced Basis Model (RBM) adopted in this study, is a projection based technique, relying on the Proper Orthogonal Decomposition (POD). This is motivated by the fact that using a POD basis gives the best approximation (or maximum accuracy), as it is the most efficient way to capture the dominant components of a high dimensional process, through a fairly small number of directions [18].

In the present work, RBM is designed to construct a low order approximation of numerical simulations, therefore, only the discrete POD theory is presented. To understand this better, let us suppose a finite element simulation of compaction test is performed within force control regime, with some quantities of interest collected in a resulting vector. Constitutive description for the simulation is defined through the novel material model, that depends on some parameters, collected in a vector \mathbf{p} . The recorded output from the simulation is a compaction curve, which is stored in a vector $\mathbf{u}_i = [u_1, u_2, \dots, u_Y]^T$, whose entries are displacement of the same point (on the punch) corresponding to Y force levels from zero to maximum specified force. Assuming that X different simulations are performed by keeping all the conditions the same and only changing the parameters of the material model, the resulting outputs of the simulations, can be projected in a new coordinate system, through a linear combination of some vectors as:

$$\mathbf{u}_i(\mathbf{p}) = \sum_{j=1}^X a_j^i \cdot \boldsymbol{\psi}_j(\mathbf{p}), j = 1, 2 \dots Y \quad (6.12)$$

Here, $\boldsymbol{\psi}_i$ are the directions in the new coordinate system and a_j^i are the unknown coefficients (or "amplitudes") of the expansion, whose values are computed through a minimization process in the least square sense such that:

$$\min \left\| \mathbf{u}(\mathbf{p}) - \sum_{i=1}^X a_i \cdot \boldsymbol{\psi}_i(\mathbf{p}) \right\| \quad (6.13)$$

where, $\|\cdot\|$ is the L_2 norm.

Within the POD theory, $\mathbf{u}(\mathbf{p})$ in equation (6.12) represents a "snapshot" which is some output of a certain system corresponding to some input parameter \mathbf{p} . A set of X different snapshots is stored in a snapshot matrix $\mathbf{U}=[\mathbf{u}_1, \mathbf{u}_2, \dots, \mathbf{u}_X]$, such that each column corresponds to different input parameters collected in matrix $\mathbf{P}=[\mathbf{p}_1, \mathbf{p}_2, \dots, \mathbf{p}_X]$. Therefore, in the present context, a snapshot matrix (size Y by X) represents a collection of X different vectors that are recording displacements from the compaction test, generated by changing the parameters entering the novel model, while keeping all other simulation conditions fixed. Using relation (6.12), snapshots in the matrix form can be expressed in a new coordinate system as:

$$\mathbf{U} = \boldsymbol{\Psi} \mathbf{A} \quad (6.14)$$

In the above equation, matrix $\boldsymbol{\Psi} = [\boldsymbol{\psi}_1, \boldsymbol{\psi}_2 \dots \boldsymbol{\psi}_X]$ contains all the directions within the new coordinate system and matrix \mathbf{A} contains the corresponding amplitudes. The choice of directions $\boldsymbol{\psi}$ to construct the basis for \mathbf{U} is arbitrary and different set of amplitudes correspond to each selected basis. However, using directions which are orthogonal to each other, as given in equation (6.15), is advantageous, since, the determination of coefficients becomes a simple task. This can be realized from the fact that due to orthogonality of vectors, the amplitude a_j^i will depend only on the vector $\boldsymbol{\psi}_i$ and not on the others, while if the chosen basis is non orthogonal, the evaluation of amplitudes would involve solving a set of linear equations.

$$\boldsymbol{\psi}_{s_1}(\mathbf{p}) \cdot \boldsymbol{\psi}_{s_2}(\mathbf{p}) = \begin{cases} 1, & \text{if } s_1 = s_2 \\ 0, & \text{if } s_1 \neq s_k \end{cases} \quad (6.15)$$

Clearly, if all the directions in the new coordinate system are taken to represent the snapshot matrix, no error is introduced and the quantities of each snapshot are merely projected in a different reference system. Given that the goal here is to reduce the dimensionality of the snapshot matrix and still maintain reasonable accuracy of its approximation, the next step is to construct an "optimal" orthogonal basis. Optimal here implies that a sequence of specially ordered orthonormal directions $\boldsymbol{\Psi} = [\boldsymbol{\psi}_1, \boldsymbol{\psi}_2 \dots \boldsymbol{\psi}_i]$ needs to be determined such that the first two of these directions ($i=2$) gives the best possible two-term approximation, the first three the best possible three term approximation and so on. Once found, they provide a favorable basis for reduction of the dimensionality of vectors (i.e. snapshots) in set, due to their optimal property, guaranteeing that there cannot be any other basis that can have better approximation for any selected number of reduced components.

The construction of optimal orthogonal basis can be achieved through Principal Component Analysis (PCA) [57]. Procedure based on PCA uses an orthogonal transformation to convert a set of observations of possibly correlated variables into a set of values of linearly uncorrelated variables, called Principal Components (PC). This transformation is defined in such a way that the first PC (direction) contains most of the variation in the data, and each succeeding direction has the highest variation possible under the constraint that it is orthogonal to the preceding directions. Therefore, the dimensionality of the original space of variables is reduced by keeping just the first few PCs, still preserving a good accuracy of the approximation.

In the present context, it is reasonable to expect that there will be a strong correlation between the snapshots since they represent the outputs of the same system where just some parameters are changed. The expected correlation suggests that previously presented POD theory can be interpreted through PCA, making it effective to apply on the snapshot matrix, allowing to construct a new orthogonal basis in which the dimensionality can be drastically cut-down. The sequence of steps to generate the POD basis for the snapshot matrix is the following:

- Find a direction in which the summations of all projections of the snapshots gives a maximum.
- Construct a direction orthogonal to the previous one and choose the one giving maximum projection of all the snapshots.
- Repeat this process until last direction is found.

To use the above mentioned steps to construct a POD basis, one needs to solve the eigenvalue problem, on positive semi-definite matrix $\mathbf{S} = \mathbf{U}\mathbf{U}^T$. It is evidenced in the literature [13, 18, 48] that for vectors in set \mathbf{U} , the POD directions are represented by eigenvectors sorted in descending order of corresponding eigenvalues. To reduce the dimensionality of the snapshot matrix, first few directions K (with $K \ll X$) are kept which have the largest projection of all the snapshots. This decision can be made based on the eigenvalues, which are sorted in descending order. The usual practice is to keep the first eigenvalues whose summation is 99.9% of the total sum of the eigenvalues. Thus, the corresponding eigenvectors represent the directions which contain the majority of "information" kept in the snapshot matrix. Therefore, by truncating the new basis to only a small number of axes, a significant reduction of dimensionality is achieved by preserving high accuracy of the approximation. The projection of snapshot matrix to a reduced space is given as:

$$\mathbf{U} \cong \bar{\Psi} \bar{\mathbf{A}} \quad (6.16)$$

and each individual snapshot can be written as:

$$\mathbf{u}_i(\mathbf{p}) \cong \bar{\Psi} \bar{\mathbf{a}}_i(\mathbf{p}), \quad i = 1, 2 \dots X \quad (6.17)$$

where, $\bar{\mathbf{A}}$ (size K by X) and $\bar{\Psi} = [\psi_1, \psi_2 \dots \psi_K]$ (size Y by K , such that $K \ll X$) are the truncated amplitude and direction matrices respectively. The whole snapshot matrix can be reconstructed just by the multiplication of the two matrices given by equation (6.16).

In what precedes, it is shown how the POD theory can be applied to construct the low order approximation of a Finite Element (FE) simulations. However, this "light" model obviously can give the responses of the simulations of compaction experiment, only for a

discrete number of parameter combinations of the novel model: those that were previously used to generate the snapshot matrix. Since the goal here is to use inverse analyses to evaluate parameters of the novel model itself, the procedure relies on performing multiple FE simulations corresponding to different input parameters within a range suggested by an "expert". Therefore, the required reduced basis model needs to be capable of computing an approximate response of the system for any arbitrary combination of parameters within that range. To this purpose, the existing data within the snapshot matrix in form of vectors collecting displacements for discrete parameter combinations, need to be interpolated and it is achieved through Radial Basis Functions (RBF) described in what follows. For more details on POD, reader is referred to [13, 57].

6.4 POD-RBF Model for Direct Analysis

Radial Basis Functions (RBF) are frequently used to construct an approximation of a certain multi-variable function by interpolation between the existing data [6, 13]. In the present context, RBF are applied to form one continuous function: to compute the numerical response of compaction experiment for any arbitrary parameter combination of the novel model, within a certain range. To achieve this, RBF utilize the already available values of snapshots computed for some discrete parameter combinations, and interpolates these responses in such a way that the output is a snapshot defined over the whole domain of parameters. A brief explanation of the methodology employed for this interpolation is presented here.

Under the assumption that amplitude vector $\bar{\mathbf{a}}$ given in equation (6.17) can be written as the linear combination of some vectors, it can be expressed as:

$$\bar{\mathbf{a}}_i(\mathbf{p}) = \sum_{i=1}^X b_i^j \cdot \mathbf{g}_i(\mathbf{p}), j = 1.2\dots K \quad (6.18)$$

In the above equation, b_i^j are the coefficients of the interpolation and the entries to the vector \mathbf{g} are functions of sought parameters written as:

$$\mathbf{g}(\mathbf{p}) = \begin{bmatrix} g_1(\mathbf{p} - \mathbf{p}_1) \\ g_2(\mathbf{p} - \mathbf{p}_2) \\ \vdots \\ g_X(\mathbf{p} - \mathbf{p}_X) \end{bmatrix} \quad (6.19)$$

The choice of interpolation function g_i in formula (6.18) is arbitrary and here, radial basis functions are chosen to represent them. There are a few types of RBF and it can be found in [13]. In the current work, an inverse multi-quadric function is selected which reads:

$$g_i(\mathbf{p} - \mathbf{p}_i) = \frac{1}{\sqrt{\|\mathbf{p} - \mathbf{p}_i\| + 1}} \quad (6.20)$$

where, $\|\cdot\|$ is the L_2 norm.

After defining the functions g_i , the unknown coefficients b_i^j need to be determined. This can be done by making the equation (6.18) exact for all the snapshots. This leads to the following formulation:

$$\bar{\mathbf{A}} = \mathbf{B} \cdot \mathbf{G} \quad (6.21)$$

such that,

$$\mathbf{B} = \begin{bmatrix} b_1^1 & b_2^1 & \dots & b_X^1 \\ b_1^2 & b_2^2 & \dots & b_X^2 \\ \vdots & \vdots & \ddots & \vdots \\ b_1^K & b_2^K & \dots & b_X^K \end{bmatrix} \quad \mathbf{G} = \begin{bmatrix} g_1(\mathbf{p}_1 - \mathbf{p}_1) & g_1(\mathbf{p}_2 - \mathbf{p}_1) & \dots & g_1(\mathbf{p}_X - \mathbf{p}_1) \\ g_2(\mathbf{p}_1 - \mathbf{p}_2) & g_2(\mathbf{p}_2 - \mathbf{p}_2) & \dots & g_2(\mathbf{p}_X - \mathbf{p}_2) \\ \vdots & \vdots & \ddots & \vdots \\ g_X(\mathbf{p}_1 - \mathbf{p}_X) & g_X(\mathbf{p}_2 - \mathbf{p}_X) & \dots & g_X(\mathbf{p}_X - \mathbf{p}_X) \end{bmatrix} \quad (6.22)$$

where, $\bar{\mathbf{A}}$ is the amplitude matrix, \mathbf{G} (size X by X) is a matrix comprising of the values of the interpolation functions in all points in the parameter space used to generate snapshot matrix, while matrix \mathbf{B} (size K by X) stores the coefficients of interpolation. Here, X is

number of available snapshots and K is the number of directions kept in the truncated POD basis. It should be noted that before construction of matrix \mathbf{G} , parameters should be normalized such that all entries are in dimensionless range between 0 and 1. This is done in order to avoid numerical problems as parameters can differ by orders of magnitude (for instance, Lamé's constants and the hardening parameter in the novel model).

After computing matrix \mathbf{B} , the snapshot \mathbf{u} for any arbitrary parameter vector \mathbf{p} can be approximated through the relations (6.17) and (6.18), which gives the analytical formulation for snapshot approximation as:

$$\mathbf{u}(\mathbf{p}) \approx \bar{\Psi} \cdot \mathbf{B} \cdot \mathbf{g}(\mathbf{p}) \quad (6.23)$$

Considering the way in which the interpolation coefficients are determined, equation (6.23) gives exact results for the parameters used to generate the snapshots, while it will give some interpolated value for any other parameter. The above formulation represents the "light" model since the system response can be computed by a simple matrix multiplication. To use this approximation, one only needs to compute vector \mathbf{g} as a function of any arbitrary parameter combination according to formula (6.19), since matrices $\bar{\Psi}$ and \mathbf{B} , that are collecting constants, are computed once-for-all. The determination of the matrix \mathbf{B} , however, requires to know the responses for a certain range of the input parameters. This is done by collecting the sets of outputs corresponding to different values of the input vectors through phase called "training" of the POD-RBF model.

In the present context, training of the model is represented by performing a set of Finite Element (FE) simulations to generate snapshots for multiple combinations of parameters of the novel model, which should cover reasonably well the range of interest. For this purpose, the common practice is to use a regular grid over the parameter space. Given that the number of parameters to be identified within the novel model is 26, regular grid distribution would lead to extremely elevated number, requiring 2^{26} parameter combinations in the minimum case. Even for these bare minimum number of parameter sets, required to form a regular grid, it is practically impossible to perform FE simulations, or generally to calibrate matrices $\bar{\Psi}$ and \mathbf{B} . Such circumstances penalizes the training of the POD-RBF procedure and therefore, constrains the application of the

outlined approach, since, it is obvious that for a reasonable approximation, the training of the model must take into account adequate number of points in the parameter space.

To overcome the above mentioned shortcoming, a scheme is proposed within which the POD-RBF model will be trained "selectively". Selective training here implies that the snapshot matrix is generated only for those parameter combinations which are in the zone of the solution, or generally where the value of the objective function is low. To this purpose, a scheme is proposed with employment of POD-RBF model with controllable training, seen as "enrichment", by gradually adding new points in the parameter space throughout the minimization. Therefore the training is directly incorporated into the minimization through genetic algorithm to perform inverse analysis. The description of the proposed methodology is given in the following section.

The initial FE simulations, and subsequent operations required to calibrate matrices for reduced order model, together form the "training" of the model. The sequence of operations is summarized as follows:

- (i) Select X points within the domain of parameters that are subjected to identification.
- (ii) Perform numerical simulations of the considered experiments for these X different parameter vectors \mathbf{p}_i to generate X snapshots \mathbf{u}_i . Store the snapshots and parameters in two matrices \mathbf{U} and \mathbf{P} , respectively.
- (iii) Solve the eigen-value problem for matrix $\mathbf{U}\mathbf{U}^T$ and sort the eigenvectors in descending order of the corresponding eigenvalues.
- (iv) Keep the first few eigenvectors $\boldsymbol{\psi}_i$ (with $i = 1, 2, \dots, K$, with $K \ll X$) corresponding to the eigenvalues whose summation is 99.99% of the total sum of all the eigenvalues. These directions represent the truncated POD basis of the snapshot matrix and are stored in the matrix $\bar{\boldsymbol{\Psi}}$.
- (v) Compute the truncated amplitude matrix $\bar{\mathbf{A}}$ using the equation (6.16).
- (vi) Construct matrix \mathbf{G} for the existing parameter combinations as shown in (6.22).
- (vii) Solve for matrix \mathbf{B} containing the interpolation coefficients utilizing equation (6.21). This step concludes the design and training of the POD-RBF model.

- (viii) To approximate numerical response by POD-RBF model, for any arbitrary parameter \mathbf{p} , compute vector $\mathbf{g}(\mathbf{p})$ according to relation (6.19) and use formula (6.23) to evaluate system response.

6.5 POD-RBF Model with Controllable Enrichment for Inverse Analysis

To setup the Inverse Analysis (IA) procedure, considered measurable quantities are the compaction curves collected from both experiment and simulation of configurations -1 and -5 (figure 4.1a and figure 5.49). The radial stress curves are not employed as input data, since the coefficient of friction has already been determined to be equal to 0.05 for this powder-mold system, as given in the results in the previous chapter, otherwise it can also be considered as an additional parameter to identify. The motivation behind selection of configurations -1 and -5 is the complexity of the novel material model as well as an elevated number of parameters. Therefore, along with configuration-1 which represents a simple geometry (and hence, fairly homogeneous stress distribution over the sample), the purpose of using configuration-5 is to have a more heterogeneous stress distribution and thus "richer" experimental data as input to the IA.

Another advantage of employing a combination of configurations -1 and -5 is that their Finite Element (FE) models can be designed as axially symmetric, thus, requiring far lesser computational time, as opposed to that needed for 3-D models of the configurations -2 and -3 (figure 4.10), used previously as input data for IA procedure. Configuration-1 is discretized into 672 four-node fully integrated axisymmetric elements (marked by CAX4 in ABAQUS), while configuration-5 contains 2480 CAX4 elements. Simulations are performed within the force control regime applying a maximum load of 14 kN, corresponding to experimental details given in tables 5.3 and 5.11. The coefficient of friction defining the lateral contact is kept fixed at a value of 0.05, as previously mentioned. Other simulation conditions are those given in section 3.1.2. Note, that the peak force used within the simulations is smaller than that applied during the experiments, to avoid potential numerical instabilities of FE model for certain

parameter combinations of the novel model, which tend to occur at higher values of relative density.

Compaction curves are recorded both from the experiments and the simulations for both configurations -1 and -5. The curves from the experiments are adjusted accordingly to represent data up to the peak force of 14 kN applied within the simulations. After collecting the experimental and simulated measurements, residual vector is formed quantifying the difference between the two quantities. There are 200 entries in residual vector, such that, from each configuration, 100 points are the differences between displacements corresponding to 100 equidistantly spaced force levels from zero to maximum specified force of 14 kN. Finally, the objective function is formed as the sum of the squares of the members of residual vector and it is minimized with respect to sought parameters of the novel model using genetic algorithms.

In the Genetic Algorithm (GA) methodology, value of the objective function which quantifies the difference between experimental and simulated results, is sorted in ascending order, to create elite, cross-over and mutation kids. Such a feature of GA helps to potentially narrow down the zone of the solution, since the first few members of a generation corresponding to the low values of objective function can be expected to lie in proximity of the final solution. This serves as a reasonable ground to identify the zone where the enrichment of the POD-RBF model should be performed.

Step-by-step description of the developed method, which combines GA with POD-RBF model is given in what follows.

- (i) The first generation is formed by randomly generating $X = 300$ parameter vectors of the novel model, within the pre-defined range suggested by an "expert". These parameters are used to perform FE simulations of the compaction tests for both configurations -1 and -5. In the case of lack of convergence of FE simulations, for either of the two configurations, the member is replaced by another one, with a slight modification of parameters so that the overall number of members in each generation is kept constant.
- (ii) Previous step also served to design two distinct POD-RBF models for configurations -1 and -5, since the responses from FE simulations of both models can be represented

as individual snapshots. For each configuration, every simulation yields a snapshot \mathbf{u} which is formed by recording $Y = 100$ displacement points corresponding to 100 equidistantly spaced force levels from zero to maximum specified force of 14 kN. These snapshots of individual configurations are collected in snapshot matrices \mathbf{U}_1 (for configuration-1) and \mathbf{U}_5 (for configuration-5). To project these matrices into an optimal orthogonal basis, eigenvalue problem is solved on the matrices $\mathbf{S}_1 = \mathbf{U}_1\mathbf{U}_1^T$ and $\mathbf{S}_5 = \mathbf{U}_5\mathbf{U}_5^T$. Obtained eigenvalues are sorted in descending order, and the drop by several orders of magnitude is evidenced for the 15th value with respect to the largest one for both configurations. Therefore, the truncated basis $\overline{\Psi}_1$ and $\overline{\Psi}_5$ corresponding to configuration -1 and -5 respectively, gathered first 14 directions. The amplitudes for these orthogonal directions are computed through equation (6.16) and stored in the matrices $\overline{\mathbf{A}}_1$ and $\overline{\mathbf{A}}_5$.

- (iii) Once the truncated POD basis is formed, Radial Basis Functions (RBF) are employed to interpolate the response from the existing data to compute the numerical response of compaction experiments for any arbitrary parameter combination of the novel model. To this purpose, parameter vectors (\mathbf{p}) used to perform these simulations are normalized between 0 (lower bound) and 1 (upper bound) to take into account the diverse order of magnitude of different entries and are stored in parameter matrix (\mathbf{P}). Using the respective amplitude matrices and the parameter matrix, two corresponding POD-RBF models are designed.
- (iv) From each simulation, compaction curve is extracted and it is compared against the experimental one, for both configurations, to form the residual vector and eventually the objective function as described above. Its value corresponding to each parameter vector is assessed, and these values are then sorted in ascending order.
- (v) Apart from the first generation, all the subsequent generations are formed by performing computations through the POD-RBF models to create elite, cross-over and mutation kids such that: a) the first four parameter vectors with the best (lowest) values of objective function are directly passed to the next generation as the elite kids; b) the next 216 parameter sets are selected to form cross-over kids and c) the worst 80 parameter vectors are subjected to mutation (random perturbation). Instead

of using a constant value for the mutation, an alternative approach is used. The amount of perturbation is kept to be ± 0.4 , ± 0.3 , ± 0.2 and ± 0.1 , up to 50, 100, 150 and 200 generations, respectively. This strategy is driven from the fact that as the number of generations increases, it is reasonable to expect that more and more members would find themselves in the global minimum zone.

- (vi) In the case of replacement of the elite members due to the improvement of the objective function within any particular generation, the response for these members is also calculated through FE simulations for comparative purposes. The vectors collecting displacements corresponding to elite members are collected, from POD-RBF model and FE simulations, for both configurations. The error vector (100 by 1) is formed for each configuration, such that it quantifies the difference between the displacements from the two models (i.e FE and POD-RBF), corresponding to the same force levels, as indicated in step (ii). Further on, the entries of the error vector for both configurations are divided by the corresponding members of the vector collecting displacements from FE simulations and the mean of its entries is computed. Error for each of the two configurations is represented as the mean percentage. The tolerance values for the error is kept to be 8%, 6%, 3% and 1% up to 50, 100, 150 and 200 generations, respectively. If the error between the two models (i.e FE and POD-RBF) is larger than the prescribed tolerance for any of the configurations, enrichments are performed as explained in the next step.
- (vii) Enrichment here refers to performing additional FE simulations for the first few members having low values of the objective function, within the current generation. The responses from these simulations are collected in form of snapshots as described in step (ii) for both configurations. These newly generated snapshots are respectively added as "enrichments" to the already available snapshot matrices formed in step (ii), giving "enriched" snapshot matrices for the two configurations, which are further employed to construct new version of POD-RBF model, following already described sequence of operations. In this way, controllable enrichment of POD-RBF models is performed, with new reduced basis model used for further computations of the new generations of GA. An important aspect of the procedure is the number of members

within each generation that are taken into account for enrichment. Here, 15, 20, 25 and 30 members are considered for enrichment, if the total number of generations is up to 50, 100, 150 and 200, respectively. Such a strategy is reasonable, since it can be expected that within the first few generations, fewer members are in the global minimum zone and this number increases as the algorithm progresses. Therefore, the POD-RBF models for both configurations becomes more accurate, particularly within the zone of interest.

- (viii) In the event of the elite members being replaced, or those that are selected for the enrichments, have convergence difficulties through FE simulations, for either of the configurations, a slight modification of parameters is done. Such a scheme guarantees the same number of members in each generation as well as makes the best possible use of the computational time consumed during FE simulations.
- (ix) The outlined sequence of steps from (ii) to (viii) is repeated until the convergence criteria of the algorithm are met. Here, specifically as stopping criteria, the following values are selected: the total number of generations reaches 200 or the stalling generation exceeds 30 (i.e number of generations without any improvement of best member's objective function value), the algorithm is stopped. From the last generation upon the termination of the minimization process, the best member is taken as solution to the inverse analysis.

The procedure of combining the GA with POD-RBF model relies on three major factors: a) the ability of GA to find the global minimum even when the objective function is neither continuous nor differentiable, thereby helping to deal with certain numerical instabilities of the novel model; b) sorting of the values of the objective function within GA, enabling to perform controllable enrichment of POD-RBF model; and c) the use of POD-RBF model to substitute FE simulations, contributing to the significant reduction of computational burden, and hence, making minimization through GA viable. Such features of GA and POD-RBF model are exploited simultaneously to perform inverse analysis procedure for determining parameters of the novel model, with the results of the identification presented in what follows.

6.6 Results and Discussions

The novel material model is defined through 28 parameters. Out of these, 26 parameters are assessed and the two parameters, namely: initial void ratio (e_0) and exponential decay term of elasto-plastic coupling (n) are not subjected to the identification, and kept fixed at values of 0.5 and 2, respectively. The evaluated values of the parameters are given in table 6.2. The comparison between the experimental and simulated curves for configurations -1 and -5 is presented in figures 6.4 and 6.5.

Table 6.2. Parameters of the novel constitutive model corresponding assessed through IA employing configuration-1 and -5 as inputs

Serial Number	Parameter	Parameter Value	Units	Parameter Description
Yield Surface Parameters				
1.	p_{c0}	0.366	[MPa]	<i>Initial Hardening</i>
2.	M_0	0.984	-	<i>Pressure Sensitivity</i>
3.	k_1	0.537	-	
4.	δ_1	227.940	-	
5.	n_1	2.004	-	
6.	m_1	1.825	[MPa]	<i>Meridian Shape Parameters</i>
7.	m_2	2.033	-	
8.	α_1	0.183	-	
9.	α_2	1.312	-	
10.	β	1.811	-	<i>Deviatoric Shape Parameters</i>
11.	γ_1	0.863	-	
12.	γ_2	0.450	[MPa]	
13.	η	0.521	-	<i>Plastic flow</i>
Hardening Parameters				
14.	a_1	0.701	-	<i>Cooper-Eaton Hardening</i>
15.	λ_1	0.486	[MPa]	
16.	a_2	0.252	-	
17.	λ_2	8.825	[MPa]	
18.	p_{cb}	1.196	[MPa]	<i>Cohesion Related Hardening</i>
19.	c_∞	1.124	[MPa]	
20.	Γ_c	0.047	[MPa ⁻¹]	
Elastic Parameters				
21.	Λ_1	209.090	[MPa]	<i>Lame's Constants</i>
22.	μ_1	28.107	[MPa]	
23.	Λ_2	4648.020	[MPa]	
24.	μ_2	599.830	[MPa]	
25.	Γ_F	0.996	[MPa ⁻¹]	<i>Elasto-plastic Coupling</i>
26.	p_0	0.113	[MPa]	

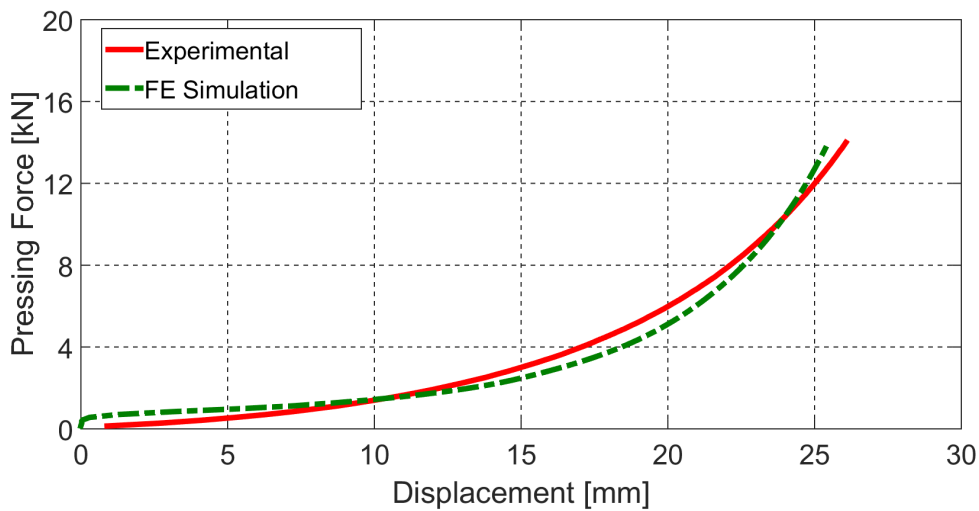


Figure 6.4. Experimental vs. final computed compaction curve from FE simulation for configuration-1, corresponding to parameters of the novel model identified through IA employing configuration-1, and -5 as inputs

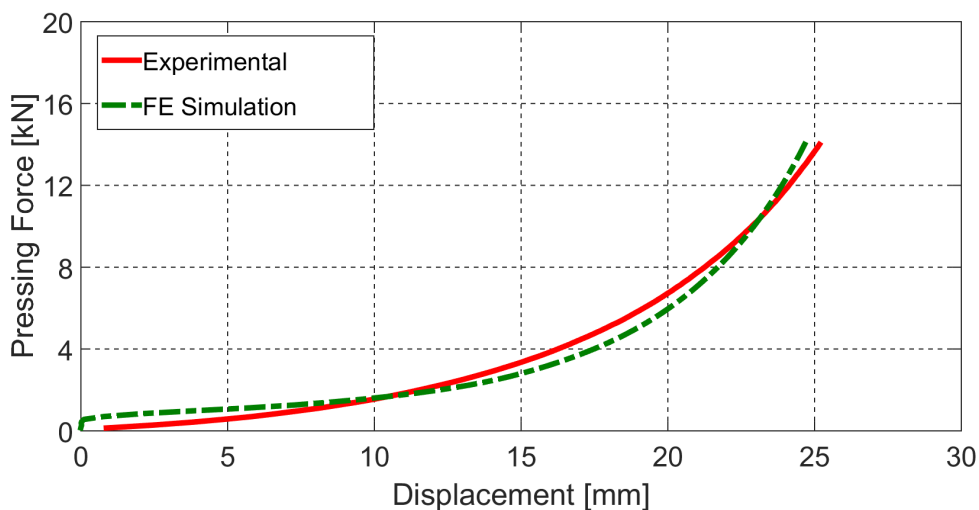


Figure 6.5. Experimental vs. final computed compaction curve from FE simulation for configuration-5, corresponding to parameters of the novel model identified through IA employing configuration-1, and -5 as inputs

The above figures show that the compaction curves from experiment and simulation are in good agreement for both configurations -1 and -5. The minimization result is achieved in 188 generations and it is terminated due to reaching the stopping criterion of exceeding 30 generations with no improvement in the objective function. The other details of the developed procedure are given in table 6.3. The complete first generation comprising of 300 simulations each for both configurations and an additional 2570,

making a total of 3170 simulations are performed by the full order finite element model, which is about 5% of the overall number of objective function evaluations. Considering that remaining function evaluations are done on the basis of POD-RBF model, such strategy represents computational time reduction by almost five times, since calculation of system response through POD-RBF model is practically done in a real time. It represents significant time savings as one compaction simulation for both configurations takes about 7 minutes on a computer with i7 processor and 8GB of RAM.

Table 6.3. Parameters of the novel constitutive model corresponding assessed through IA employing configuration-1 and -5 as inputs

Generation	Members for Enrichment through FE Simulations	Number of Enrichments	FE Simulations Performed (Column 1 x Column 2 x 2 Configurations)	FE Simulations (if Classical GA)
2-50	15	36	1080	14700
51-100	20	23	920	15000
101-150	25	9	450	15000
151-188*	30	2	120	11400
Total FE Simulations			2570	57100

Furthermore, the accuracy of POD-RBF model is verified by comparing its results against FE simulations, for the final set of parameters obtained at the end of minimization process, which are listed in table 6.2. The comparison is presented in figures 6.6 and 6.7. It can be observed that there is an insignificant difference between the two curves, which corroborates that the fast computations offered by POD-RBF models are not introducing any additional error within the identification procedure.

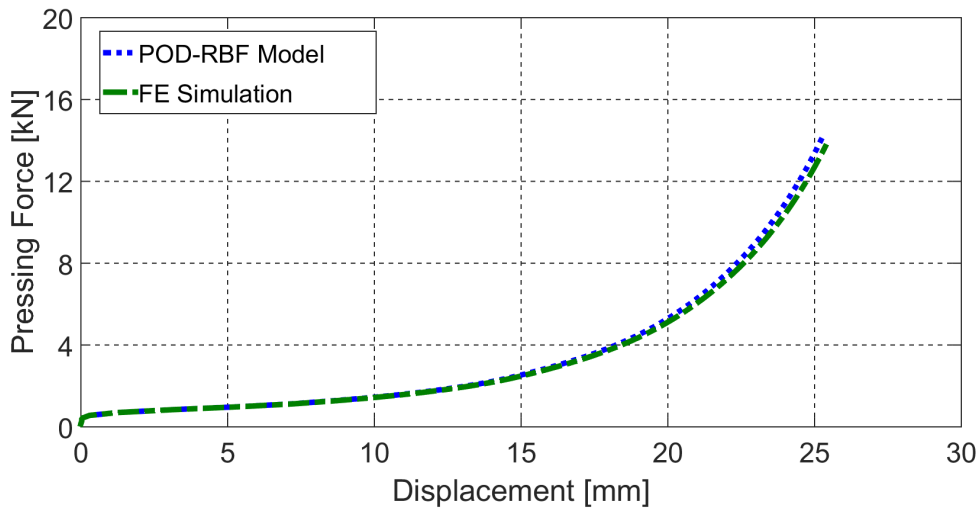


Figure 6.6. Comparison of compaction curves generated through POD-RBF model and FE simulation for configuration-1, corresponding to parameters of the novel model identified through IA employing configuration-1, and -5 as inputs

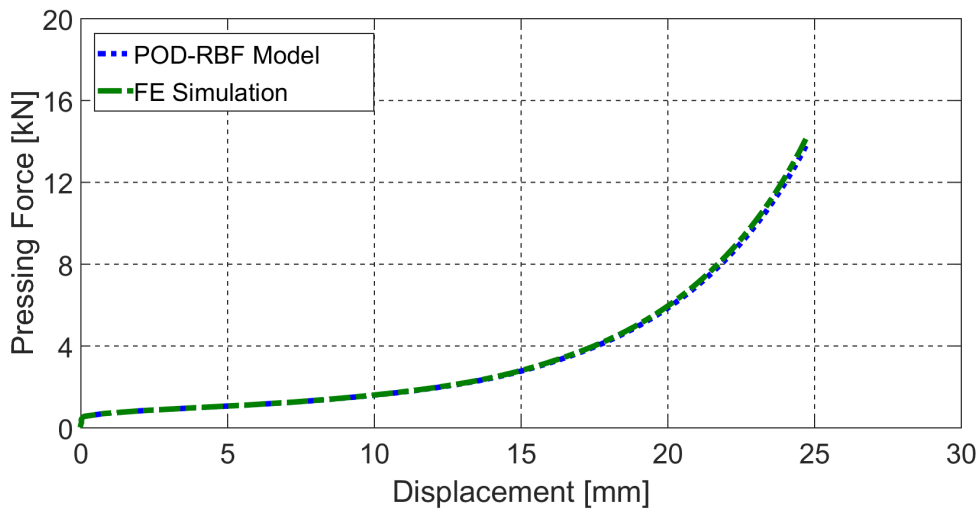


Figure 6.7. Comparison of compaction curves generated through POD-RBF model and FE simulation for configuration-5, corresponding to parameters of the novel model identified through IA employing configuration-1, and -5 as inputs

To validate the proposed calibration method, and in turn the identified parameters of the novel model listed in table 6.2, compaction simulations of complex geometries, namely, configuration -6 and -7 (given in figure 5.49) are performed using these parameters. The simulated curves are compared against the experimental ones, with results visualized in figures 6.8 and 6.9.

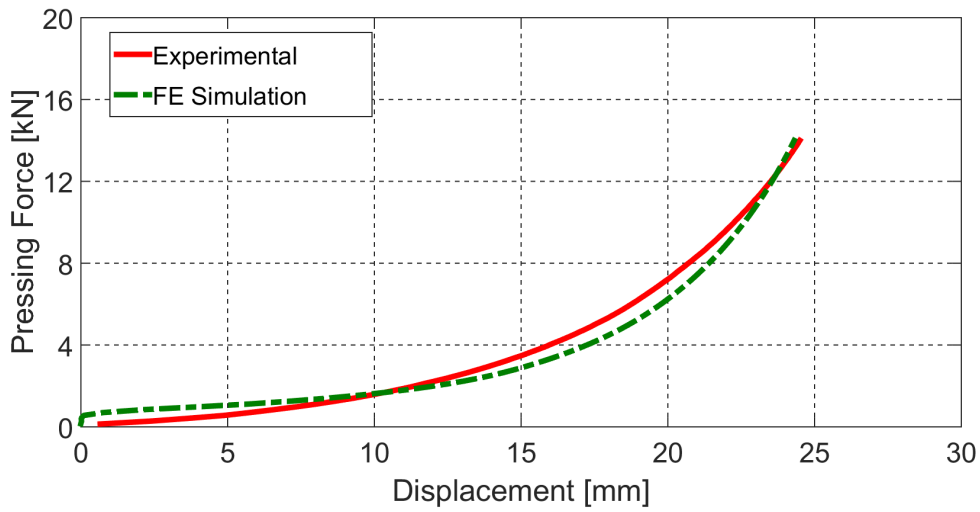


Figure 6.8. Experimental vs. final computed compaction curve from FE simulation for configuration-6, corresponding to parameters of the novel model identified through IA employing configuration-1, and -5 as inputs

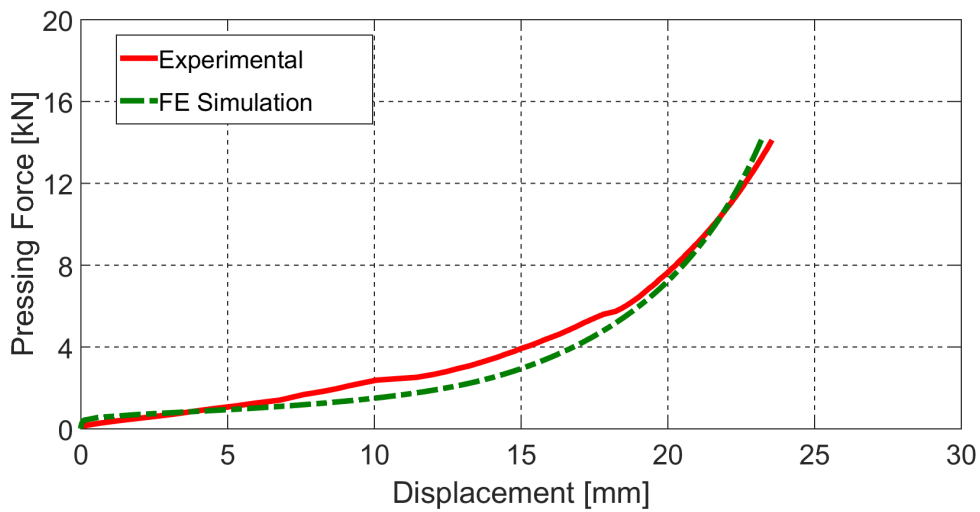


Figure 6.9. Experimental vs. final computed compaction curve from FE simulation for configuration-7, corresponding to parameters of the novel model identified through IA employing configuration-1, and -5 as inputs

The above results evidence that the inverse problem is well posed. The fact that the parameters obtained through the developed calibration strategy can be used to model compaction involving arbitrary geometries, confirms that the established procedure provides an efficient transition from experimental data, collected from pressing test, to the constitutive parameters, even for complex material models like the one considered here.

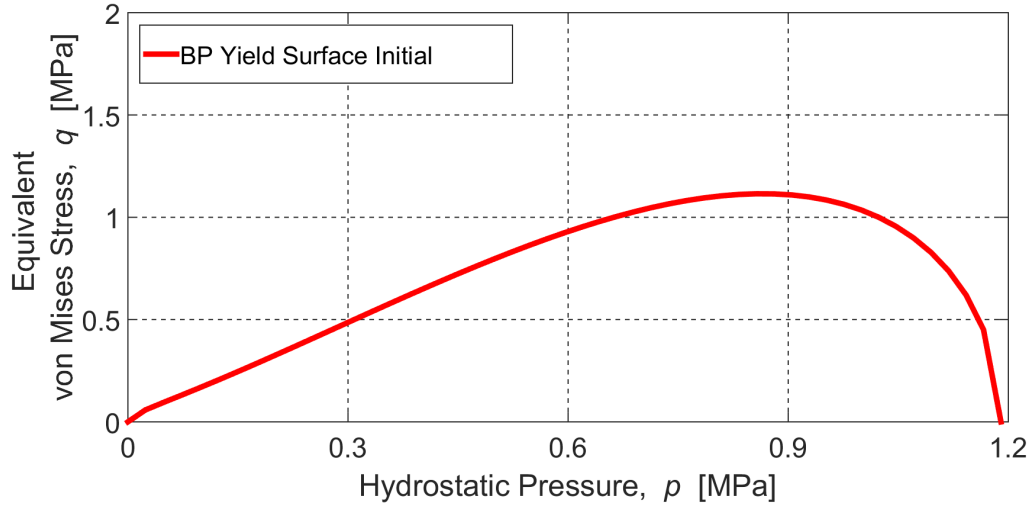
The Inverse Analysis (IA) procedure inherently contains numerical simulations of the experiment, which may be unstable when complex constitutive models are utilized. Such circumstance penalizes the use of efficient derivative based algorithms for providing the solution to the resulting minimization problem within IA. Alternatively, Genetic Algorithms (GA) can be exploited, with increased computational effort, as these algorithms are involving a larger number of simulations. To make the computational burden consistent with constrains related to the employment of GA, the use of reduced basis model, as considered within this work, turns out to be crucial. Proposed training scheme, different from previous studies (see e.g. [16, 48]) works fairly effective in present context, by providing the enrichments of the POD-RBF model throughout the minimization. The computational effort is therefore concentrated within the zone of parameters with a low value of the objective function.

However, due to an elevated number of parameters, the designed POD-RBF model cannot be trained once-and-for-all over the whole domain of parameters. This presents a limitation since the system response cannot be computed for any arbitrary parameter combinations that are far from the zone where the model is enriched. This implies that full order FE model will again be employed to perform simulations for such parameter combinations, as opposed to the POD-RBF models utilizing regular grids over the whole parameter space, which can calculate the numerical response for any arbitrary parameter once their training is complete. However, for any situation, where the number of sought parameters is high, it is practically impossible to train the POD-RBF procedure according to regular grid distribution, and the proposed training scheme may be an advantageous alternative.

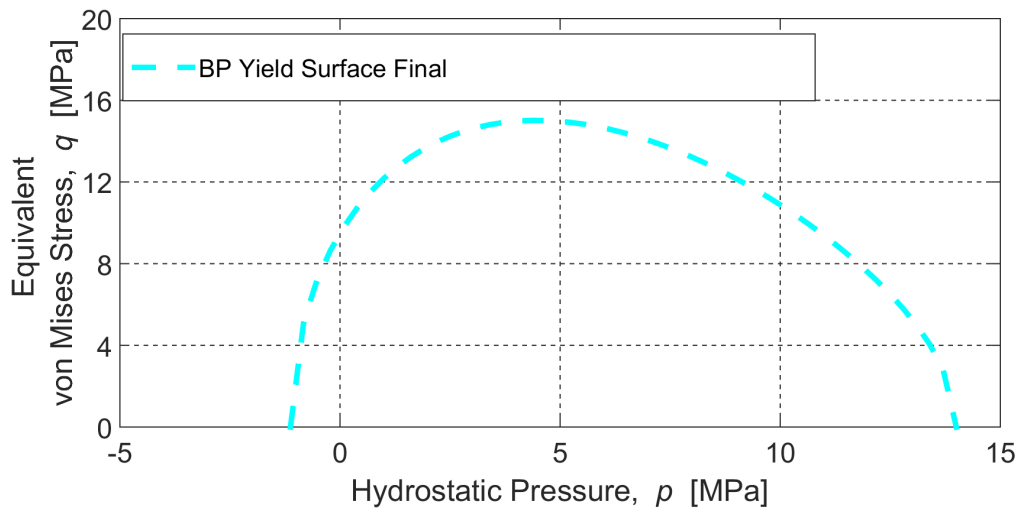
6.6.1 Comparison between Drucker-Prager Cap and Bigoni Piccolroaz Yield Surface

One of the unique features of the novel constitutive model is represented through the Bigoni-Piccolroaz (BP) yield criterion, which has the ability to change the shape of the yield surface. To demonstrate this, the yield surface corresponding to initial and final

stages of compaction are visualized in figure 6.10, which is plotted by inputting the parameters listed in table 6.2 into equation 6.1.



(a) Bigoni-Piccolroaz yield surface resembling Drucker-Prager Cap type yield surface during initial stages of compaction



(b) Bigoni-Piccolroaz yield surface resembling either Cam Clay type yield surface during final stages of compaction

Figure 6.10. Evolution of Bigoni-Piccolroaz yield surface during compaction for powder from granular to dense state

Indeed, the above figure indicates the transformation of the yield surface from Drucker-Prager Cap (DPC) type, which is typical for granular material, to Cam Clay like surface for dense solid. Therefore, it is more relevant to compare the DPC and BP yield surface only for the initial stages of compaction. It should be recalled that according to BP yield criterion, cohesion only starts to develop once the breakpoint pressure (p_{cb}) is

reached, which is identified as 1.19 MPa, while no such rule is defined for DPC yield criterion. Therefore, to establish a fair comparison, the BP yield surface is plotted for hydrostatic pressure ($p=1.25$ MPa), which is slightly higher than the breakpoint pressure, marking the onset of cohesion. The relative density of the sample is recalculated from the plastic strain through equation (2.7), which corresponds to 62% for this hydrostatic pressure. For obtaining the DPC parameters at 62% relative density, previously identified values listed in table 5.10 are used in combination with equation (3.3). The comparison between the two yield surfaces is presented in the following figure.

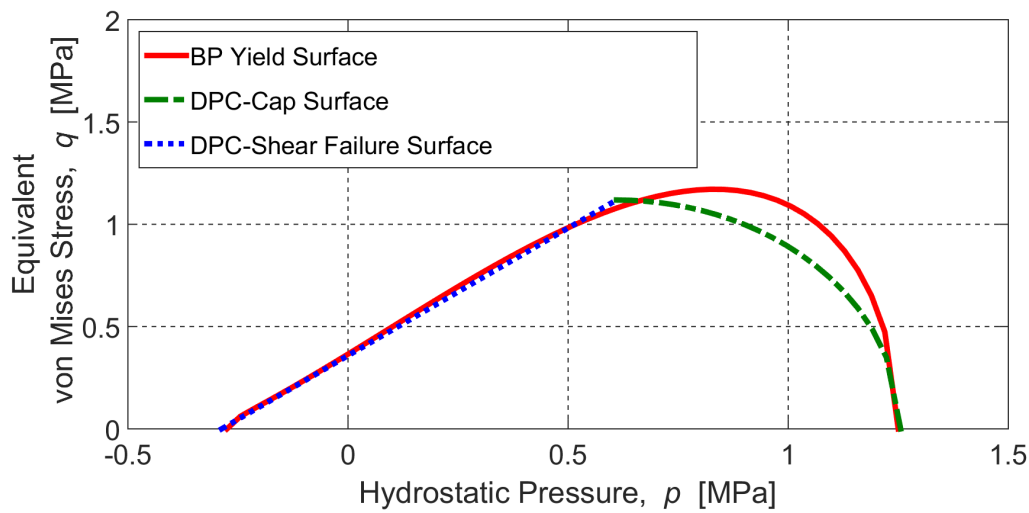


Figure 6.11. Comparison between Drucker-Prager Cap and Bigoni-Piccolroaz yield surface in initial stages of compaction after cohesion starts developing in the powder.

The above figure shows a good agreement between the DPC and novel material model for the initial part of the compaction. This contributes to the conclusion that DPC yield criterion models the initial compaction accurately enough.

To establish some relevant comparison for the final part of compaction between the BP and DPC criterion, final values of some of the similar parameters are listed in table 6.4. Note that the cohesion here for DPC model refers to the intersection of yield surface with the hydrostatic pressure axis on the tension side (negative side on the p - q plot). Hardening parameter here is the intersection of yield surface with the hydrostatic pressure axis on the compression side (positive side), which is marked as hydrostatic yield compression stress (p_b) in the DPC model and hardening parameter (p_c) in the novel model. Young's modulus for the novel model is recalculated from the values of Lamé's constants.

Table 6.4. Comparison between the final values of similar parameters for novel constitutive model and DPC model

Parameter	Final Value (Relative Density=0.82)		
	DPC Model	Novel Model	Difference
Young's Modulus	1.724 GPa	1.801 GPa	4.275 %
Cohesion	1.071 MPa	1.124 MPa	4.715 %
Hardening Parameter	13.231 MPa	14.020 MPa	5.627 %

It can be observed that values of the parameters for the two criteria are comparable and the points at which these surfaces intersect the hydrostatic pressure axis are reasonably close. This indicates that even though the shape of the final yield surfaces are fairly different for BP and DPC yield criterion, both of them represent similar extreme values for the allowed stress. In the present research, for this powder composition, the loading path of the considered geometries tends to be closer to the hydrostatic axis (for instance, see figure 2.5). Therefore, satisfactory results are obtained from the DPC model, since the transformation of the yield surface becomes irrelevant for the examples treated within this work. However, such flexibility of the yield surface could be advantageous and play an important role when modeling compaction of certain powder compositions or even more complex geometries, which cannot be taken into account through the DPC model.

Chapter 7

CONCLUSIONS AND FUTURE WORK

7.1 Conclusions

In the present work, a fully automated procedure is designed to calibrate the constitutive models used in powder compaction simulations. During the compaction, powder transforms from a granular state to a dense solid called "green body", exhibiting fairly different mechanical properties for these two states. Therefore, modeling of the compaction process is a challenging task, with simulations often involving complex constitutive models like, Drucker-Prager Cap (DPC) [28, 31, 70], Cam-Clay [24], etc., which are defined through an elevated number of parameters.

Currently adopted praxis to evaluate the constants entering the material models relies on performing time consuming destructive tests on a green body (for instance, Brazilian and crush tests) [2, 28, 70]. Even though such calibration protocol provides a reasonable estimate of the material parameters, a large number of experiments is needed. Furthermore, some of the parameters cannot be determined at relatively low densities of green body through the conventional experimental route [26]. Such circumstances make the application of the current praxis rather difficult and fairly expensive for routine industrial purposes.

To tackle this problem, an alternative approach based on Inverse Analysis (IA) is developed. The central novelty of this research is the development of more accurate and

more economical parameter calibration method, that relies on data collected from the compaction tests only. Such scheme is obviously more efficient and advantageous for routine industrial applications, since it fully eliminates the need for heavy experimental regime adopted currently.

Inverse Analysis (IA) procedure is centered on the minimization of the discrepancy between experimentally measured quantities and their numerically computed counterparts [13]. From the compaction experiment, digitalized compaction force vs. displacement (of the punch) curve and compaction force vs. radial stress (measured from the die-wall) graphs are collected as measurable quantities. To ascertain the strong influence of sought parameters on the measured data, systematic sensitivity analyses are performed, and different mold geometries (i.e configurations) are designed. A combination of these configurations represents the source of experimental data, while their simulations, performed in commercial code ABAQUS, give the simulated data. Discrepancy function is setup quantifying the difference between the two measured quantities and the parameters which minimize this function represent the solution to the inverse problem and also the representative material properties.

The developed IA approach is tested to calibrate the Drucker-Prager Cap (DPC) model which is frequently adopted for powder compaction simulations [2, 23, 28, 31, 70]. For accurate modeling, the typical DPC model is "modified" such that the parameters are defined as a continuous function of accumulated plastic strain, which is then converted to relative density. The proposed relationship between the parameters and relative density is very general, capable of taking into account distinct trends of evolution for different parameters. Such modification provides very flexible definition of hardening (i.e. the dependency of yield function parameters on accumulated plastic strain), which incorporates both linear and exponential trends. Along with the DPC model parameters, the coefficient of friction is also evaluated as opposed to previous studies where it has been assumed as a constant value [26] or derived through empirical relations [28, 45, 59] usually representing a source of an error.

The minimization problem is solved through the Trust Region Algorithm (TRA). The obtained parameters from IA successfully simulate the compaction of miniaturized green bodies typically resembling industrial parts, validating the established calibration

protocol. The parameters assessed via IA are in good agreement with those evaluated through conventional experimental route, with multiple advantages that are listed here:

- The number of experiments required for the calibration by the IA procedure are three as compared to about 60 that are needed based on the currently adopted praxis, highlighting significant efficiency of the developed calibration method.
- Through IA, the parameters are assessed as a continuous function of relative density as compared to the current praxis, where the parameters can only be estimated for discrete relative densities.
- Through proposed procedure the parameters can also be evaluated for very low relative densities, which cannot be done via conventional experimental route.

To further test the IA methodology, calibration of a more sophisticated constitutive model relying on the Bigoni-Piccolroaz yield criterion is considered [7, 49, 51]. Apart from the elevated number of parameters, this model showed unstable simulations for certain parameter combinations. Such circumstance penalizes the use of efficient Trust Region Algorithm (TRA) for the minimization. As a remedy, Genetic Algorithms (GA) are employed. The computational burden coming from GA is made consistent with repetitive routine applications through reduced basis model.

In the present work, Proper Orthogonal Decomposition (POD) is chosen as the model reduction technique. Such strategy allows to approximate the system response by projecting it in new reference frame with significant reduction in its dimensionality, while still preserving reasonable accuracy of the approximation. Within the POD model, the spatial distribution of the field of interest (displacements from compaction curve in this case) are described using POD directions, while its amplitudes depend on the sought parameters. This functional dependence of amplitudes on the parameters is expressed as a linear combination through *a priori* chosen Radial Basis Functions (RBF), which are frequently used for scattered data interpolation. The coefficients of this combination are evaluated by satisfying the solution exactly for pre-selected inputs (parameters of novel model) and outputs (vectors collecting displacements from compaction curve) through a phase called "training". However, the previously adopted training methods [16, 48]

utilizing the regular grid over parameter space, cannot be employed for the current POD-RBF model, since the number of parameters is quite high.

To overcome this difficulty, a scheme is designed to controllably train the POD-RBF model, seen here as "enrichments", only for those parameter combinations that are in the zone of the solution. It is achieved by incorporating the training procedure directly into the minimization through genetic algorithms. The best members within each generation in GA lie in the proximity of the final solution, serving as a reasonable ground to identify the zone for performing enrichment of POD-RBF model.

Using the developed scheme, the minimization problem is solved and obtained parameters successfully simulate complex geometries, validating the established procedure. It is interesting to note that almost 95% of function evaluations of GA are performed through POD-RBF model, which are done in almost real-time, offering significant time savings. It is also observed that the fast computations offered by POD-RBF model do not represent any additional source of error. This contributes to the conclusion, that the developed IA procedure employing POD-RBF model with controllable enrichment can be effectively used to calibrate complex constitutive models, with an elevated number of parameters and whose numerical implementation is not fully stable. This particular scheme can be useful also in other applications when dealing with complex material models, and not only in the present context of powder compaction.

7.2 Future Research

In the current research, developed protocol based on Inverse Analysis (IA) is successfully applied to the calibration of Drucker-Prager Cap (DPC) model and novel constitutive model. However, the methodology could very well be extended to other material models like Cam-Clay or Gurson, and even for different groups of powders.

The examples treated in this thesis use IA in a deterministic sense, however, such procedure could be tailored to include the uncertainty within the process by employing techniques like Kalman filters [27, 33]. In practical applications it is often observed that the compaction curves corresponding to the same powder under similar conditions are slightly different, and this discrepancy becomes even more pronounced at lower relative

densities. Such behavior could be accounted through stochastic IA. The main idea to perform such an IA remains the same, and the parameters are evaluated with some standard deviation corresponding to the associated noise endowed in measurable quantities, or generally some errors of different origins present in the model. To this purpose, Kalman filters look promising and have been already been employed in material characterization through indentation tests [17], flat jack tests [25], etc. Their implementation in the present context requires further investigations, and can be the topic of future research.

The reduced basis model used herein employs controllable training in the zone of interest. Such scheme could be useful for any complex constitutive model involving an elevated number of parameters, where the regular grid distribution is not possible, as previously mentioned. A desirable extension of this strategy would be its investigation in the context of multi-scale models. It would also be interesting to explore the model reduction based on proper generalized decomposition as it eliminates the need for laborious training which is involved when proper orthogonal decomposition is used. This technique has already been applied in other fields of research [46], but the context was different and its application to goals pursued in this study requires further investigations.

This page is intentionally left blank.

Bibliography

- [1] ABAQUS. *Theory and user's manuals, release 6.5-1*. HKS Inc., Pawtucket, 2005.
- [2] Almanstötter, J. “A modified Drucker–Prager Cap model for finite element simulation of doped tungsten powder compaction”. *International Journal of Refractory Metals and Hard Materials*, Volume 50, 2015, pp. 290–297.
- [3] Almanstötter, J. “Materials physics based numerical simulation in powder metallurgical processing and calibration of material models”. *Metal Powder Report*, Volume 71, Number 5, 2016, pp. 333–338.
- [4] ASTM, D. “3967, Standard Test Method for Splitting Tensile Strength of Intact Rock Core Specimens”. *ASTM International, West Conshohocken, PA*.
- [5] Berkooz, G., Holmes, P., and Lumley, J. L. “The proper orthogonal decomposition in the analysis of turbulent flows”. *Annual Review of Fluid Mechanics*, Volume 25, Number 1, 1993, pp. 539–575.
- [6] Bialecki, R., Kassab, A., and Fic, A. “Proper orthogonal decomposition and modal analysis for acceleration of transient FEM thermal analysis”. *International Journal for Numerical Methods in Engineering*, Volume 62, Number 6, 2005, pp. 774–797.
- [7] Bigoni, D. and Piccolroaz, A. “Yield criteria for quasibrittle and frictional materials”. *International journal of solids and structures*, Volume 41, Number 11, 2004, pp. 2855–2878.
- [8] Bolzon, G., Buljak, V., Maier, G., and Miller, B. “Assessment of elastic–plastic material parameters comparatively by three procedures based on indentation test and inverse analysis”. *Inverse Problems in Science and Engineering*, Volume 19, Number 6, 2011, pp. 815–837.

- [9] Bolzon, G., Chiarullo, E. J., Egizabal, P., and Estournes, C. “Constitutive modelling and mechanical characterization of aluminium-based metal matrix composites produced by spark plasma sintering”. *Mechanics of Materials*, Volume 42, Number 5, 2010, pp. 548–558.
- [10] Bolzon, G., Maier, G., and Panico, M. “Material model calibration by indentation, imprint mapping and inverse analysis”. *International Journal of Solids and Structures*, Volume 41, Number 11, 2004, pp. 2957–2975.
- [11] Borsic, A., Comina, C., Foti, S., Lancellotta, R., and Musso, G. “Imaging heterogeneities with electrical impedance tomography: laboratory results”. *Géotechnique*, Volume 55, Number 7, 2005, pp. 539–547.
- [12] Buljak, V., Cocchetti, G., and Maier, G. “Calibration of brittle fracture models by sharp indenters and inverse analysis”. *International Journal of Fracture*, Volume 184, Number 1-2, 2013, pp. 123–136.
- [13] Buljak, V. *Inverse analyses with model reduction: proper orthogonal decomposition in structural mechanics*. Springer Verlag, Berlin, 2011.
- [14] Buljak, V. “Proper orthogonal decomposition and radial basis functions algorithm for diagnostic procedure based on inverse analysis”. *FME Transactions*, Volume 38, Number 3, 2010, pp. 129–136.
- [15] Buljak, V. and Maier, G. “Identification of residual stresses by instrumented elliptical indentation and inverse analysis”. *Mechanics Research Communications*, Volume 41, 2012, pp. 21–29.
- [16] Buljak, V. and Maier, G. “Proper orthogonal decomposition and radial basis functions in material characterization based on instrumented indentation”. *Engineering Structures*, Volume 33, Number 2, 2011, pp. 492–501.
- [17] Buljak, V., Pandey, S., and Balać, I. “Material model calibration through indentation test and stochastic inverse analysis”. *FME Transactions*, Volume 45, Number 1, 2017, pp. 109–116.
- [18] Chatterjee, A. “An introduction to the proper orthogonal decomposition”. *Current science*, 2000, pp. 808–817.

- [19] Chen, X., Deng, X., Sutton, M. A., and Zavattieri, P. “An inverse analysis of cohesive zone model parameter values for ductile crack growth simulations”. *International Journal of Mechanical Sciences*, Volume 79, 2014, pp. 206–215.
- [20] Chisari, C., Macorini, L., Amadio, C., and Izzuddin, B. “An inverse analysis procedure for material parameter identification of mortar joints in unreinforced masonry”. *Computers & Structures*, Volume 155, 2015, pp. 97–105.
- [21] Cunningham, J., Sinka, I., and Zavaliangos, A. “Analysis of tablet compaction. I. Characterization of mechanical behavior of powder and powder/tooling friction”. *Journal of Pharmaceutical Sciences*, Volume 93, Number 8, 2004, pp. 2022–2039.
- [22] Damasceno, V. and Fratta, D. “Monitoring chemical diffusion in a porous media using electrical resistivity tomography”. In: *Site and Geomaterial Characterization*. 2006, pp. 174–181.
- [23] Diarra, H., Mazel, V., Boillon, A., Rehault, L., Busignies, V., Bureau, S., and Tchoreloff, P. “Finite Element Method (FEM) modeling of the powder compaction of cosmetic products: Comparison between simulated and experimental results”. *Powder Technology*, Volume 224, 2012, pp. 233–240.
- [24] Diarra, H., Mazel, V., Busignies, V., and Tchoreloff, P. “Comparative study between Drucker-Prager/Cap and modified Cam-Clay models for the numerical simulation of die compaction of pharmaceutical powders”. *Powder Technology*, Volume 320, 2017, pp. 530–539.
- [25] Fedele, R. and Maier, G. “Flat-jack tests and inverse analysis for the identification of stress states and elastic properties in concrete dams”. *Meccanica*, Volume 42, Number 4, 2007, pp. 387–402.
- [26] Garner, S., Strong, J., and Zavaliangos, A. “The extrapolation of the Drucker–Prager/Cap material parameters to low and high relative densities”. *Powder Technology*, Volume 283, 2015, pp. 210–226.
- [27] Gibbs, B. P. *Advanced Kalman filtering, least-squares and modeling: a practical handbook*. John Wiley & Sons, 2011.

- [28] Han, L., Elliott, J., Bentham, A., Mills, A., Amidon, G., and Hancock, B. “A modified Drucker-Prager Cap model for die compaction simulation of pharmaceutical powders”. *International Journal of Solids and Structures*, Volume 45, Number 10, 2008, pp. 3088–3106.
- [29] Huang, F., An, X., Zhang, Y., and Yu, A. “Multi-particle FEM simulation of 2D compaction on binary Al/SiC composite powders”. *Powder Technology*, Volume 314, 2017, pp. 39–48.
- [30] Jiang, Y., Li, G., Qian, L.-X., Liang, S., Destrade, M., and Cao, Y. “Measuring the linear and nonlinear elastic properties of brain tissue with shear waves and inverse analysis”. *Biomechanics and modeling in mechanobiology*, Volume 14, Number 5, 2015, pp. 1119–1128.
- [31] Kadiri, M. and Michrafy, A. “The effect of punch’s shape on die compaction of pharmaceutical powders”. *Powder Technology*, Volume 239, 2013, pp. 467–477.
- [32] Kallel, A. Enabling Technologies Department, Vesuvius Group, Ghlin, Belgium.
- [33] Kalman, R. E. and Bucy, R. S. “New results in linear filtering and prediction theory”. *Journal of basic engineering*, Volume 83, Number 1, 1961, pp. 95–108.
- [34] Kerschen, G., Poncelet, F., and Golinval, J.-C. “Physical interpretation of independent component analysis in structural dynamics”. *Mechanical Systems and Signal Processing*, Volume 21, Number 4, 2007, pp. 1561–1575.
- [35] LaMarche, K., Buckley, D., Hartley, R., Qian, F., and Badawy, S. “Assessing materials’ tablet compaction properties using the Drucker–Prager Cap model”. *Powder Technology*, Volume 267, 2014, pp. 208–220.
- [36] Li, L., Ye, B., Liu, S., Hu, S., and Li, B. “Inverse analysis of the stress–strain curve to determine the materials models of work hardening and dynamic recovery”. *Materials Science and Engineering: A*, Volume 636, 2015, pp. 243–248.
- [37] Li, W., Krist, S., and Campbell, R. “Transonic airfoil shape optimization in preliminary design environment”. *Journal of aircraft*, Volume 43, Number 3, 2006, pp. 639–651.

- [38] Liang, W., Murakawa, H., and Deng, D. “Estimating inherent deformation in thin-plate Al-alloy joint by means of inverse analysis with the help of cutting technique”. *Advances in Engineering Software*, Volume 99, 2016, pp. 89–99.
- [39] Ly, H. V. and Tran, H. T. “Modeling and control of physical processes using proper orthogonal decomposition”. *Mathematical and Computer Modelling*, Volume 33, Number 1-3, 2001, pp. 223–236.
- [40] Magalhaes, R., Braga, R., and Barbosa, B. “Young’ s Modulus evaluation using Particle Image Velocimetry and Finite Element Inverse Analysis”. *Optics and Lasers in Engineering*, Volume 70, 2015, pp. 33–37.
- [41] MATLAB. *User’s guide and optimization toolbox, release 6.13*. Math Works Inc., USA, 2002.
- [42] McPhee, N. F., Poli, R., and Langdon, W. B. “Field guide to genetic programming”, 2008.
- [43] Muñoz, V. and Martinez, A. G. T. “Factors controlling the mechanical behavior of alumina–magnesia–carbon refractories in air”. *Ceramics International*, Volume 42, Number 9, 2016, pp. 11150–11160.
- [44] Nakamura, T., Kamimura, Y., Igawa, H., and Morino, Y. “Inverse analysis for transient thermal load identification and application to aerodynamic heating on atmospheric reentry capsule”. *Aerospace Science and Technology*, Volume 38, 2014, pp. 48–55.
- [45] Nedderman, R. M. *Statics and kinematics of granular materials*. Cambridge University Press, 2005.
- [46] Nouy, A. “A priori model reduction through proper generalized decomposition for solving time-dependent partial differential equations”. *Computer Methods in Applied Mechanics and Engineering*, Volume 199, Number 23-24, 2010, pp. 1603–1626.
- [47] Oddone, V., Boerner, B., and Reich, S. “Composites of aluminum alloy and magnesium alloy with graphite showing low thermal expansion and high specific

- thermal conductivity”. *Science and Technology of Advanced Materials*, Volume 18, Number 1, 2017, pp. 180–186.
- [48] Ostrowski, Z., Bialecki, R. A., and Kassab, A. J. “Estimation of constant thermal conductivity by use of proper orthogonal decomposition”. *Computational Mechanics*, Volume 37, Number 1, 2005, pp. 52–59.
- [49] Penasa, M., Argani, L., Misseroni, D., Dal Corso, F., Cova, M., and Piccolroaz, A. “Computational modelling and experimental validation of industrial forming processes by cold pressing of aluminum silicate powder”. *Journal of the European Ceramic Society*, Volume 36, Number 9, 2016, pp. 2351–2362.
- [50] Piccolroaz, A., Bigoni, D., and Gajo, A. “An elastoplastic framework for granular materials becoming cohesive through mechanical densification. Part II—the formulation of elastoplastic coupling at large strain”. *European Journal of Mechanics-A/Solids*, Volume 25, Number 2, 2006, pp. 358–369.
- [51] Piccolroaz, A., Bigoni, D., and Gajo, A. “An elastoplastic framework for granular materials becoming cohesive through mechanical densification. Part I—small strain formulation”. *European Journal of Mechanics-A/Solids*, Volume 25, Number 2, 2006, pp. 334–357.
- [52] Resende, W., Stoll, R., Justus, S., Andrade, R., Longo, E., Baldo, J., Leite, E., Paskocimas, C., Soledade, L., Gomes, J., et al. “Key features of alumina/magnesia/graphite refractories for steel ladle lining”. *Journal of the European Ceramic Society*, Volume 20, Number 9, 2000, pp. 1419–1427.
- [53] Rogers, A. and Ierapetritou, M. “Challenges and opportunities in modeling pharmaceutical manufacturing processes”. *Computers & Chemical Engineering*, Volume 81, 2015, pp. 32–39.
- [54] Rojek, J., Nosewicz, S., Jurczak, K., Chmielewski, M., Bochenek, K., and Pietrzak, K. “Discrete element simulation of powder compaction in cold uniaxial pressing with low pressure”. *Computational Particle Mechanics*, Volume 3, Number 4, 2016, pp. 513–524.

BIBLIOGRAPHY

- [55] Rojek, J., Nosewicz, S., Maździarz, M., Kowalczyk, P., Wawrzyk, K., and Lumelskyj, D. “Modeling of a sintering process at various scales”. *Procedia Engineering*, Volume 177, 2017, pp. 263–270.
- [56] Ruotolo, R. and Surace, C. “Using SVD to detect damage in structures with different operational conditions”. *Journal of Sound and Vibration*, Volume 226, Number 3, 1999, pp. 425–439.
- [57] Ryckelynck, D., Chinesta, F., Cueto, E., and Ammar, A. “On the a priori model reduction: overview and recent developments”. *Archives of Computational methods in Engineering*, Volume 13, Number 1, 2006, pp. 91–128.
- [58] Shang, C., Sinka, I., and Pan, J. “Constitutive model calibration for powder compaction using instrumented die testing”. *Experimental Mechanics*, Volume 52, Number 7, 2012, pp. 903–916.
- [59] Sinha, T., Curtis, J. S., Hancock, B. C., and Wassgren, C. “A study on the sensitivity of Drucker–Prager Cap model parameters during the decompression phase of powder compaction simulations”. *Powder Technology*, Volume 198, Number 3, 2010, pp. 315–324.
- [60] Sirovich, L. and Kirby, M. “Low-dimensional procedure for the characterization of human faces”. *Josa a*, Volume 4, Number 3, 1987, pp. 519–524.
- [61] Sobieczky, H. and Center, D. G. A. “Knowledge based aerodynamic optimization”. In: *Proceedings of 4th SST CFD Workshop, Tokyo*. 2006, pp. 1–6.
- [62] Tang, D., Kholodar, D., Juang, J.-N., and Dowell, E. H. “System identification and proper orthogonal decomposition method applied to unsteady aerodynamics”. *AIAA journal*, Volume 39, Number 8, 2001, pp. 1569–1576.
- [63] Tarantola, A. *Inverse problem theory and methods for model parameter estimation*. SIAM, 2005.
- [64] Trujillo, D. M. and Busby, H. R. *Practical inverse analysis in engineering*. Volume 7. CRC press, 1997.

- [65] Wang, B.-T. and Chiu, C.-H. “Determination of unknown impact force acting on a simply supported beam”. *Mechanical systems and signal processing*, Volume 17, Number 3, 2003, pp. 683–704.
- [66] Xie, T., He, Y.-L., Tong, Z.-X., Yan, W.-X., and Xie, X.-Q. “An inverse analysis to estimate the endothermic reaction parameters and physical properties of aerogel insulating material”. *Applied Thermal Engineering*, Volume 87, 2015, pp. 214–224.
- [67] Xu, L., Srinivasakannan, C., Zhang, L., Yan, M., Peng, J., Xia, H., and Guo, S. “Fabrication of tungsten–copper alloys by microwave hot pressing sintering”. *Journal of Alloys and Compounds*, Volume 658, 2016, pp. 23–28.
- [68] Yan, Z., Hara, S., and Shikazono, N. “Effect of powder morphology on the microstructural characteristics of $\text{La}_{0.6}\text{Sr}_{0.4}\text{Co}_{0.2}\text{Fe}_{0.8}\text{O}_3$ cathode: A Kinetic Monte Carlo investigation”. *International Journal of Hydrogen Energy*, Volume 42, Number 17, 2017, pp. 12601–12614.
- [69] Yu, G., Wen, P., Wang, H., and Rose, J. W. “An inverse method to determine boundary temperature and heat flux for a 2D steady state heat conduction problem”. In: *Proceedings of the ASME International Design Engineering Technical Conferences and Computers and Information in Engineering Conference (IDETC/CIE 2008)*, New York. Paper number DETC2008-49811. 2008, pp. 1087–1093.
- [70] Zhou, M., Huang, S., Hu, J., Lei, Y., Xiao, Y., Li, B., Yan, S., and Zou, F. “A density-dependent modified Drucker-Prager Cap model for die compaction of Ag-Cu-Sn-In mixed metal powders”. *Powder Technology*, Volume 305, 2017, pp. 183–196.
- [71] Zienert, T., Dudczig, S., Fabrichnaya, O., and Aneziris, C. G. “Interface reactions between liquid iron and alumina–carbon refractory filter materials”. *Ceramics International*, Volume 41, Number 2, 2015, pp. 2089–2098.

This page is intentionally left blank.

APPENDIX A

EVALUATION OF THE RADIAL STRESS FROM STRAIN GAUGE

To measure the radial stress at different locations during the compaction test, strain gages are attached on the outer surface of the die-wall (mold). However, given that the gages are on the external surface of die-wall, the lateral stress (radial stress) cannot be measured directly, making it obsolete to calibrate the strain gage.

For the calibration of the strain gage, sample made from rubber (with the same diameter as the mold) is compacted in a well lubricated mold (to minimize the frictional effects). It is assumed that for such materials, the Poisson's ratio is almost equal to 0.5. From elementary elasticity theory it can be seen that for uniaxial strain compaction, the relationship between axial and radial stress is given by:

$$\sigma_z = \frac{(1 - \nu)}{\nu} \sigma_r \quad (\text{A.1})$$

where, σ_z and σ_r are axial and radial stress respectively. Therefore, for rubber (with Poisson's ratio assumed to be 0.5), axial stress applied during compaction is equal to the radial stress that the material exerts on the die-wall, as visualized from figure [A.1](#).

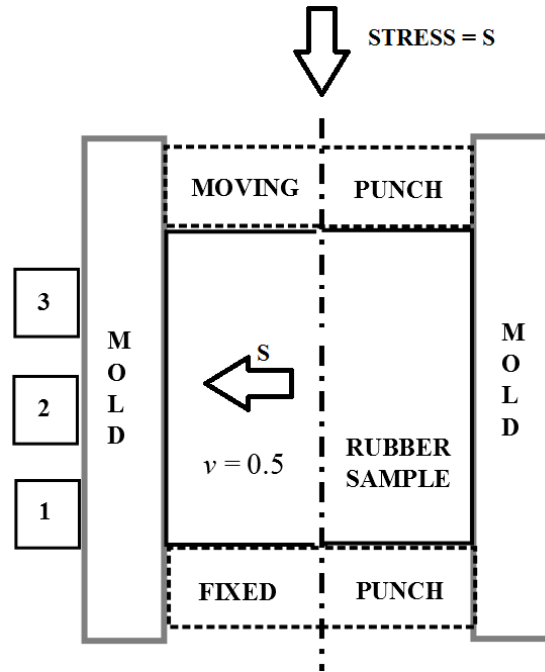


Figure A.1. Schematic representation of strain gages pasted on the die-wall

From the available value of axial stress and Poisson's ratio, a relationship can be established such that, for each value of circumferential strain, the corresponding radial stress is known. The relationship between the circumferential strain and radial stress is obviously linear, since the mold material made from steel deforms within elastic limits. Therefore, the calibration factor of the strain gage is calculated as the slope of this plot. For instance, in the present thesis, the following graph is obtained for strain gage calibration and the slope (i.e. calibration factor) is found to be 466.6 MPa.

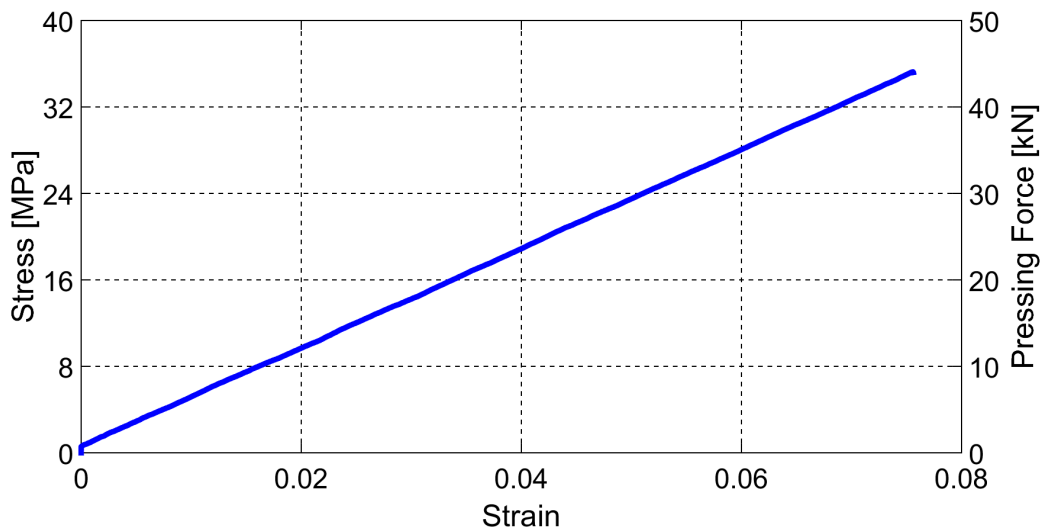


Figure A.2. Axial stress (= radial stress) vs. circumferential strain for rubber sample

Once the calibration factor is assessed, the measured circumferential strain from the powder compaction can directly be converted to the radial stress. Obviously, the load used during the calibration is kept higher than what will be eventually applied on the powder under consideration. Such a scheme allows to calculate radial stress for any pressing force up to that limit, since the value of radial stress is known for all possible readings obtained from the strain gage.

In the current work, the initial height up to which the powder is filled in the mold is very similar for all the experiments in which the radial stress is recorded. However, when specimen with relatively different initial heights are subjected to compaction, rubber samples of different heights should be considered and the calibration factor can then be calculated as the function of initial height.

This page is intentionally left blank.

BIOGRAPHY OF THE AUTHOR

A. Personal Information

Name: Shwetank Pandey

Date of birth and Place: 4th July 1991, Nagpur (India)

B. EDUCATION

B1. Undergraduate Studies

2008-2012: Bachelor of Technology (B.Tech) in Metallurgical and Materials Engineering from Visvesvaraya National Institute of Technology, Nagpur.

Thesis Title: Effect of Rolling on Corrosion Behavior of 7075 Al-alloy.

B2. Postgraduate Studies

2012-2014: Master of Technology (M.Tech) from Indian Institute of Technology, Madras with thesis development in RWTH Aachen, Germany on DAAD scholarship.

Thesis Title: Expert Model for BOF Process.

C. Scholarships

2013-2014: DAAD scholarship for master's studies in RWTH, Aachen, Germany.

2014-2017: Marie Curie scholarship for doctoral studies in University of Belgrade, Serbia

This page is intentionally left blank.

Прилог 1.

Изјава о ауторству

Потписани-а: Shwetank Pandey

број индекса: Д20-2014

Изјављујем

да је докторска дисертација под насловом

**МЕТОДА ЗА КАЛИБРИСАЊЕ КОНСТИТУТИВНИХ МОДЕЛА ЗА СИМУЛИРАЊЕ
ПРОЦЕСА ПРЕСОВАЊА КЕРАМИЧКОГ ПРАХА КОРИШЋЕЊЕМ ИНВЕРЗНИХ
АНАЛИЗА**

**PROCEDURE FOR CALIBRATION OF MATERIAL CONSTITUTIVE MODELS FOR
POWDER COMPACTION THROUGH INVERSE ANALYSIS**

- резултат сопственог истраживачког рада,
- да предложена дисертација у целини ни у деловима није била предложена за добијање било које дипломе према студијским програмима других високошколских установа,
- да су резултати коректно наведени и
- да нисам кршио/ла ауторска права и користио интелектуалну својину других лица.

Потпис докторанда

У Београду, _____

This page is intentionally left blank.

Прилог 2.

Изјава о истоветности штампане и електронске верзије докторског рада

Име и презиме аутора: Shwetank Pandey

Број индекса: Д20-2014

Студијски програм Докторска Дисертација

Наслов рада:

**МЕТОДА ЗА КАЛИБРИСАЊЕ КОНСТИТУТИВНИХ МОДЕЛА ЗА СИМУЛИРАЊЕ
ПРОЦЕСА ПРЕСОВАЊА КЕРАМИЧКОГ ПРАХА КОРИШЋЕЊЕМ ИНВЕРЗНИХ
АНАЛИЗА**

**PROCEDURE FOR CALIBRATION OF MATERIAL CONSTITUTIVE MODELS FOR
POWDER COMPACTION THROUGH INVERSE ANALYSIS**

Ментор: Проф. др. Владимир Буљак

Потписани/а: Shwetank Pandey

Изјављујем да је штампана верзија мог докторског рада истоветна електронској верзији коју сам предао/ла за објављивање на порталу **Дигиталног репозиторијума Универзитета у Београду**.

Дозвољавам да се објаве моји лични подаци везани за добијање академског звања доктора наука, као што су име и презиме, година и место рођења и датум одбране рада.

Ови лични подаци могу се објавити на мрежним страницама дигиталне библиотеке, у електронском каталогу и у публикацијама Универзитета у Београду.

Потпис докторанда

У Београду, _____

This page is intentionally left blank.

Прилог 3.

Изјава о коришћењу

Овлашћујем Универзитетску библиотеку „Светозар Марковић“ да у Дигитални репозиторијум Универзитета у Београду унесе моју докторску дисертацију под насловом:

МЕТОДА ЗА КАЛИБРИСАЊЕ КОНСТИТУТИВНИХ МОДЕЛА ЗА СИМУЛИРАЊЕ ПРОЦЕСА ПРЕСОВАЊА КЕРАМИЧКОГ ПРАХА КОРИШЋЕЊЕМ ИНВЕРЗНИХ АНАЛИЗА

PROCEDURE FOR CALIBRATION OF MATERIAL CONSTITUTIVE MODELS FOR POWDER COMPACTION THROUGH INVERSE ANALYSIS

која је моје ауторско дело.

Дисертацију са свим прилозима предао/ла сам у електронском формату погодном за трајно архивирање.

Моју докторску дисертацију похрањену у Дигитални репозиторијум Универзитета у Београду могу да користе сви који поштују одредбе садржане у одабраном типу лиценце Креативне заједнице (Creative Commons) за коју сам се одлучио/ла.

1. Ауторство
2. Ауторство - некомерцијално
3. Ауторство – некомерцијално – без прераде
4. Ауторство – некомерцијално – делити под истим условима
5. Ауторство – без прераде
6. Ауторство – делити под истим условима

(Молимо да заокружите само једну од шест понуђених лиценци, кратак опис лиценци дат је на полеђини листа).

Потпис докторанда

У Београду, _____

1. Ауторство - Дозвољавање умножавање, дистрибуцију и јавно саопштавање дела, и прераде, ако се наведе име аутора на начин одређен од стране аутора или даваоца лиценце, чак и у комерцијалне сврхе. Ово је најслободнија од свих лиценци.

2. Ауторство – некомерцијално. Дозвољавање умножавање, дистрибуцију и јавно саопштавање дела, и прераде, ако се наведе име аутора на начин одређен од стране аутора или даваоца лиценце. Ова лиценца не дозвољава комерцијалну употребу дела.

3. Ауторство - некомерцијално – без прераде. Дозвољавање умножавање, дистрибуцију и јавно саопштавање дела, без промена, преобликовања или употребе дела у свом делу, ако се наведе име аутора на начин одређен од стране аутора или даваоца лиценце. Ова лиценца не дозвољава комерцијалну употребу дела. У односу на све остале лиценце, овом лиценцом се ограничава највећи обим права коришћења дела.

4. Ауторство - некомерцијално – делити под истим условима. Дозвољавање умножавање, дистрибуцију и јавно саопштавање дела, и прераде, ако се наведе име аутора на начин одређен од стране аутора или даваоца лиценце и ако се прерада дистрибуира под истом или сличном лиценцом. Ова лиценца не дозвољава комерцијалну употребу дела и прерада.

5. Ауторство – без прераде. Дозвољавање умножавање, дистрибуцију и јавно саопштавање дела, без промена, преобликовања или употребе дела у свом делу, ако се наведе име аутора на начин одређен од стране аутора или даваоца лиценце. Ова лиценца дозвољава комерцијалну употребу дела.

6. Ауторство - делити под истим условима. Дозвољавање умножавање, дистрибуцију и јавно саопштавање дела, и прераде, ако се наведе име аутора на начин одређен од стране аутора или даваоца лиценце и ако се прерада дистрибуира под истом или сличном лиценцом. Ова лиценца дозвољава комерцијалну употребу дела и прерада. Слична је софтверским лиценцама, односно лиценцама отвореног кода.

This page is intentionally left blank.